Università degli Studi di Napoli *Federico II*

DOTTORATO DI RICERCA IN FISICA

Ciclo *XXXIV*

Coordinatore: prof. Salvatore Capozziello

Muon radiography applications: the study of the Mt. Vesuvius Great Cone and the search and 3D modeling of underground cavities

Settore Scientifico Disciplinare FIS/04

Dottorando
Mariaelena D'Errico

Coordinatore
Prof. Giulio Saracino

Anni 2018/2021

Nothing in life is to be feared, it is only to be understood.
Now is the time to understand more, so that we may fear less.

– Marie Curie

Contents

List of Figures

List of Tables

Introduction

Cosmic-rays are high energy particles produced by different astronomic events within and outside our galaxy. These particles, traveling in every direction, constantly reach the Earth's atmosphere and collide with air nucleus, generating particle showers, including muons. Muons are elementary particles, like electrons but 200 times heavier. Their ability to penetrate dense material makes them suitable to be used to look inside structures of large dimensions, the same way as X-ray are used in X-ray radiography.
This work of thesis is focused on the relative recent technique which exploits cosmic-ray muons to investigate the internal mass distribution of large objects, and that is known as *muon radiography* or *muography*. A brief summary of the contents of the various chapters is provided in the following.

Chapter 1 describes cosmic-rays and their interactions within the atmosphere focusing on how muons are produced. Then, muon radiography is presented in deep details and the most used muon detectors are overviewed. Particular attention is payed to the aspects and instruments involved in the specific applications presented in this work.

Chapter 2 is dedicated to the state of art of muon radiography worldwide: the main results of different applications, divided by area of interest, are briefly introduced and the corresponding references are provided to the reader who wants to learn more on specific topics.

Chapters 3, 4 and 5 introduce the research topics of this work, consisting of three different applications of muon radiography.

In **Chapter 3** the MURAVES (MUon RAdiography of Mt. VESuvius) experiment is presented. The project, involving the *Istituto Nazionale di Geofisica e Vulcanologia* (INGV), the *Istituto Nazionale di Fisica Nucleare* (INFN) and the Universities of Naples "Federico II" and Florence, aims to the imaging of the summital part of the Mt. Vesuvius, a very dangerous active volcano located in the south of Italy. Purposes and infrastructures are described. The monitoring and data acquisition of the muon telescope are presented. Preliminary feasibility studies are also introduced to acknowledge the reader of the difficulties of the experiment goal. Then, the main aspects of the data analysis, starting from the raw data manipulation, up to the muon tracking and good tracks selection strategies, are deeply described. To conclude, first analyzed data are presented and preliminary considerations about the resulting density asymmetry between two opposite sides of the crater are discussed.

Chapter 4 focuses on the application of muon radiography to the discover and modeling of hidden cavities or density anomalies, of particular interest in the fields of civil engineering and urban safety, archaeology and geophysical prospections in general. This application has been conducted in the underground of the Mt. Echia, a little hill in the center of Naples, where a complex of ancient cavities is excavated. This site allowed to prove the suitability of the technique to reveal the presence of cavities in the rock overlying the detector. Furthermore, an algorithm to perform a three-dimensional muon radiography has been developed and it has been applied to a discovered hidden cavity. All the details of the algorithms and the final results are described in Chapter 4.

Chapter 5 introduces the recently developed *cylindrical borehole detector*, a compact muon telescope realized to be portable and easily insertable in existing, or drilled on purpose, holes. The shape of this telescope and its sensitive elements are particularly advantageous for muon radiography application, maximizing the effective surface and minimizing the size. The detector itself is preliminarily described in Chapter 1. Data analysis, tests and preliminary applications are presented in Chapter 5. In particular, the agreement between free-sky data and simulations is shown, and the results from a first data acquisition in a real field are presented.

Principles and technologies 1

Muon Radiography is an imaging method exploiting cosmic radiation to measure the density distribution or density anomalies inside bodies of large dimensions, enriching the results from standard techniques or substituting them if not applicable. A brief introduction to the phenomenology and methodology of muon radiography is given in the following sections.

1.1 Cosmic rays

Muography is based on the existence of a natural constant flux of cosmic particles coming from the outer space, that has been largely studied and measured in the past century and is still subject of further investigations. This radiation was first observed in the 1912, when Victor Hess ascended to 5300 meters, on board of a balon, and measured the rate of ionization in the atmosphere founding that it increased to some three times that at sea level. He referred this excess to a penetrating radiation that was entering the atmosphere from above; this was what nowadays we call *cosmic rays*.

These high-energy particles arriving from outer space are mainly (89%) protons - nuclei of hydrogen, the lightest and most common element in the universe - but they also include nuclei of helium (10%) and heavier nuclei (1%), all the way up to uranium. Such particles are generally called *primary cosmic rays*. A small flux of energetic electrons and positrons, at the level of about one percent of the hadronic flux, has also been identified. Part of this flux is probably due to the pion - muon - electron (or positron) decay chain resulting from energetic collisions of the primary hadronic component with the interstellar medium and to interactions with the background radiation field [1].

The energy spectrum of these primary particles has been measured in a range from around a GeV to above 10^{12} eV; Figure 1.1 represents an overview of the measurements performed over more than 25 years [2]. The global spectrum can be divided into four regions, each describable by inverse power laws, $\propto E^{\alpha}$, with different values of α. From 10 to 10^6 GeV the spectral index is

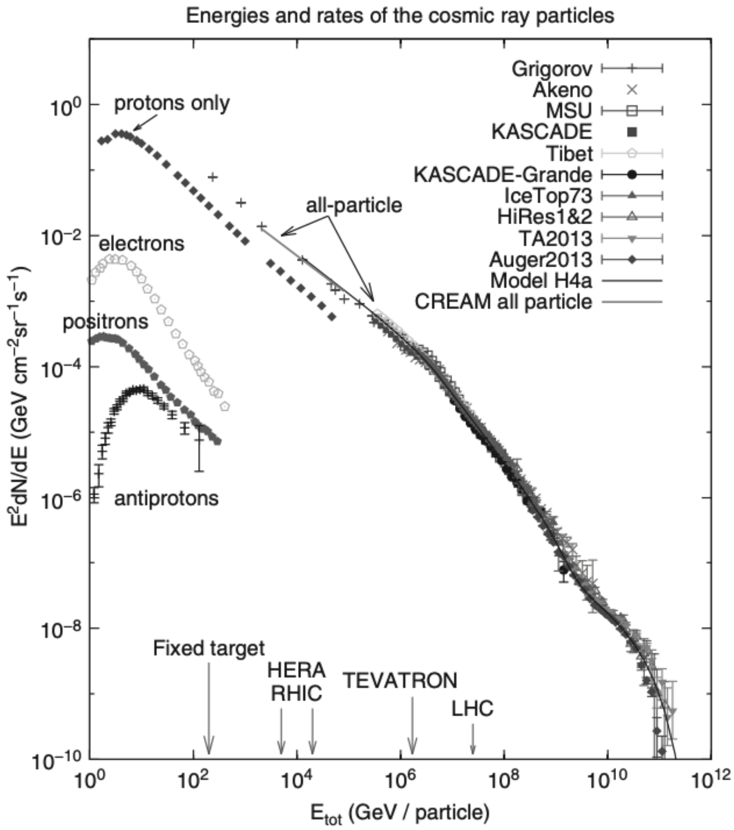

Figure 1.1: Overview of energy spectra of cosmic rays of all types. [2]

$\alpha \approx -2.7$. From 10^6 GeV to 10^9 GeV it is $\alpha \approx -3.1$. Above 10^{10} GeV the spectrum returns to $\alpha \sim -2.6$ and then it apparently cuts off around 10^{12} GeV. The transition points between the first and second and the second and third regions are known as the *knee* and the *ankle* respectively.

The four regions are well described by the mentioned power laws, but there are important hints of a finer structure within them; for more details see [2].

When primary cosmic radiations traverse the Earth's atmosphere, they interact with electrons and nuclei of atoms and molecules that constitute the air. All particles are subject to hadronic and/or electromagnetic processes, generating an *extensive particles shower*, consisting in an hadronic core and a photon-electron component which grows mostly in the electromagnetic cascades initiated by neutral pions decaying in two photons.

Energetic primary protons are characterized by an interaction mean free path λ_i of about 80 g/cm^2, corresponding to an average of 12 interaction along a vertical trajectory through the atmosphere. The most abundant particles produced by these interactions are pions, but kaons, hyperons, charmed particles and nucleon-antinucleon pairs are also generated [1]. Secondary mesons (π, K..) are unstable and are subject to decay, but if sufficiently energetic they can themselves contribute to new hadronic cascades; the relative probabilities for the interaction and decay of secondary particles are a function of energy, altitude and zenith angle. The decay probability of a secondary particle of momentum p and vertical trajectory, after traversing a thickness of X g/cm^2 can be evaluated [1], resulting in

$$W = 1 - exp\Big(-\int \frac{m_0}{\rho \tau_0 p} dX\Big) \sim \frac{m_0 X}{\rho \tau_0 p} \tag{1.1}$$

where m_0 is the rest mass of the unstable particle [Gev/c^2], X the thickness traversed [g/cm^2], τ_0 the mean life at rest [s] and ρ the density [g/cm^3]. Formula (1.1) modifies if the incident particle has a zenith angle $\theta > 0°$, enhancing by a factor sec(θ),

$$W \sim \frac{m_0 X \sec(\theta)}{\rho \tau_0 p} \tag{1.2}$$

From (1.2) it is evident that, for a given column of air traversed, the decay probability of a particle depends on its mean life, its momentum (or energy), the density (or altitude) and zenith angle of propagation in the atmosphere.
The particle flux in atmosphere, due to the cascade formation before and the energy loss and decay of secondaries then, increases with increasing depth up to a maximum at 100 g/cm^2 when it starts to decrease. The mentioned maximum was first discovered by Pfotzer at a height of about 20 km and is called *Pfotzer maximum* [3] [4].
Cosmic radiation has originally been divided into two components, the *hard* or *penetrating* component and the *soft* component. A particle is classified as soft if it is absorbed within 15 cm of lead, which corresponds to a thickness of 167 g/cm^2. The soft component contains mainly electrons and low energy muons, whereas the hard penetrating component consists of energetic hadrons and muons. Which one is dominating depends on the altitude. At sea level the hard component consists mostly of muons.

1.1.1 Cosmic-ray muons

Cosmic particles reaching the Earth ground are mainly muons, generated from the decay of charged $\pi^\pm$ and K mesons following the processes:

$$\pi^\pm \longrightarrow \mu^\pm + \nu_\mu(\bar{\nu}_\mu) \tag{1.3}$$

$$K^{\pm} \longrightarrow \mu^{\pm} + \nu_{\mu}(\bar{\nu}_{\mu}) \quad (1.4)$$

with branching ratios respectively of the 100% and 63.5%.

The probability for a muon with an energy E_{μ} to be produced by the above processes at a slant depth X in the atmosphere depends on the decay probabilities of π and K mesons, while the total muon flux reaching a certain depth is also influenced by muon energy loss and decay in flight; these effects can be accounted adding a suppression factor S_{μ}, to the muon flux, as follows:

$$\frac{dN_{\mu}}{dE_{\mu}} = S_{\mu}(E_{\mu}) \times \frac{dN_{0\mu}}{dE_{\mu}}. \quad (1.5)$$

At high energy where $S_{\mu} \longrightarrow 1$, assuming a primary proton flux of the form $P_0 E_p^{\gamma}$, with $P_0 \approx 1.8$ cm^{-2} sr^{-1} s^{-1} GeV$^{\gamma-1}$ and $\gamma \approx 2.7$, the muon flux at sea level, according to [2], can be assessed by:

$$\frac{dN_{\mu}}{dE_{\mu} d\Omega dt dS} = 0.14 \left(\frac{E}{GeV sr cm^2 s} \right)^{-2.7} \left[\frac{1}{1 + \frac{1.1 E \cos\theta}{115 GeV}} + \frac{0.054}{1 + \frac{1.1 E \cos\theta}{850 GeV}} \right] \quad (1.6)$$

In Figure 1.2, this high-energy expression is compared with the measured vertical muon flux and the full model obtainable accounting for the instability of muons. It is clear that the effects of muon energy loss and decay are important below ≈ 200 GeV for vertical muons.

To give an idea of the order of magnitude of the sea-level muon flux in simple words, it is estimated that, on the average, about 600 muons cross a human body every minute, or that 1 muon per second intercepts the palm of a hand.

The muon flux can be influenced by many variables such as altitude, solar activity, Earth and solar magnetic field and other factors. It is maximum at the Zenith (vertical direction) and it scales approximately with $\cos^2(\theta)$, with θ the angle with respect to the vertical, and the average energy is comprised between 3 and 4 GeV.

In a muon radiography experiment the flux of incident cosmic muons is used to determine the attenuation produced by the target; it is thus of critical importance to be provided of a model of this flux as accurate as possible in order to minimize biases in the density measurements. Different solutions are possible: a Monte Carlo simulation can be performed starting from pri-

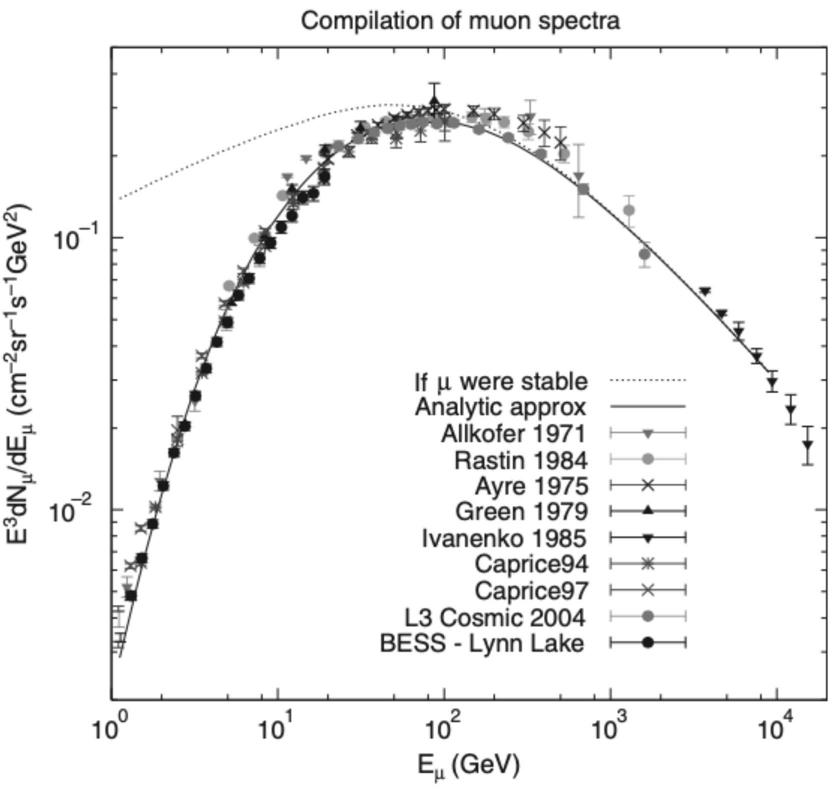

Figure 1.2: Comparison between measured muon flux and that calculated with and without the decay and energy loss contribution [2]

mary particles and following their interactions up to the muon production; other possibilities are to use the measured fluxes as reference, or to provide an analytical model for sea-level muon flux, as in the case of the Gaisser's model in eq. (1.6). This formula is not enough accurate to properly describe the muon flux if the Zenith angle θ is above 70°. However, in several scenarios where muon radiography is applied, useful muon directions are near-horizontal, thus it is necessary to have a model accurate for those angles. A new parametrization has been introduced to account for the Earth curvature, non-negligible at high θ, substituting θ with a new angle $\theta^\star$ defined by:

$$\cos\theta^\star = \sqrt{\frac{(\cos\theta)^2 + P_1^2 + P_2(\cos\theta)^{P_3} + P_4(\cos\theta)^{P_5}}{1 + P_1^2 + P_2 + P_4}} \tag{1.7}$$

where the parameters are given in Table 1.1. This new parametrizations is included in the modified Gaisser's formula [5]:

$$\Phi_\mu(\theta, E) = 0.14\left[\frac{E}{GeV}\left(1+\frac{3.64GeV}{E(\cos\theta^\star)^{1.29}}\right)\right]^{-2.7}\times \\ \times\left[\frac{1}{1+\frac{1.1E\cos\theta^\star}{115GeV}} + \frac{0.054}{1+\frac{1.1E\cos\theta^\star}{850GeV}}\right] \tag{1.8}$$

P_1	P_2	P_3	P_4	P_5
0.102573	-0.06828	0.958633	0.0407253	0.817285

Table 1.1: Parameter used in Eq. 1.8

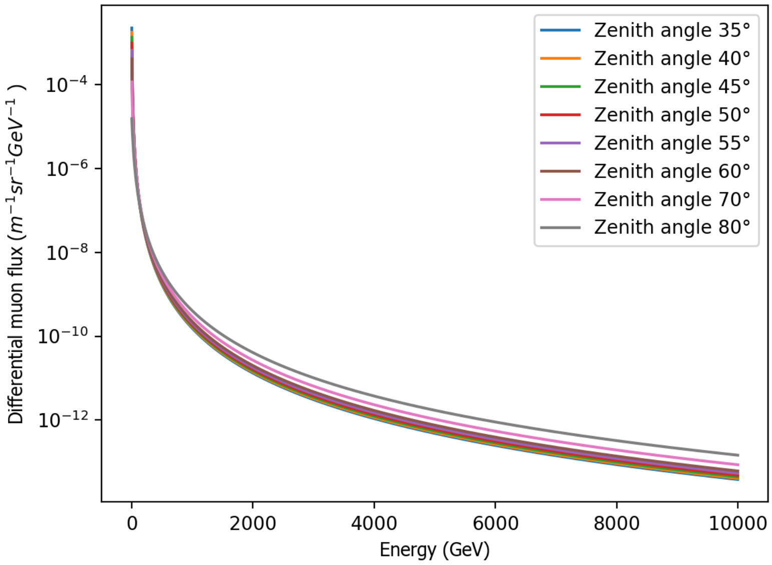

Figure 1.3: Expected muon fluxes at different Zenith angle, given by Gaisser's modified formula (eq. (1.8)).

which also account for low-energy regimes. Figure 1.3 represents eq. (1.8) for different values of the Zenith angle.

1.1.2 Interactions with matter

Muons loose part of their energy when they pass through matter, but differently respect to other particles, they can cross hundred meters of rock without being completely absorbed. This property makes muons suitable to investigate the interior of big bodies, such as volcanoes, pyramids, and so on.
The most relevant effects following the passage of muons through matter are: I) an energy loss and II) a deviation of the particle trajectory (*multiple scattering*). Both of these effects can give informations about the composition of the crossed material.
The mean stopping power for a muon in a material can be described by the following [6]:

$$-\frac{dE}{dX} = a(E) + b(E)E \tag{1.9}$$

where $a(E)$ accounts for ionization and atomic excitation and $b(E)$ accounts for radiative processes, *i.e.* bremsstrahlung, pair production and photonuclear interactions. The first term, dominating at low energies, ~ below 100 GeV, is well described by the

Bethe - Bloch formula:

$$\left\langle -\frac{dE}{dX} \right\rangle = Kz^2 \frac{Z}{A} \frac{1}{\beta^2} \left[\frac{1}{2} \ln \frac{2m_e c^2 \beta^2 \gamma^2 W_{\max}}{I^2} - \beta^2 - \frac{\delta(\beta\gamma)}{2} \right] \tag{1.10}$$

which describes the energy loss for ionization and atomic excitation per unit *opacity* $X = \int_0^x x' \rho(x') dx'$. The stopping power in eq. (1.10) is expressed in MeV g cm^{-2}, K is a proportionality coefficient, z the charge number of the incident particle (z = 1 for muons), Z and A the atomic number and mass of the absorber, I the mean excitation energy, m_e the mass of the electron, W_{max} the maximum energy transfer in a single collision and $\delta(\beta\gamma)$ a correction related to the density effect.

The radiative processes contributing to the muon energy loss, are formalized in the term $b(E)E$ where $b(E)$ is a slowly varying function of energy which is asymptotically constant and can be expansed as the sum of three terms, $b = b_{brems} + b_{pair} + b_{nucl}$, from bremsstrahlung, pair production and photonuclear interactions. The reflection of these processes on the muon stopping power law are widely discussed and formally derived in [6] and will not be treated in this thesis.

Practically, several muon radiography experiments by absorption use to take as reference, to perform simulations and evaluate the muon flux expectations, a common material type, referred as *standard rock*, for which the rate of muon energy loss has been tabulated. This fictitious material consists of a density of crystalline quartz (i.e. ρ_{qrz} = 2.65 g cm^{-3}), a Z and A of 11 and 22, respectively (which is almost sodium), and density effect parameters that have been measured on calcium carbonate. As widely explained and studied in [7] by Lechmann et al., the variations in chemical composition of the rock can generate serious biases on the muon flux. Aside from the variations in density that can be easily accounted, the composition of the rock can also influence the muon flux. This study reveals that the muon fluxes for every rock below 300 m do not depart more than 2.5 % from their respective density-modified standard rock flux. However, when the target consists of high Z^2/A rocks (like basalts and limestones) and the rock thicknesses become larger than 300 m, the flux discrepancies start to exceed ±2.5%. This corresponds to the point where radiative losses, which stopping power contribution depend on Z^2/A start to become the dominant energy loss processes. This investigation thus suggests to account for the chemical composition of rock when high Z^2/A ratios, as basaltic rocks or carbonates, are faced and thicknesses above 300 m are involved. Currently these effects are not yet assessed within the

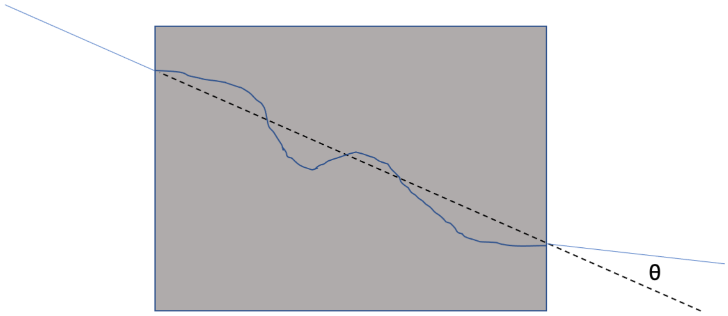

Figure 1.4: A schematic view of multiple coulomb scattering process.

MURAVES experiment, which is studying the mass distribution of the Mt. Vesuvius (see Chapter 3).

As already mentioned, when muons cross a given material they are also subjected to *multiple coulomb scattering*, repeated random deviations from their direction, resulting in a net exiting angle θ. A scheme of this effect is represented in Fig 1.4.
If the average number of scatterings is greater than 20 and the energy loss is small, that is usually the case of muographic applications, the distribution of the net deflection as a function of the thickness can be obtained treating the process statistically, such as in the theory of Molière. For many applications the net scattering distribution can be described considering the central limit theorem, which states that the sum of a large number of distributions, in this case the single Coulomb scatterings, can be approximated by a Gaussian. The root mean square (rms) of the obtained Gaussian distribution of the projected angle can be expressed as follows:

$$\sigma_\theta \quad = \quad \frac{13.6\text{MeV}}{\beta c p} z \sqrt{\frac{x}{X_0}} \left[1 + 0.038 \ln \left(\frac{x z^2}{X_0 \beta^2} \right) \right] \tag{1.11}$$

where p, βc, and z are the particle momentum, velocity, and charge (for the muons $z = 1$), x is the thickness of the scattering medium, $\sigma_\theta = \theta^{\text{rms}}_{\text{plane}} = 1/\sqrt{2}\ \theta^{\text{rms}}_{\text{space}}$ and X_0, the material radiation length, is defined as:

$$X_0 = 716.4\ g/cm^2 \frac{A}{Z(Z+1)\ln(287/\sqrt{Z})} \tag{1.12}$$

where Z is the the atomic number and A the atomic mass number. Some muon radiography applications are based on the measurement of the muon deflections to assess properties of the deflettant material; more details are given in the next section.

1.1.3 Imaging with muons

Cosmic muons come with straight trajectories, not significantly affected by Earth's magnetic field, and have a high penetrating power, allowing them to cross very deep rock masses. These particles are indeed exploited in different applications that can be distinguished in: muon radiography by absorption, usually referred simply as **muon radiography**, muon radiography by multiple scattering, or **muon tomography**, both devoted to the imaging of large objects, and **muon metrology**, an alternative method to control civil structures stability. A brief overview of these applications is provided in the following.

Muon radiography

Muon radiography by absorption measures the absorption degree of muons through a given volume to indirectly get the mean density of the traversed materials or to reveal the presence of possible density anomalies, such as void regions or high density deposits, manifesting themselves as an excess or deficit of muons respectively.
The principle is very similar to the common X-ray radiography, used to scan human body or little objects, with the difference that in muography the source is natural (cosmic muons), thus its flux is fixed, and is not unidirectional. Another crucial difference stays in the nature of muons: these particles can penetrate hundreds meters of rock, while X-rays cannot survive deeper than about ten meters. This property makes muons suitable to scan bigger bodies respect to X-rays.
A typical muography experiment measures the incoming muon flux as a function of the direction (θ, ϕ), where θ is the Zenith and ϕ the horizontal angle. Given the differential muon flux $\phi_\mu(\Omega; E)$, the number of muons detected by the muon telescope $N_\mu(\theta, \phi)$ can be described as:

$$N_\mu(\theta, \phi) = \Delta t_{ACQ} \int_{2\pi} d\Omega \, S_{eff}(\Omega) \int_{E_{min}}^{\infty} dE \, \phi_\mu(\Omega; E) \, \epsilon \quad (1.13)$$

where Δt_{ACQ} is the total active acquisition time, Ω is the direction (θ,ϕ), $d\Omega = \sin\theta d\theta d\phi$ is the element of the solid angle, $S_{eff}(\Omega)$ is the effective surface of the telescope in the direction Ω and ϵ

is a global efficiency that in principle depends on both Ω and E. The effective surface

$$S_{eff}(\Omega) = g(\Omega)\, S \tag{1.14}$$

depends on S, the total sensitive area of the telescope, and on the geometrical factor $g(\Omega)$ which depends on the specific telescope geometry and estimates the fraction of S involved in the detection of particles coming from Ω. More details are given in section 3.6.3 for the case of a multi-planes muon tracker.
The total efficiency ϵ is defined by different effects; the trigger efficiency, which involves also the detector element efficiencies, the data-acquisition efficiency and the analysis efficiency. The term ϵ can thus be factorized as:

$$\epsilon = \epsilon_{tr}\, \epsilon_{DAQ}\, \epsilon_{an}. \tag{1.15}$$

The observed number of muons depends on the traversed opacity X, through the integration extreme in (1.13),

$$E_{min} = E_{min}^{rock}(X) + E_{min}^{det} \tag{1.16}$$

where $E_{min}^{rock}(X)$ is the minimum energy a muon needs to survive the opacity X, and E_{min}^{det} is the energy necessary to be detected. Usually to reduce systematic uncertainties, the mass distribution is evaluated from the *transmission* $T(\theta,\phi)$, instead of using the measured flux; $T(\theta,\phi)$ is defined as the ratio between the measured flux in (1.13) and a calibration flux, called *free-sky*, measured by taking data in the same conditions but pointing the detector toward the open sky for a certain time Δt_{fs}. This procedure ensures that geometrical factors and trigger efficiency are in good approximation equal for both datasets and thus cancel. What remains is:

$$T = k \cdot \frac{N_\mu(\theta,\phi)}{N_{fs}(\theta,\phi)} = k \cdot \frac{\int_{E_{min}}^{\infty} \phi_\mu(\Omega; E) dE}{\int_{E_{min}^{det}}^{\infty} \phi_\mu(\Omega; E) dE}, \tag{1.17}$$

where k is the calculable constant

$$k = \frac{\Delta t_{fs}}{\Delta t_\mu} \frac{\epsilon_{DAQ}^{\mu}}{\epsilon_{DAQ}^{fs}} \frac{\epsilon_{an}^{\mu}}{\epsilon_{an}^{fs}} \tag{1.18}$$

The quantity in (1.17) is used to assess the density distribution or density anomalies by comparing the measured values to the expectations. The specific procedures depends on the particular case. More details are given in the next chapters, where specific applications are described.

Muographic data can be also exploited to measure a three-dimensional density distribution; muographic data alone can be sufficient if enough muographies from different points are available, but also gravimetric data can be added to apply a joint inversion of both data types. The 3D inverse problem is posed by dividing the investigated region into M voxels *i.e.* basic volumetric units, which size depends strongly on the spatial resolution and on the amount of available data. The opacity derived from muon radiography from the *i-th* direction, is written as:

$$X_i = \sum_j^M L_{ij}\rho_j \tag{1.19}$$

where ρ_j is the density of the *j-th* voxel and L_{ij} is the matrix of the length crossed by the *i-th* direction in the *j-th* voxel. The inverse problem consists in evaluating the density vector ρ_j that reproduces the measured opacity vector (*i.e*. the measured flux) for each direction i of all the detectors. Usually data are not enough to state a unique solution of the problem, so further assumptions have to be considered.
Adding gravimetric data to the inverse problem declaration can help to constrain the solution. Gravimetry provides a traditional method to measure density anomalies inside large objects such as volcanoes, measuring the vertical component of the local gravity field; the vertical component of the gravity anomaly measured at the *i-th* gravity station is then expressed as

$$\Delta g_i = \Delta g(x_i, y_i, z_i) = \sum_j^M G_{ij}\rho_j \tag{1.20}$$

where G_{ij} is the vertical gravity contribution of the *j-th* voxel to the *i-th* gravity station for unit density. Equations 1.19 and 1.20 can be merged in a unique matricial equation:

$$\mathbf{d} = \mathbf{A}\rho \tag{1.21}$$

where **d** and **A** are integrated data vector and integrated design matrix:

$$\mathbf{d} = \begin{pmatrix} X \\ \Delta g \end{pmatrix}, \mathbf{A} = \begin{pmatrix} L \\ G \end{pmatrix} \tag{1.22}$$

Given the inverse problem, a lot of effort has been and is currently paid to the development of more and more advanced solving strategies. One of the possibilities, chosen by Nishiyama et al. [8] [9], applying the inversion on the Mt. Showa-Shizan data, is based on a Bayesian approach [10]. Given the observed data $\mathbf{d}_{obs}$, the solution of Eq. (1.21) is expressed as

$$\rho = \rho_0 + (\mathbf{A}^T\mathbf{C_d^{-1}A} + \mathbf{C}_{\rho_0}^{-1})^{-1}\mathbf{A^T C_d^{-1}}(\mathbf{d_{obs}} - \mathbf{A}\rho_\mathbf{0}) \qquad (1.23)$$

with covariance matrix written as

$$\mathbf{C}_\rho = (\mathbf{A^T C_d^{-1} A} + \mathbf{C}_{\rho_\mathbf{0}}^{-1}) \qquad (1.24)$$

where ρ_0 is an initial guess density, and $\mathbf{C}_{\rho_\mathbf{0}}$ and $\mathbf{C_d}$ are covariance matrices for the initial guess and the data. To deal with the ill-posed inverse problem, a smoothing constraint has been imposed on model parameters through an exponential covariance

$$C_\rho(i,j) = \sigma_\rho exp(-d(i,j)/l) \qquad (1.25)$$

where σ_ρ is the a priori error of the density, l is the correlation length, and $d(i,j)$ is the distance between the i-*th* and *j-th* voxels. Other possible approaches to the inverse problems are introduced and cited in [11].

Muon tomography

Muon tomography is a different muographic approach, which exploits the multiple Coulomb scattering process. It finds applications in transport, industrial and nuclear controls. It is based on the measurement of the deviation of muons crossing the object to inspect. The technique is suitable to investigate volumes characterized by thicknesses not exceeding tens of meters, and requires to install detectors to measure muons before and after they cross the target.
Simplifying eq. (1.11), the standard deviation of the scattering angle for a muon of momentum p can be approximated by:

$$\sigma_\theta \approx \frac{13.6MeV}{pc}\sqrt{\frac{x}{X_0}} \qquad (1.26)$$

The scattering angles can be related to the linear scattering density $\lambda = 1/X_0$ that is approximately the product of the atomic number Z and the density ρ, $\lambda \approx Z\rho$ as it can be deduced

from eq. (1.12).
Eq. (1.26) is obtained considering monochromatic muons of momentum p distributed according to a Gaussian; but cosmic muons are not monochromatic, and their scattering angle has a distributions described by the following expression:

$$\frac{dN}{d\theta} = \frac{1}{b\sqrt{2\pi x\lambda}} \int_0^\infty p f(p) e^{\frac{-\theta^2 p^2}{2x\lambda b^2}} dp \tag{1.27}$$

where $f(p)$ is the momentum spectrum and b= 13.6 MeV/c. The variance of distribution in eq. (1.27) is:

$$\langle\theta^2\rangle = \lambda x b^2 \langle\frac{1}{p^2}\rangle \tag{1.28}$$

where the individual unknown momentum is substituted by a fixed value computed from the average value of the distribution of the quantity $1/p^2$. Eq. (1.28) shows the dependance of the scattering angle variance from the material density through the presence of λ. In some cases the muon momentum measurement cannot be replaces by the mean cosmic-ray muons momentum, and informations about real muon momenta have to be provided to perform the required results.
Muon tomography can also provide a 3D imaging of the object, if the detector dimensions are larger than or at least comparable with the size of the volume to inspect. NEW: The research work presented in this thesis do not concerns applications of Muon Tomography; for this reason the reader is invited to follow as instance the reference [12] to find more detailed descriptions of the technique. Anyway, some existing applications are briefly introduced in Chapter 2.

Muon metrology

Muons, especially if high energetic, have a very straight trajectory not even influenced by the geomagnetic field. This feature has been largely exploited to align and calibrate particle detectors, especially ones adopted in high energy physics. To this purpose, the idea is to reconstruct trajectories of muons which cross different parts of the detector, and to use track parameters to estimate the position and orientation of all active detector elements.
Recently, the possibility to use a similar method exploiting cosmic muons for the metrology of structures, such as an industrial press and historical buildings, has been investigated by some authors [13] [14]. This application is based on the measurement of

possible changes over time of the relative alignment of a system of detectors, some integral to the structure of interest and the others to the surrounding environment. Changes in the alignment between the detectors reflect on the quality of the muon track, that means the chi square gets worst, and can be associated to movements or deformations of the structure. Muon metrology is interested in the relative changes of aligned parameters, which are less sensitive to several sources of systematic uncertainties compared to absolute measurements. Moreover, less stringent requirements are necessary on the number of detectors, on their resolution and on the statistics to collect respect to those for detector alignments.
A possible drawback of using cosmic-muons for metrology is the limited muons flux and the consequent long data taking periods needed to collect enough statistics for the set goal. However, for applications such as the static monitoring of historical buildings, data takings of the order of few days (or even few weeks) could not be a problem, as typical structural deformations evolve over a very long period of time.
Even if the method concerns the measurement of the changes in the relative position between two detectors by the reconstruction of muons trajectories, if some material is interposed between the two instruments, those muons can be affected by multiple scattering. In order to reduce the impact of the multiple Coulomb scattering, a minimum χ^2 estimation method, independently applied to both x-z and y-z views can be implemented to measure the relative displacement and inclination between the muon tracks extrapolated independently from the two detectors. Defining $(x'_h - x'_l)$ and $(\theta_h - \theta_l)$ the differences of the x and θ coordinates of the extrapolated points of the two tracks on a common plane, in case of perfectly aligned telescopes, these variables are zero in average; however if some changes occurred in the detector alignments, it determines non-zero expected values for these variables, allowing for the estimation of the relative displacement and inclination from a minimum χ^2 estimation method, using the following definition [14]:

$$\chi^2 = \sum_i \left[\frac{(x'_{h,i} - x'_{l,i})}{\sigma^2_{x'_{h,i}} + \sigma^2_{x'_{l,i}}} + \frac{(\theta_{h,i} - \theta_{l,i})}{\sigma^2_{\theta_{h,i}} + \sigma^2_{\theta_{l,i}}} \right] \tag{1.29}$$

where $\sigma_{x'}$ and σ_θ are the errors on the reconstructed x′ and θ respectively, while l and h indicate the lower or higher detector. Some examples of muon metrology applications are briefly introduced in Chapter 2.

1.2 Detectors

Muon radiography applications are often performed in harsh environments (volcanoes, pyramids, underground...). This requires detectors to be compact, easily transportable and installable, low or zero power consuming, and quite stable when environmental conditions vary. For the same reason the capability to control the status of the system remotely results to be particularly advantageous.
Several different types of detectors have been used to perform muography; the choice depends on the particular application and on which characteristics are preferred. In the next paragraphs an overview of the adopted technologies is presented; the detectors used in the context of this work are described in more details.

1.2.1 Overview

The most adopted muon telescopes for muon radiography are: nuclear emulsion detectors, scintillation detectors and gaseous detectors. The principal feature required to the used detector is the tracking capability, *i.e.* the capability to reconstruct the incoming particle direction in space.
Nuclear emulsion detectors have been largely chosen in muon radiography applications. They are similar to photographic emulsions; the particle is revealed because its passage produces a ionization, visible as a path of Ag grains. The principal advantages of nuclear emulsions are compactness and transportability, the high spatial resolution and the capability to work without electric power supply; anyways, emulsions lose efficiency when exposed to high temperatures, and the worst drawbacks are that no online monitoring is possible and the exposure time cannot be much long. Furthermore, because all events are registered together on the films, data can be analyzed only at the end of the data taking, when the emulsion have to be scanned, through a process that requires a relevant time and sophisticated equipments.
A large variety of applications make the use of scintillator hodoscopes. Scintillators respond to the passage of a ionizing particle emitting light by atomic excitations. The light is then collimated to a light sensor, that translate the luminous signal in electric signal. A scintillator tracker is usually composed by two or more planes containing two layers of orthogonal scintillator bars used to track particles in two independent projections . The

dimensions and the section (rectangular, triangular...) of the bars define the sensitivity and resolution of the detector. Commonly used photodetectors are Photo-Multiplier Tubes, PMT, (single or multi anodes) and more recently Silicon Photo-Multipliers (SiPM). The latter are cost effective, efficient, robust, consume low electric power and, due to their small dimensions, order of mm^2, are ideal for compact assembly. The major drawback of these devices is the higher sensitivity to temperature variations with respect to phototubes. Examples of scintillator trackers are described in the following sections.
Gaseous detectors are used in both muon radiography and muon tomography. The usage of these instruments is less practical respect to the previous examples because of the necessity of gas changing, a drawback that can be determinant when the field is particularly uncomfortable. Anyway, these detectors, such as drift chambers or resistive plate chambers, represent the best choice in multiple scattering tomography where the target objects, often of large dimensions, need to be entirely covered; indeed, gaseous detectors cab be of larger size at a reasonable cost; also, spatial and angular resolutions comparable or better than scintillators ($\sim 300\ \mu$m, ~ 1 mrad) can be reached.
In the next sections some particular muon telescopes, related to the specific applications presented in this work, are described in deep details.

1.2.2 Mu-Ray prototype

The Mu-Ray detector has been realized in 2010 to be used for muon radiography of volcanoes, especially the Mt. Vesuvius. Within the Mu-Ray project, it has been tested in two different volcanic environments, the Mt. Vesuvius and the Puy the Dome [15] [16]. Successively, it has been also exploited to the investigation of undergrounds, as widely described in Chapter 4.
The Mu-Ray hodoscope (Fig. 1.5) is composed of three tracking stations, consisting of two adjacent planar arrays of plastic scintillator bars, orthogonally oriented to provide the x and y coordinates of the muon impact point. The basic module of the hodoscope is an array of 32 plastic scintillator bars, shown in Figure 1.6. Two of these are assembled to form a single-view plane, and two planes are interfaced orthogonally to form a tracking station. The sensitive area of each station is 1 m^2. The scintillator bars have been provided by FERMILAB-NICADD and they are of the same kind used for the D0 [17] and Min-

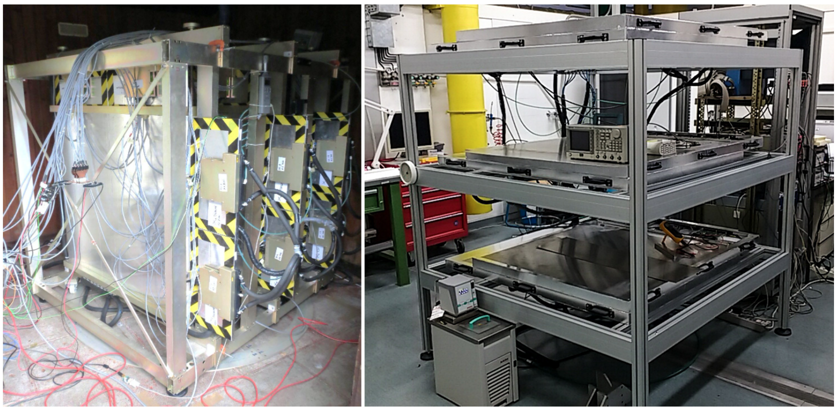

Figure 1.5: The Mu-Ray detector in two different configurations. Left: configuration with vertical planes, sensible to near-horizontal muons. It is the best chose to look through objects from the side. Right: configuration with horizontal planes. It is more sensitive to vertical muons; it is chosen when the detector has to be installed under the object to be investigated.

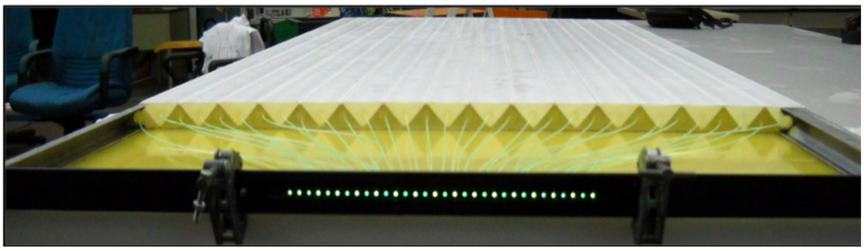

Figure 1.6: The basic module of Mu-Ray detector.

erva [18] experiments. They are produced by extrusion with a central hole of $\sim 1.5 \pm 0.1$ mm diameter to host a WLS fiber and present a TiO_2 coating (0.25 mm thick) that increases the internal reflectivity and shields them from the environmental light. The scintillator plastic is made of a bulk of polystyrene with the addiction of PPO and POPOP scintillation dopants emitting in the blue wavelength region centered on 420 nm, with $\sim$3 ns of emission time. The adopted fibers are 1.2 mm diameter multiclad Kuraray Y11 S-35 type, characterized by an absorption spectrum approximately in the wavelength range 400-470 nm and an emission spectrum in the range 470-550 nm, with a peak in the green.

Scintillator bars are characterized by an isosceles triangle-shaped section (Figure 1.7) with 3.3 cm basis and 1.7 cm height. The triangular shape allows to improve the spatial resolution, using a weighted average to evaluate the muon position, with the the charges collected by the involved adjacent bars taken as weights. The light propagating along the WLS fibers is read out by SiPMs, one coupled to each fiber. The photosensors are organized in arrays of 32 elements placed on a hybrid printed circuit (one for each detector module), shown in Figure 1.8.

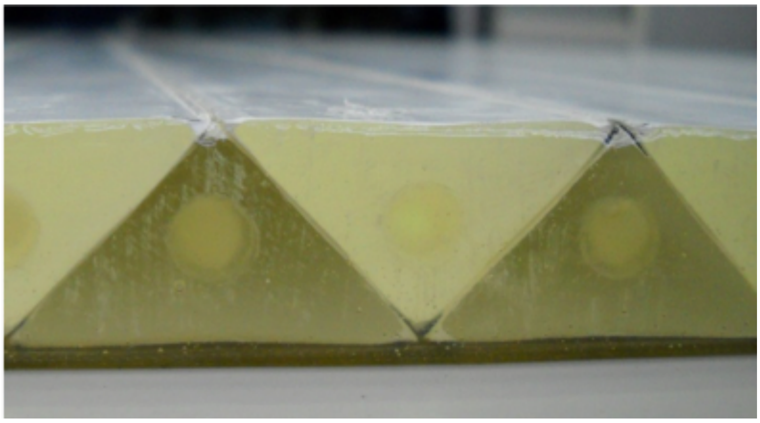

Figure 1.7: Traversal section of Mu-Ray scintillator bars.

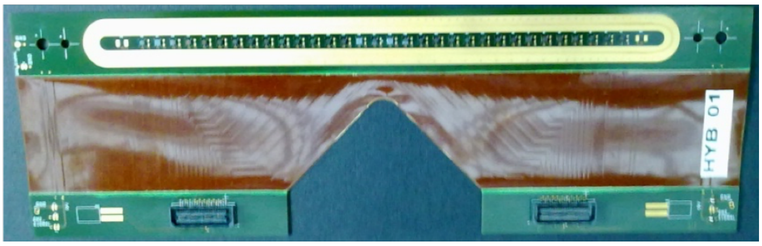

Figure 1.8: Hybrid board with 32 SiPMs housed.

Front-End electronics and DAQ system

The installation on in-hospital locations as the side of a volcano or underground, often implies the absence of a standard electricity supply. This led to the development of a low power consuming Front - End Electronics (FEE) and Data Acquisition (DAQ) system. The Front-end electronics consists in 12 equal SLAVE boards, one for each module, which contains 32 SiPM channels. Each board is equipped with an EASIROC ASIC [19] providing SiPM gain adjustment, tunable preamplification gain, signal shaping, charge measurement, high and low gain multiplexed outputs. Each SLAVE board also contains a TDC for the measurement of the time-of-flight (ToF) with 0.1 ns resolution. Each board consumes less than 2.5 W.
SiPMs signals are amplified and converted in ADC counts, measuring the charge deposited in the SiPM. Each channel also produce a fast logical signals, according to a tunable threshold level, and the logical OR of all the 32 fast signals gives the local trigger (OR32) to be sent to the MASTER board to build the global trigger.
The MASTER board, equipped with an FPGA and a Rasberry-Pi computer, is devoted to the global trigger and DAQ system. All the SLAVE outputs are collected by the MASTER, which verifies if the trigger requirement, programmed by the FPGA, is fulfilled, and, if yes, data are acquired and stored on a storage unity. In Figure 1.9 a SLAVE an a MASTER board are showed.

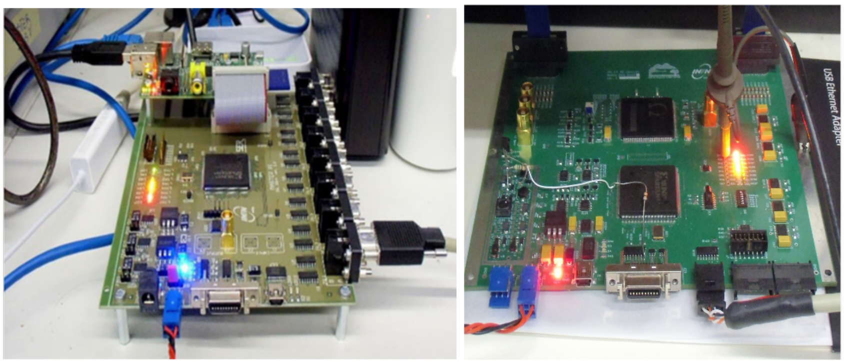

Figure 1.9: Left: the MASTER board. Right: a SLAVE board.

An important feature of the MU-RAY front-end electronics is the capability of measuring the time of flight (ToF) of the muon crossing the telescope. This ToF measurement allows to reject the background due to muons traversing the telescope from the wrong direction and scattering upwards on the Earth's surface. Each SLAVE is provided of a *time expansion* system based on the charge and a slower discharge of a capacitor. The capacitor starts charging when a local trigger occurs on the relative board. The charging process stops when a trigger signal is received from the MASTER board. Thus, the capacitor starts discharging. The discharge needs a time $T_{discharge} \sim E \cdot T_{charge}$ where E is the *expansion factor* usually of order ~ 50. The discharge time is measured by the SLAVE clock operating at 50 MHz, with an effective resolution of about 400 ps.

1.2.3 MURAVES telescope

MURAVES is a muon telescope designed to work in the volcanic area of Mt. Vesuvius. It has been realized on the basis of the past experience of the Mu-Ray prototype (section 1.2.2) and consists in an array of three identical muon hodoscopes, called ROSSO, NERO and BLU, showed in Figure 1.10.

The total sensitive area of the telescope is 3 m^2; the increased total area of the telescope, respect to the Mu-Ray prototype, is necessary to reduce the exposure time needed to acquire a consistent statistics. Each MURAVES hodoscope is analogous to the Mu-Ray detector but with an additional station. As it can be seen in Figure 1.10, the stations are installed vertically and on different levels, to maximize the geometrical acceptance in the direction of the volcano's crater. A lead block is also interposed between the last two stations to reduce the background, stopping particularly the low-energy component of cosmic-rays. The geometry and

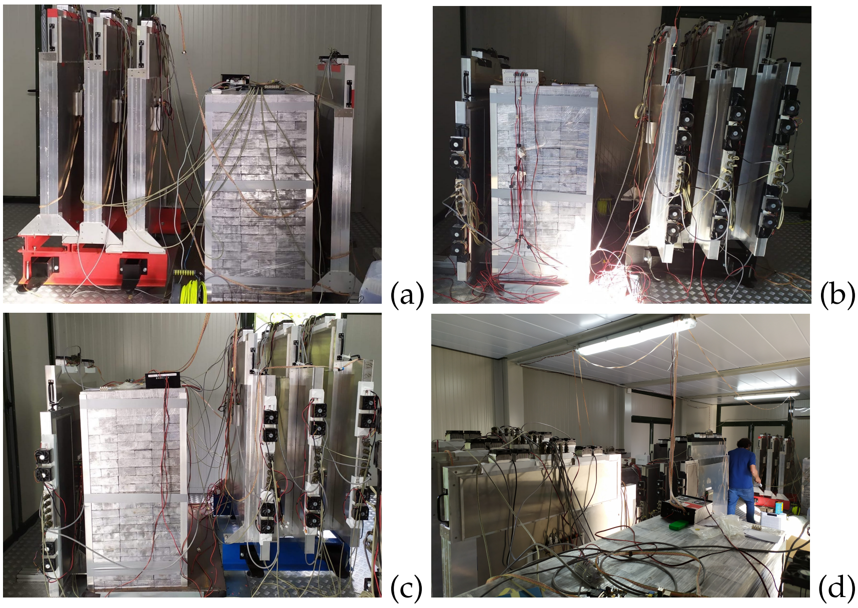

Figure 1.10: The MURAVES muon telescope: (a) ROSSO hodoscope; (b) NERO hodoscope; (c) BLU hodoscope; (d) a view of how the three hodoscopes are installed in the Vesuvius laboratory.

the reference frame of the hodoscopes is pictorially represented in Fig. 1.11. The front-end electronics is the same used in the Mu-Ray apparatus but each MURAVES hodoscopes is provided of 16 SLAVEs and 1 MASTER for a total of 51 electronic boards. The photosensors used in this case are ASD-RGB1C-P Silicon PhotoMultipliers (SiPM) [20], produced by the Advansid company. Some relevant parameters of these SiPM model are reported in Table 1.2. SIPMs are quite sensitive to temperature variations; this

Dark Counts (DCR) (kHz/mm^2)	< 100
Photon Detection Efficiency PDE (%)	32.5
Operating Voltage (V)	30
Gain	2.6×10^6
Breakdown Voltage Temperature Coeff. (mV/°C)	27

Table 1.2: Relevant parameters of the Advansid SiPM ASD-RGB1C-P.

could means a big deal for the specific application MURAVES is devoted to; in fact, to be able to operate in in-hospitable environment as the side of a volcano, the detector and all related technologies have to be stable with environmental variations (humidity, temperature...). At this scope, a temperature control system has been designed to keep the SiPM operating temperature stable and adjustable.

The temperature control system

The MURAVES temperature control system (Figure 1.12) is a thermoelectric system based on the Peltier effect, able to both cooling and heating the photosensors. It consists in two peltier

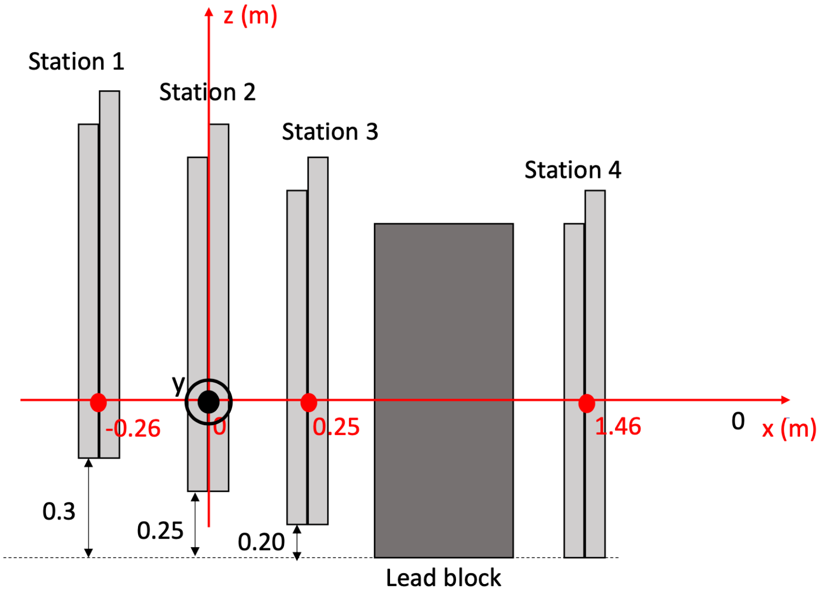

Figure 1.11: A schematic view of the reference frame of the MU-RAVES hodoscopes.

Figure 1.12: The temperaure control system. Left: the elements before installing on the detector. Right: the system installed on the detector.

cells for each array of SiPMs (haused on the same hybrid circuit), a copper bar to ensure a uniform heat distribution, and a couple of fans to the heat ventilation. A custom circuit controls the thermoelectric cells by the use of Pulse Width Modulation drivers to pilot the Thermal Electric Coolers with maximum efficiency. The board is connected to the outside world through an USB and a CAN Bus. The temperature on SiPMs is modulated to maintain a 5 degrees maximum difference respect to the environmental temperature. This strategy allows to reduce the consumption from 15-20 W to only 4 W per layer. Figure 1.13 clarify how the system works: when the difference between the current working point temperature and the environmental temperature becomes higher than 5 degrees, the SiPMs working point is changed to reduce this gap. Also, the environmental humidity is constantly measured and the temperature to impose on SiPMs is chosen safely distant from the dew point, to avoid condensation which could seriously damage the instrumentation. On the bottom of Figure 1.13 the measured temperature on SiPMs is shown; as it can be seen the system is able to apply the desired temperature

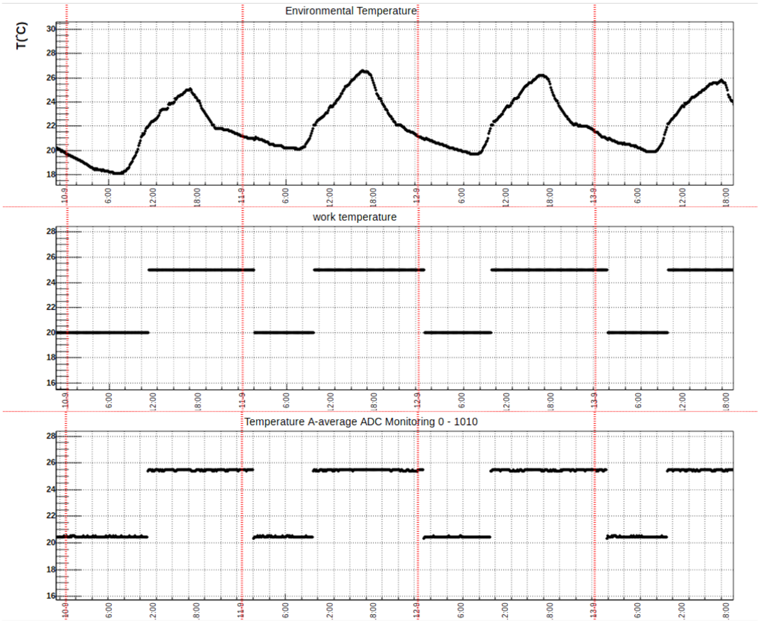

Figure 1.13: Top: measured environmental temperature. Center: nominal temperature set on SiPMs. Bottom: temperature measured on SiPMs.

very precisely.

1.2.4 Borehole cylindrical detector

Some applications of muon radiography, such as the search for hidden cavities or the study of different materials deposits in mines, require the detectors to be installed underground, inside tunnels, excavated chambers or drilled holes. Usually the available locations are difficult to be accessed by people and by big instrumentations; this issue suggested the idea to construct a very compact cylindrical muon tracker, which maximizes the acceptance respect to its small dimensions.
The borehole cylindrical detector [21] has been designed and realized at the Physics Department at the University of Naples Federico II, by INFN of Naples with the collaboration of TechnoIn SpA. It is 1.2 m long and has a 24 cm diameter (Figure 1.14), when the steel shell is considered, while it is 1 m long and 20 cm of radius naked. The dimensions have been chosen to fit a 25 cm in diameter drilled well; indeed large wells present logistical difficulties and higher costs, while a 25 cm well can be drilled at a reasonable cost with ordinary drilling machines.
On the way of the past expertise, the new borehole detector is composed of plastic scintillators, optically coupled to Silicon photomultipliers. The scintillators have been realized in two different shapes: common bars, surrounding the detector in parallel to the axis of the cylinder, and arcs, in groups of four covering the circumference of the cylinder transverse sections

Figure 1.14: Borehole Cylindrical detector naked (left) and inside the steel shielding (right).

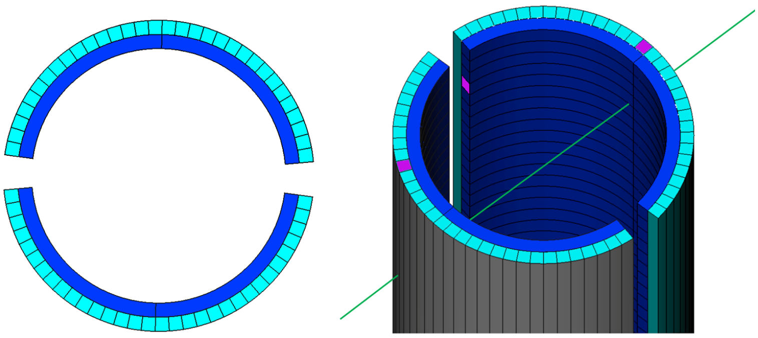

Figure 1.15: Arrangement of the scintillating elements in the cylindrical detector.

(see Figure 1.15). Considering a cylindrical coordinates system, represented in Figure 1.16, the bars measure the ϕ coordinate, while the arcs, arranged concentrically with respect to the z-axis, provide the z-coordinate of the impact point of the muon. The bars have a rectangular section of 8.5 mm $\times$ 6.5 mm and are 1 m long. Arcs are 15 mm thick with internal and external radius of 83 and 93 mm respectively (Figure 1.17). Every arc subtends an angle of about 83°. The whole detector consists in 256 arcs and 64 bars for a total of 320 scintillators elements arranged in two semi-cylinders. The bars are coupled to SiPMs at both ends. The arcs are read only from one end, while the other end is covered with aluminum tape, to increase the light collection and avoid the cross talk between two arcs facing each other. The total amount of SiPMs is therefore 384.
The scintillators are housed in racks designed specifically to be the skeletron of the detector and realized in Acrylonitrile

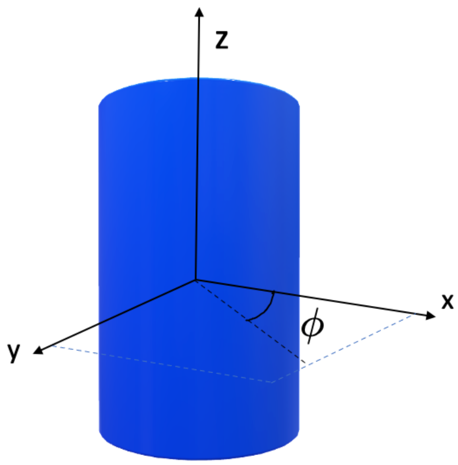

Figure 1.16: Coordinates describing the cylindrical detector.

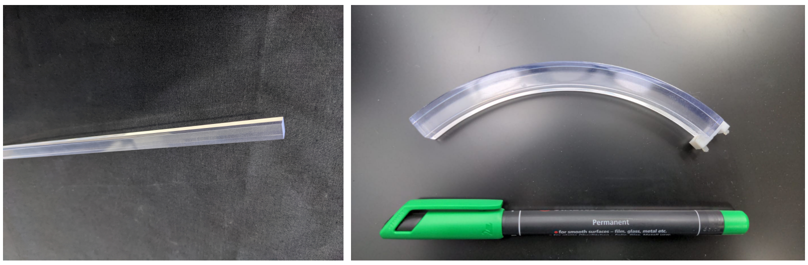

Figure 1.17: The scintillator elements. Left: one of the bars. Right: one of the arcs.

Butadiene Styrene (ABS) with a 3D printer. The complete housing structure is composed of 8 equal semicylindrical racks, a single rack is shown in Figure 1.18. The full length of a semicylinder is covered by four racks piled up. Each semicylinder has its front-end electronics installed in the cavity created by the arc curve (Figure 1.19).

The photosensors

Scintillator elements often are equipped with wavelength shifting fibers running along the length of the strip, to improve the light transmission; but in the case of the cylindrical detector we preferred a direct coupling between the photosensor and the scintillator to reduce costs and simplify production; scintillators are used as light guides, with overall excellent performance.
As light sensors, the S13360-3050PE SiPMs, manufactured by Hamamatsu, have been chosen. They are surface mount sensors, with a 50 μm cell pitch and an active area of 3×3 mm^2, that is about a tenth of the section surface of the scintillators. Even if the light gain would be improved by covering the whole scintillator surface by the photosensor, the occurrence of the dark counts and costs of the devices limit the choice of the size of

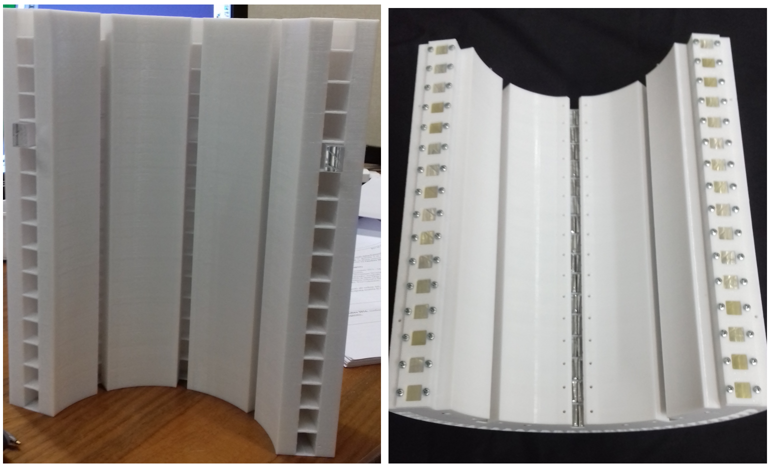

Figure 1.18: One of the racks used as skeletron of the cylinder. The total number of used racks is 8, divided in 2 stacks of 4. They were realized in ABS.

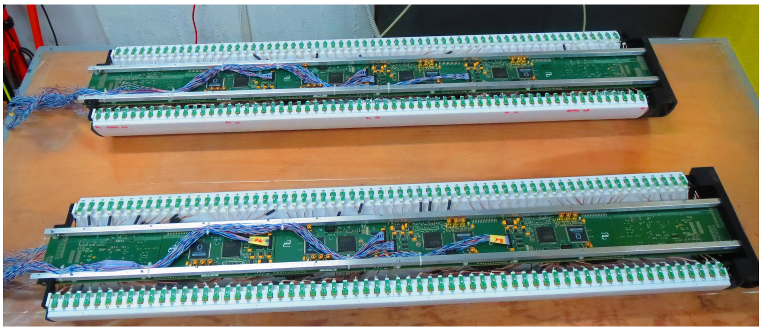

Figure 1.19: The two semicylinders before the assembly of the detector. The corresponding front-end electronics are placed in the cavities of both part.

the SiPM photosensitive area. It has been proved by laboratory measurements that this SiPMs coupled with the scintillators are capable of gain enough signal light compared to the level of dark counts. The photosensors are soldered onto dedicated printed circuit boards (PCB) and connected to a two-pin connector mounted on the same PCB (Figure 1.20).

Data Aquisition and Trigger Logic

The scintillators are read-out by 12 slave boards, each of which hosts 32 SiPMs channels. Each group of 32 arcs housed in the same rack are connected to the same board, for a total of 8 boards dedicated to the arcs and 4 boards to the bars. The whole front-end system [22] consumes only about 30 W, that is low enough to be supplied in a typical environment where the detector is thought to be installed. The boards are equipped with the EASIROC chip [19] developed for the SiPM readout. The chip preamplifies and shapes the signal, using a sample and hold technique and stores the analog information relating to the number of photons released in each of the scintillators, producing a fast logical signal, called Local Trigger (LT), when at least one of the 32 inputs exceeds a settable threshold level.

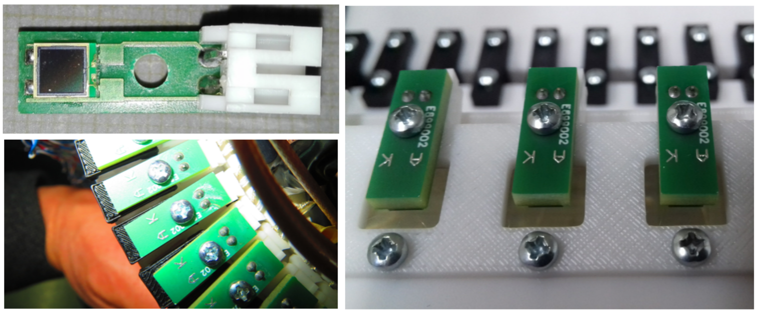

Figure 1.20: Top left: the SiPM installed on the PCB. Bottom left: SiPMs installed on the bars. Right: SiPMs installed on the arcs.

The Global Trigger (GT) is managed by the Master board, where an ARM single-board computer is embedded. The trigger logic requires a single muon hit, that is identified as the coincidence of a signal of at least one bar and one arc of the same semi-cylinder so, if A1 and B1 are the ORs of the arcs and bars respectively of the first semicylinder while A2 and B2 are the same quantities but for the other semicylinder, the trigger logic can be written as: $(A1 \cap B1) \cup (A2 \cap B2)$.
In Chapter 5 performance tests and first applications of the borehole cylindrical detector are presented.

1.3 Background sources

A muon radiography experiment is based on a precise measurement of the muon flux. It is thus necessary to avoid any background contaminations.
The most likely sources of background are events produced by hits of spurious origin, either temporally correlated or not. Uncorrelated hits may be due to dark counts or to independent particles crossing different layers of the detector within the trigger time window. A reduction of this kind of background can be achieved by restricting the required time window between the hits or applying tighter constraints in the alignment of the track. Correlated hits may be generated by particles produced in the same shower; in this case a Time of Flight measurement can help to discover and reject those events [23].
Muon are not the unique particle types that reach the Earth ground, even being the most abundant; in fact, electrons and positrons are also present at the sea level, being produced in the electromagnetic component of the extensive showers of cosmic rays; they can thus represent a background source causing tracks not distinguishable from muons. A frequently adopted solution is the use of an absorber material, usually lead or iron, able to stop those particles or even to induce the generation of a particle

shower. In the latter case the event is rejected by measuring the hit multiplicity after the absorber or by registering a poor alignment of the hits.
Other possibile contaminations come from *albedo* muons. Upward going muons can reach the detector and be mis-identified. A Time of Flight (ToF) measurement allows to distinguish the time order of the hits and thus to avoid the mis-reconstruction. Albedos are also muons that get through multiple scattering inside the investigated body, exiting with a different direction respect to the entering one. This effect affects in particular objects with thicknesses of the order of kilometers, such some volcanoes. The scattered muons are an irreducible component of background: for muons that are still down-going after been deflected, of this contribution can be applied only on the base of simulations.
A solution to remove some non-signal events, as correlated particles hitting the detector simultaneously or backward coming muons, is to measure the Time of Flight (ToF). The Mu-Ray (sec 1.2.2) and MURAVES (sec 1.2.3) front-end electronics are capable of measuring the ToF. Some laboratory tests on the Time of Flight system, conducted on one of the MURAVES hodoscopes, are described in the Appendix A.

Muon Radiography's state of art

2

Muon radiography is a relative young field of applied particle and nuclear physics; lots of possible applications have been developed during the last decades, and many others are under development. The very first usage of this technique dates back to the 1955 when E. P. George measured the overburden of a tunnel at the Snowy Mountains Hydro-Electric Scheme (Australia) with a Geiger detector [24].
A cornerstone of muon radiography applied to archaeological studies is represented by the work of the Nobel prize L. Alvarez in 1973 [25]. He used a bubble chamber to scan with cosmic muons a part of the Chephren's Pyramid to search for burial chambers, already discovered in the Cheope's Pyramid. The result was that no relevant signals had been observed in that part of the pyramid, so the experiment confirmed the absence of burial chambers in the Chefren's Pyramid.
After a first period in which the applications exploited mainly the muon radiography by absorption, more recently also the deflection of muons (muon tomography) has been used to design new applications. Nowadays more and more groups around the world are working on this research field.

2.1 Volcanology applications

After the pioneering experiment of L.W. Alvarez, the technique has been refreshed and suited to volcanological applications. If the volcano's typical thicknesses are not prohibitive ($\lesssim 1000$ m) muon radiography can be a valid help, together with standard geophysical methods, to the understanding of the possible eruptive modes of the volcano. Muography is independent of the geophysical model, and directly measures the density length (density × path length). If the path length is determined from topographic information, the measurement gives the average density along the path line of cosmic-ray muons. By measuring the muon absorption rate a small change in density due to the existence of either less-dense or more-dense areas can be

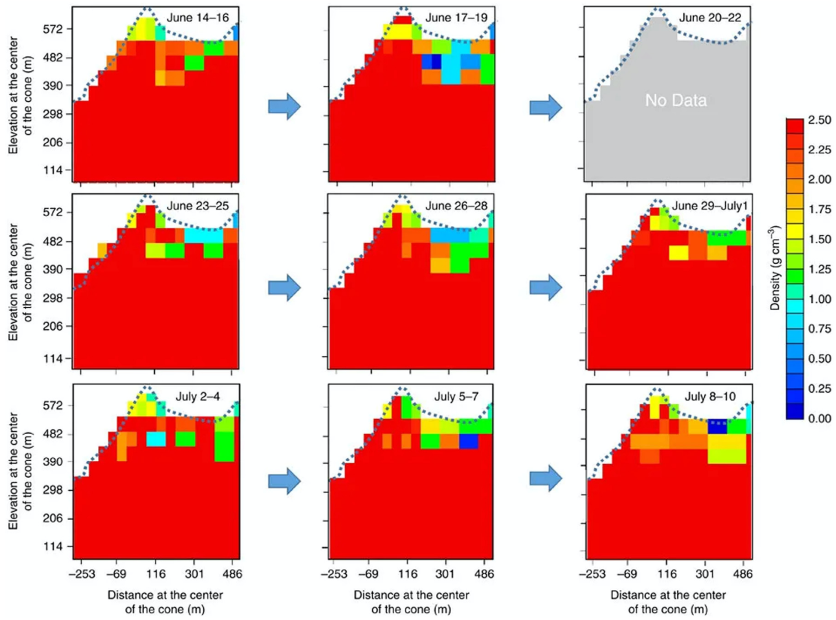

Figure 2.1: Magma dynamics during the Satsuma-Iwojima eruption. The plots show the angular distribution of 1 σ (68% CL) upper limit of the average density along the muon path. The frame rate is 10 frames per month. The data were not taken during 20-22 June due to a blackout. Horizontally adjacent two bins were packed in order to achieve higher and more accurate statistics. The elevation and horizontal distances at the centre of the cone are shown.

detected. Furthermore, in some cases muography could give realtime hints of possible modifications of the structure, due, for instance, to the magma rise, which could be precursors of a new eruption.

In 1994 the use of muography to scan the body of a volcano was proposed for the first time by a japanese group of scientists. The idea was to use a simple tracking system made of plastic scintillator bars to measure the muon flux across the Mt. Tsukuba. The technique was found to have the potential to spatially resolve the internal structure of a volcano with higher resolution than the conventional geophysical techniques.

Some years after this first approach at Mt. Tsukuba, other volcanoes have been investigated with muon radiography in Japan. In [26] results obtained at Mt. Asama, using ECC emulsion detectors, are reported and represent one of the first proofs of the effectiveness of muography in volcanological applications.

Eruption processes are preceded by magma motion in a conduit. Visualizing magma dynamics is often a key component to understand eruption patterns. In 2013 for the first time, evidence of the magma dynamics in a volcanic conduit manifested in muon radiography data, as presented in [27]. This result demonstrates that muon radiography can be potentially used as a tool to detect hints of eruptions. The experiment has been conducted at the small-scale Satsuma-Iwojima volcano, in Japan. The apparatus needs an adequate time resolution to perform rapid time sequence radiography considering the low intensity of the cosmic ray muon flux, fixed by nature, that requires long acquisition exposures to obtain adequate muon transmission image contrast.

In the case of Satsuma-Iwojima, muons reach the detector after passing a maximum depth of 800 m in the rock ($\rho \sim 2.0$ g / cm^3), from the direction of 264±17 mrad. It means that the detector collects 1.75 muons per day in each bin (33 × 33 mrad). If the volcano conduit is filled with magma of the same density, this path length will increase to 1200 m and the muon count will be reduced to 0.37 muons per day. This difference between an empty or full conduit can be detected in 3 days at a 2σ (95%) confidence level (CL). The results are summarized in Figure 2.1.

Other groups in Europe are successfully applying muon radiography to study volcanoes.
In France two independent groups have investigated the suitability of the technique by applying it to two different targets: the *La Soufriere of Guadeloupe*, an explosive subduction volcano in the Lesser Antilles holding one of the most hazardous volcanic hydrothermal systems in the world, and the *Puy de Dome*, an extinct volcano with an altitude of 1465 m a.s.l. and a lateral extension of more than 2 km at the base. Even if the last one could seems not of great interest for a geological investigation, it has been chosen by TOMUVOL and Mu-Ray collaborations [16] as *test site* for the development of muon radiography because it is isolated, so that there is no muon absorption from other structures, the size is moderate enough allowing measurements of a large part of the edifice, and can be observed from many locations, most of them with infrastructure reachable by roads and served by electricity.
The study of La Soufrière de Guadeloupe has been conducted by the DAPHNE group exploiting a plastic scintillator based detector with three XY planes of 50 × 50 cm^2 area. Volcano density structures are traditionally studied with gravity data, but 3-D models solely based on these data are highly non-unique and low resolution, especially since field conditions often make it difficult to achieve a good data coverage. DAPHNE collaboration obtained the 3D image, reported in Figure 2.2 applying a jointly inversion of gravity data with muon data. The muographic data consists of three independent measurements, acquired from three telescope simultaneously. The joint of gravimetric and muographic data allowed to improve the resolution achievable using gravity data alone or muon data alone [28].
The DAPHNE collaboration also demonstrated that muon radiography allows to detect and characterize mass movements in shallow hydrothermal systems of low-energy active volcanoes. In [29] and [30] they present the measurement of density variations

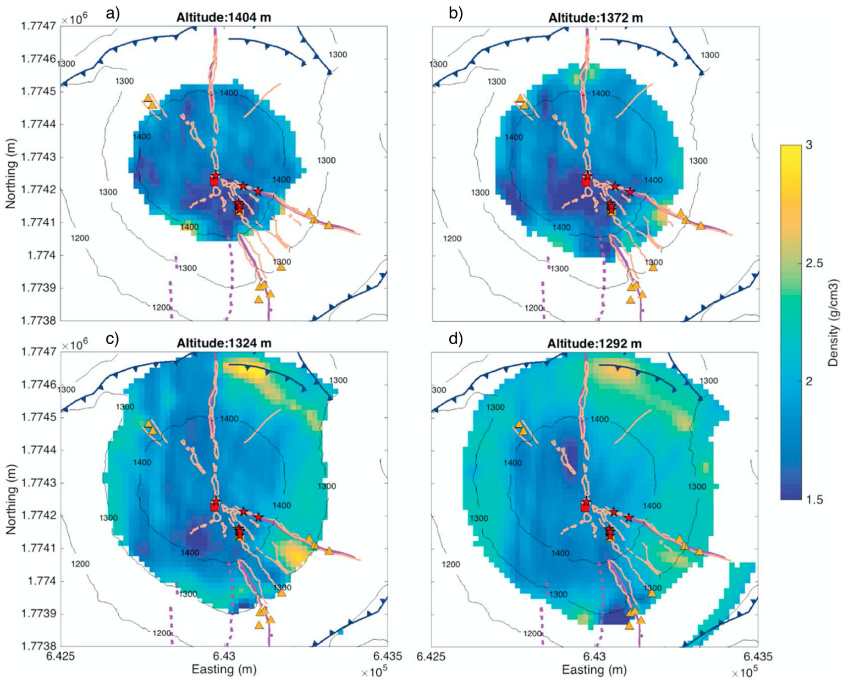

Figure 2.2: (a-d) Horizontal slices of the 3D density model obtained from the joint inversion of field muon and gravity data. A structural map is superposed to facilitate interpretation (orange lines: fractures; violet lines: faults; blue lines: collapse scars; orange symbols: past activity; red symbols: present activity; triangles: hydrothermal fluid exurgence; stars: active fumaroles; squares: boiling acid ponds).

in three domains of La Soufrière de Guadeloupe, and show how the combination of seismic noise monitoring and muon density tomography allowed to detect, with an unprecedented space and time resolution, the increase of activity (at timescales of few hours to few days) of a hydrothermal spot located 50 to 100 m below the summit of an active volcano.

Italy also hosts active and dangerous volcanoes, representing challenging targets for muon radiography applications. Three different volcanoes has been studied or are currently being investigated by different muography groups. A first example is the Mt. Etna, a very active strato-volcano in the Sicily island, that can present eruptions from its four summit craters or from vents or fissures. It has a height of about 3350 m, and the base is about 40 km in diameter. It has frequent activities that prevented the urbanization of the area around its base.

Mt. Etna has been studied with muon radiography the first time in 2010 [31] with a telescope consisting of two detection planes, both with 16 X and 16 Y scintillator strips, to form 256 pixels, each sized $5 \times 5\ \mathrm{cm}^2$. This first attempt had the principal purpose of test the possible use of a double-plane telescope avoiding a too high level of background. They found a marked bias on the observed flux, arising from false muon tracks. This background is caused by low-energy particles that, by chance, hit simultaneously the two matrixes of the telescope, leading to detection of a false positive. From this condition derives that a telescope with more than two planes is necessary to avoid fake tracks

contamination. However a rough estimation of the probability to have this accidental tracks has been evaluated and the result is compatible with the observed measurement. In spite of the huge amount of background in the measurement, that is incompatible with an accurate estimation of the density distribution inside the volcano, an indication of a lower opacity region was shown, after the subtraction of the background as predicted by the synthetic model.
A new attempt was conducted by MEV experiment [32] . The MEV group developed a three-planes scintillator-based detector and tested it in the Monte Rossi site, an extinct volcano similar in shape and dimensions to the North-East crater of Mt. Etna. The test phase was successful, and the detector was moved to Mt. Etna to start real data acquisition. The principal drawback of the experiment is that the logistic conditions exclude the possible use of a lead wall or other shielding techniques to suppress background. For this reason the group is looking for the introduction of a time of flight measurement or of a Cherenkov based detector to discriminate forward muons from backward muons.
In the south of Italy, near the city of Naples, another volcano arises, the Mt. Vesuvius, considered one of the most dangerous volcanoes in the world due to the high level of urbanization of the surrounding area. Indeed, more than half a million inhabitants live inside of the so-called red zone around it. It's quiet since the last effusive eruption in 1944, but a new possible eruption could be very destructive for the urban centers nearby. This danger makes Mt. Vesuvius object of an intense investigation and monitoring. In the 2009–2012 period, the Italian National Institute of Nuclear Physics (INFN) funded a research and development project on muon radiography applied in particular to the study of Vesuvius. The Mu-Ray and Mu-Ray2 [33] [34] [15] were prototypes (1 m^2 of active area) realized and operated for a test run at the Vesuvius, in collaboration with the Italian National Institute of Geophysics and Volcanology (INGV). MURAVES experiment is a INFN-INGV new project funded by the Italian Ministry of Research and Education based on the experience of the Mu-Ray program. The experiment is taking data at the Vesuvius since summer 2019 when the first of the three hodoscopes has been installed on the site (see 1.2.3). The MURAVES commissioning and data analysis represents one of the main topics of this thesis; all the details are largely described in Chapter 3.
Another relevant volcano in Italy is Stromboli, a large stratovolcano of the Aeolian archipelago. A first image of the internal structure of the summit crater has been published in 2019 [35].

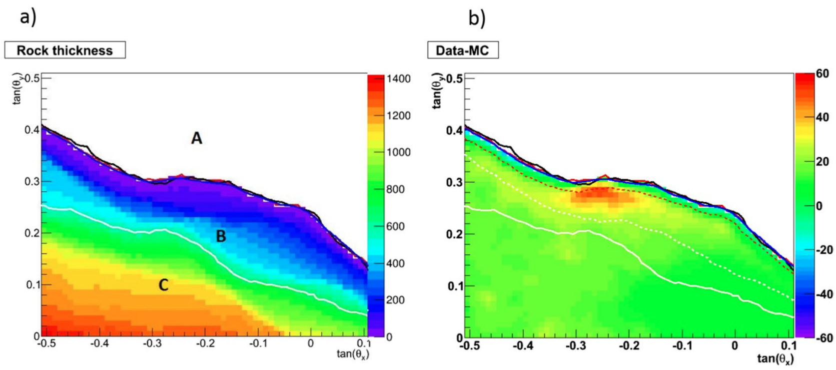

Figure 2.3: (a) Rock thickness and mountain profile as seen by the emulsion detector, given with 10×10 mrad^2 binning. The color scale is the rock thickness in meters. The white profile gives the statistical sensitivity limit, as defined in the text. (b) Difference between the observed muon flux and the one expected from Monte Carlo simulation over an angular range centered at crater region. Color scale represent muons counts. The average density ranges in between 1.4 and 2.2 g/cm^3 above the sensitivity limit.

The results have been obtained exploiting nuclear emulsion films. The exposure started on October 22, 2011 and ended on March 24, 2012 for a total duration of about five months, mainly in wintertime. At the end of the exposure, emulsions were removed from the site and distributed among the Napoli, Salerno and Tokyo scanning laboratories to be scanned. The experiment resulted in the observation of a clear muon excess respect to the expected flux in the crater zone (Figure 2.3); this excess translates in a corresponding low-density region.

2.2 Archaeology: search for hidden cavities

The already mentioned Alvarez's application of muon radiography [25] to the study of the Chephren's pyramid represents the first historically relevant result of this technique. The Nobel Prize was motivated to attempt this measurement by the evidence of an higher complexity of the internal structure of the near Cheope's pyramid; it was indeed conceivable to expect a similar structure in the other egyptian pyramids. Even if the experiment resulted in the observation of any unknown chamber in the explored region of the pyramid, Alvarez proved the possibility to investigate the presence of void regions inside a structure, such as pyramids, with the use of a muon telescope installed under the region to be inspected.
Muon radiography applied to archaeological heritage has the main advantage to be *not-invasive* respect to other methods, allowing to preserve the asset from any possible damage.
In year 2000, following in the footsteps of Alvarez, a research

group of the National Autonomous University of Mexico (UNAM), decided to explore the internal body of the Sun Pyramid at Teotihuacan in Mexico, the third largest pyramid in the world, built by Aztecs in the 14th century. After about a decade from the start of the experiment, the most significant result is the evidence of a lower density region, shaped as an equilateral triangle of 60 m side [36].

Recently, muon radiography has again been exploited to investigate the interior of egyptian pyramids. The Scan Pyramids collaboration has discovered a large void inside the Cheope's pyramid [37]. This large void has been detected with high confidence by three independent analyses related to three different muon detection technologies: nuclear emulsion and electronic detector installed in the *Queen's chamber* and gaseous detectors installed outside the pyramid. The emulsion detectors were installed in two different positions and the corresponding data has been then triangulated. Comparing the resulting muon radiographies with expectations, computed using a Monte Carlo simulation, they first confirmed that the large known structures (the Grand Gallery and the King's chamber) are observed and match what is expected and then showed an unexpected and significant excess of muons, observed from both the positions, in a region almost parallel to the image of the Grand Gallery. The statistical significance of this excess is higher than 10 σ at the highest difference direction suggesting the volume of the new chamber should be of the same order of the Grand Gallery signal. Two scintillator detectors were then placed in the Queen's chamber and confirmed the emulsion results. A third kind of instrument has been installed outside the pyramid to have another point of view to strongly affirm the presence of the void by the agreement of four measurements. Two micropattern gaseous detectors took data from the outside looking in the direction of the Grand Gallery, and close enough to each other that their data can be combined. The observed statistically significant excess confirmed the previous results from scintillator and emulsions detectors.

Another scenario of cultural interest where a muographic survey has been conducted is the underground of Mt. Echia, a little hill in the city of Naples (Italy). It is a headland with a maximum altitude of about 60 m a.s.l. and mainly consists of yellow tuff, a soft volcanic rock. This site hosts traces of an ancient history in its subsoil: in the course of centuries a very complex system of underground tunnels and cavities has been excavated and used to several different purposes. Applying muon radiography by positioning scintillator telescopes in the so-called *Bourbon Tunnel*, part of the accessible sector of the underground, led to the discovery and three-dimensional reconstruction of an hidden cavity. This experience, which is part of this Ph.D work, is described in details in Chapter 4.

2.3 Geological applications

Aside from volcanology, muon radiography has been successfully applied to other geological targets. One example is the investigation of mines; the subsurface density distribution can be modeled three-dimensionally if muon radiographies are performed from different points, and density anomalies can be reconstructed, searching for deep, compact ore bodies. A first measurement was performed by the CRM GeoTomography Technologies, Inc., a privately owned company spin-off from Advanced Applied Physics Solutions Inc. (AAPS, now TRIUMF Innovations), based in Vancouver, at the McArthur River mine, within the Athabasca Basin in Canada. They performed a muon tomography measurement using two superplanes of scintillator bars. Each superplane consists of two planes of bars oriented in orthogonal directions. The length and width of each plane are 2.1 and 1.1 m, respectively, and the thickness of each plane is about 6 cm. The data, acquired at a depth of about 600 m underground, showed a statystical significance of the uranium deposit signature larger than 5 standard deviations. In [38] they presented a 3D density inversion of the tomographic data, showing a good agreement with drill assay data from the deposit.
Other measurements of the same kind has been performed in the Pend Oreille mine, a Mississippi Valley Type (MVT) Zn-Pb deposit located in Metaline Falls in northeastern Washington State, USA at an elevation of approximately 700 m above sea level. The measurement has been conducted without prior knowledge of the presence or absence of ore bodies. The resulting 3D density distribution indicated a substantial volume of rock with higher density than the host stratigraphy above the survey location. Subsequently, a model of existing ore shells based on drill core data was provided and a simulation of the expected muon tomography data was found to be consistent with the muon geotomography measurements [39].

Applications in glacial geology have also been investigated.

An example has been presented by Nishiyama *et al.* in [9], describing the study of the bedrock geometry beneath the Aletsch Glacier situated in the Central Swiss Alps. The shape of the bedrock underneath alpine glaciers bears vital information on the erosional mechanism related to the flow of ice. So far, several geophysical exploration methods have been proposed to map the bedrock topography though with limited accuracy. Detectors made of emulsion films have been installed at three sites along the Jungfrau railway tunnel and measured the shape of the bedrock under the uppermost part of Aletsch Glacier (Jungfraufirn). A digital elevation model (DTM) of the mountain allowed to evaluate the total thickness L (rock + ice) of matter crossed by muons for each direction. The measurement of the attenuation allows the determination of the average density ρ that is related to the rock bulk density ρ_{rock}, known by samples of rock, and the ice density ρ_{ice} through the relationship:

$$\rho = x\rho_{rock} + (1 - x)\rho_{ice} \tag{2.1}$$

The experiment resulted in the measurement of a bedrock with a steep flank that dips at 45° ± 5° and strikes at 225° N underlying the the uppermost part of Aletsch Glacier. This result demonstrated that muon radiography can be a complementary method for determination of the bedrock topography in a steep glaciated environment if underneath tunnels or suitable detector sites are available.

2.4 Industrial and security applications

Several other applications of industrial and security interest have been or are meant to be developed concerning both the absorption and the multiple scattering techniques. One example consists in the monitoring of blast furnaces. In the context of the Mu-Blast project [40], funded by EU, the capability of muon tomography to provide information on the distribution of the different components present in a blast furnace burden (coke, burden and reduced metal), during operation, has been investigated. As explained in Chapter 1, measuring the deflection of muons, the linear scattering density (LSD) of different materials can be distinguished, thus the different material distribution inside the furnace body can be highlighted. The analysis of simulation data has shown that good images can be obtained with a complete detector coverage. Anyway this would imply great difficulties in

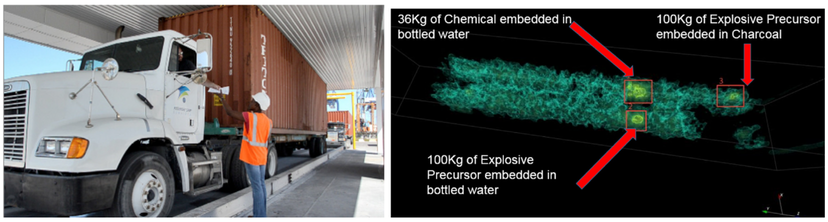

Figure 2.4: Left: large area detectors of Decision Sciences enable scanning of commercial trucks. Right: example of material anomaly detection in a three-dimensional image provided by the Decision Sciences' Discovery system [41] [11].

positioning of such large dimension detectors in an inhospitable environment as the proximity of a furnace. Thus, a more realistic setup has been simulated, consisting in a pair of detector smaller than 25 m^2, placed of the opposite sites of the blast furnace. The results have indicated that a measurement of individual particle momenta is necessary in order to obtain useful images of the furnace interior. Designing and simulating a detector capable to provide the muon momentum measurement, the results proved that useful images can be obtained in about 8 h.

A spin-off of the Mu-Blast project is the BLEMAB (BLast furnace stack density Estimation through on-line Muons Absorption measurements) project, which was funded by the EU and started in 2020. BLEMAB is proposed to investigate the imaging capability of the inner zone of the blast furnaces using a muon absorption detector that can realize a blast furnace muon radiography based on muon-transmission.

Another industrial application of muon scattering tomography is the transport and nuclear control; in particular it can be used to contrast nuclear contraband by control trucks and containers searching for possible heavy metals. This solution has been proposed by the Los Alamos group and became commercial. In fact, portals to apply muon tomography transport control have been realized, based on drift tube technology [41]. As it can be seen in Figure 2.4, a portal realized by Decision Sciences can scan an entire truck and material anomalies can be detected by the system.

In the context of transport control, the Mu-Steel European project [42] developed a solution to reveal the possible radioactive sources in containers transporting scrap metal to foundries. Foundry entrance is usually equipped with radiation portals but if the source is shielded by its transportation cask, realised with heavy metals as lead, the detection can fail. Consequently the source can be melted with serious consequences. Mu-Steel results proved the capability of a muon tomography system to intercept, in conjunction with radiation detectors, radioactive sources within a time compatible with the flux of trucks (~ 5 minutes scan).

2.5 Civil engeneering: applications of muon metrology

Muon metrology, as early described in section 1.1.3, exploits cosmic muons tracks to verify detectors alignments. Recently this technique has been investigated to study the stability of structures as industrial press and historical buildings [13] [14]. A feasibility study for the monitoring of the structural alignment of a mechanical press was conducted in 2007 and described in [13]. The study is based on the development of Monte Carlo simulations; the performances of an ideal tracking detector, consisting of three 400 cm^2 sensitive layers, mechanically connected to the press, has been tested in the monitoring of possible changes in the body of the press. Results, based on a number of reconstructed muons corresponding to 1 week of data taking, showed that a performance comparable to those obtainable with standard alignment methods (such as laser scanners, theodolites, etc.) could be achieved.
The possible use of muon metrology has been inverstigated also in the control of historical buildings deformations. In [14] the vaulted roof of the Palazzo della Loggia, in the town of Brescia (Italy), has been used as exemplary case. The authors considered a simpler scenario, based on a system of 2 tracking detectors, consisting of three 400×400 mm^2 sensitive elements each. The sensitive material is made of scintillating fibers orthogonally oriented. A 15 cm thick wooden layer (simulating the ceiling of the Salone Vanvitelliano within Palazzo della Loggia), was interposed between the detectors. The results show that accuracies on the relative position between the two telescopes can be of the order of 1 mm with few days of data takings. Performance is found to be comparable to those of other monitoring systems, with few potentially appealing features, such as the applicability also in presence of interposing structures and the limited invasiveness.

More details and references related to the applications briefy described here or not mentioned for brevity, are available in the review [11].

3 MURAVES: MUon RAdiography of Mt. VESuvius

3.1 Purpose and motivations

Mount Vesuvius is an active volcano in the south of Italy near the city of Naples. It is considered one of the most dangerous volcanoes in the world due to the high probability to manifest an explosive eruption. Despite the hazard, the region surrounding this volcano is highly populated and urbanized; this keeps lots of people in danger and makes the monitoring of volcanic activity crucial to avoid possible catastrophes.
The history of Vesuvius is characterized by several explosive eruptions. The most famous eruption is the Plinian eruption that destroyed Pompeii in the 79 b. C. and led to the collapse of a large portion of the volcanic edifice, forming the Mt. Somma caldera, within which the Vesuvius cone emerges.
The eruptive activity among years changed the morphology of the volcano; in particular several explosive eruptions caused the collapse of the crater (Figure 3.1). The last eruption manifested in 1944, starting with an effusive activity causing a lava overflow, and terminating with an explosive eruption after which the crater took the aspect on the right in Figure 3.2. The explosive eruption caused a deposition of high-density lava on the NE side of the volcano, and an incoherent and low-density deposit on the top of the volcano.
In this scenario, the measurement of the density distribution inside the body of the Vesuvius becomes of high interest to better understand the past explosive dynamics and the possible future activity. Muon radiography can reveal the density distribution inside the volcano. Furthermore, muographic results can be combined with standard gravimetric measurements to improve the information achievable from one method alone.
The MURAVES (MUon RAdiography of Mt. VESuvius) experiment aims to apply muon radiography to the summit of the Vesuvius. The project is a joint activity participated by the Istituto Nazionale di Geofisica e Vulcanologia (INGV), the Istituto Nazionale di Fisica Nucleare (INFN) and the Universities of Naples "Federico II" and Florence, and is financed by the Italian Ministry of Education, Universities and Research. The collabo-

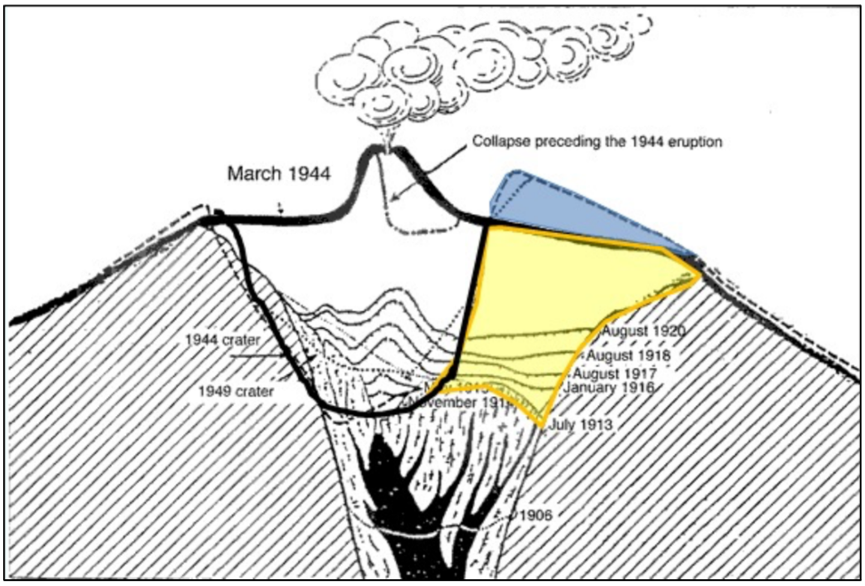

Figure 3.1: Evolution of Vesuvius crater between 1906 and 1944 from observations of Malladra and other researchers of the Osservatorio Vesuviano [43].

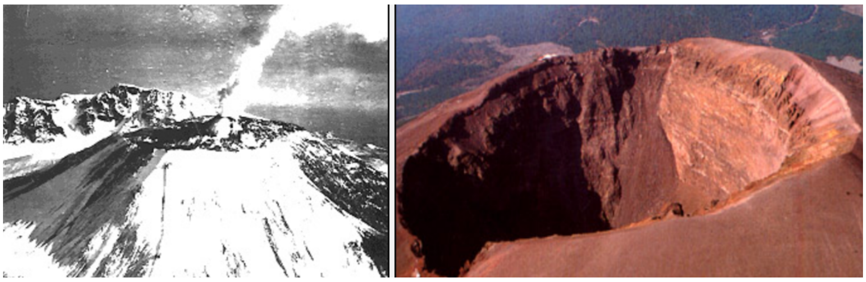

Figure 3.2: The crater of the Vesuvius before 1944 eruption (left) and as it appears now (right).

ration follows the experience gained within the previous INFN R&D project Mu-Ray, started in 2009 that led to the realization of the first hodoscope prototype (see section 1.2.2 and Chapter 4).

As described in section 1.2.3, the MURAVES telescope is an array of three identical muon trackers each composed of 4 XY stations of 1 m^2 sensitive area. The sensitive elements are scintillator bars with an optical fiber inside, running longitudinally, read out by SiPMs. Each muon tracker is the advanced version of the Mu-Ray hodoscope.

The experiment, the installation on the site, the data analysis and the up-to-date results are presented in the following.

3.2 The *in situ* laboratory

The MURAVES apparatus is described in details in section 1.2.3. A container of 45 m^2 area (Figure 3.3), has been built on a flank of Mt. Vesuvius at about 600 m a.s.l. The site has been chosen to be easily accessible and to have the best signal-to-noise ratio (evaluated with Monte Carlo simulations). The location and ori-

Figure 3.3: The container placed on the volcano at 600 m a.s.l.

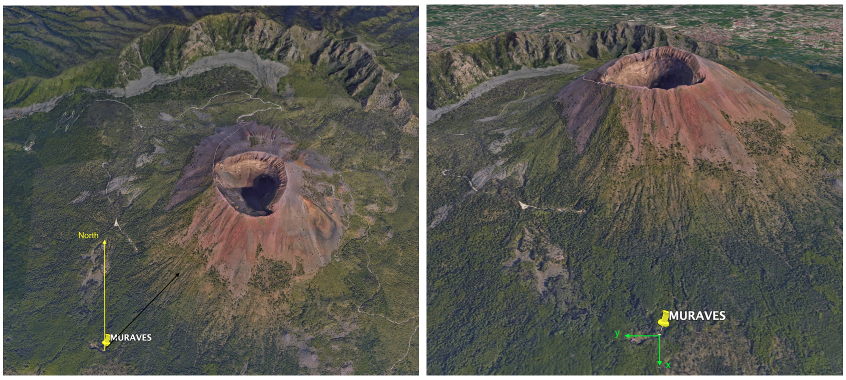

Figure 3.4: Left: the MURAVES laboratory position; the central line of sight of the telescope is represented in respect to the North direction. Right: the Mt. Vesuvius as seen by the MURAVES telescope; the xy axes of the MURAVES frame are also drawn.

entation of the container makes the acceptance of the hodoscopes maximum in the direction of the volcano's crater. In Figure 3.4 the position of the laboratory is indicated; the central line of sight of MURAVES is rotated respect to the North of an angle $\sim$ 45 degrees.

Inside the container, four spots are arranged to install the muon hodoscopes; each of the spots can host a lead wall, being equipped with a concrete platform that rests directly on the ground, avoiding pressing the container floor. The lead is interposed between the last two stations of each tracker. The first three stations of each hodoscope are mounted on an iron support, designed to fix distances between stations and their elevations from the floor, and necessary to freely move the detectors from one spot to another without changing the relative geometry. Figures 3.5 and 3.6 shows the interior of the container and clarify the detectors and lead walls arrangements. Three of the four spots are intended to look toward the volcano, while the fourth is devoted to the *calibration* data acquisition. To *calibrate* the detector means to estimate the incoming muon flux from open sky, as it would come in absence of the volcano. This condition is approximated by reversing the detector orientation, pointing to the opposite direction, where only sky is encountered by muons

Figure 3.5: View of the container from the inside.

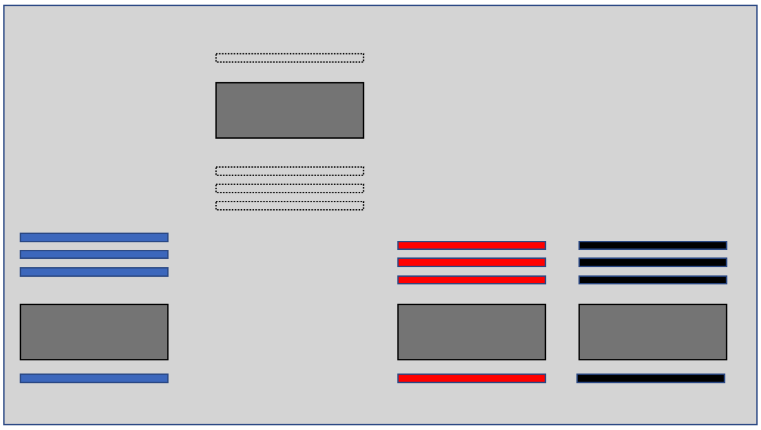

Figure 3.6: Schematic representation of the container plant. Four spots have been realized to install the hodoscopes, three of which looking toward the volcano (blue, red and black rectangles) and one looking toward open sky (dotted contour rectangles) for calibration acquisition. The dark gray boxes represent the lead wall.

before reaching the telescope, assuming the isotropy of the flux. Figure 3.6 shows a scheme of the container plant.
The telescope is low-power consuming; each hodoscope needs about 30 W to be fully functioning; this power is supplied by a system of solar panels installed on the roof of the container and connected to an array of batteries (Figure 3.7), which guarantee the night functioning of the apparatus.

3.2.1 Online monitoring

Due to the inconvenient logistic of accessing the site, the MURAVES apparatus can be remotely monitored and controlled; the status of the power supply system can be monitored from the website of the Victron Energy enterprise [44], who furnished the energy system. Accessing the private area of the website, several informations about the status of the system are provided; such as the charge level of batteries, the power supplied by solar panels, the apparatus consumptions, and many other informations. Figure 3.8 shows an overview of the system over a month of

Figure 3.7: Left: system of batteries installed inside the container. Right: solar panels installed on the roof.

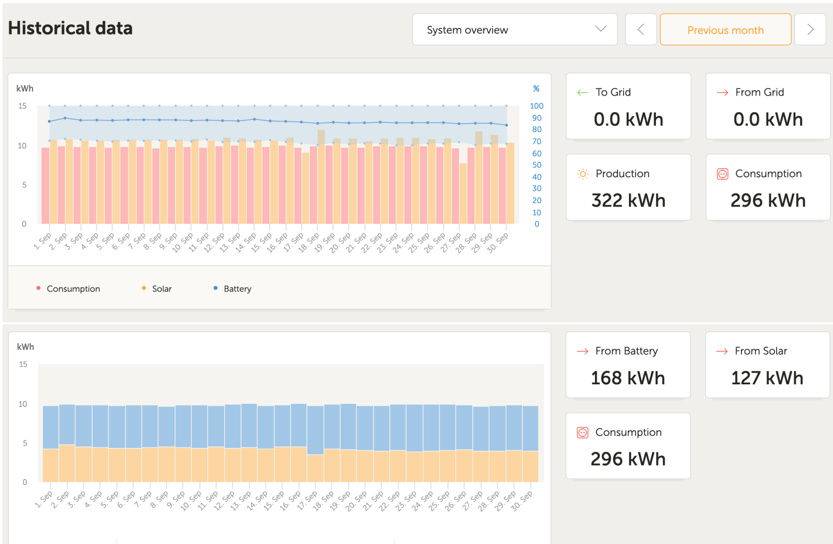

Figure 3.8: Top: overview of the power supply system from the Victron Energy website. Bottom: details of the apparatus power consumptions.

functioning. The solar energy produced is shown together with the power consumptions and the charging status of batteries; also the integrated consumptions are indicated over the chosen period. Furthermore, other detailed informations are available; as instance the distribution of power consumptions between solar power and batteries (Figure 3.8, bottom).
Aside the power system monitoring, also other informations useful to control the proper operations of the apparatus are achievable. An example is the trigger rate, the environmental and instrument temperatures, the humidity, the working point and other interesting distributions.
All the collected data, stored in a local storage unity, are remotely accessed and downloaded through a *rsync* protocol, in run-time.

3.3 Trigger and Data Acquisition

The trigger logic of the trackers is programmed defining a reasonable dynamics associated to a muon passage. An event is thus recorded if a signal is contemporary registered on the first

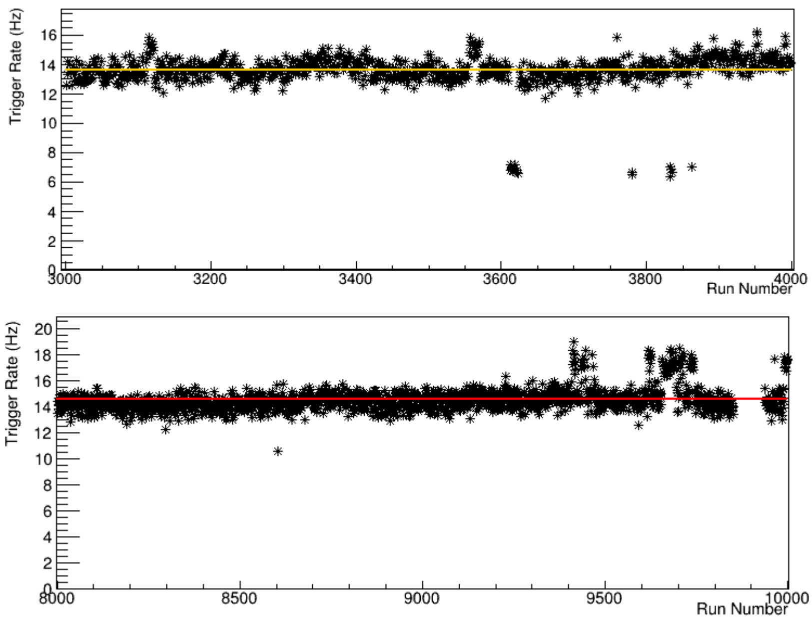

Figure 3.9: Trigger rate as a function of the run number of NERO (top) and ROSSO (bottom) detectors. The mean value of the first is 13.6 Hz while the latter is averaged on 14.5 Hz.

three planes of the tracker, of both z- and y- views. An energy deposit in a scintillator bar is considered a signal if it exceeds a tunable threshold, that in this case is set to 6 photoelectrons, based on the SiPMs gain in the actual conditions. In more details, considering M_z^i and M_y^i the OR of the 64 bars of the z and y views respectively of the i-th station of the tracker, the trigger logic corresponds to the AND of the first three stations:

$$\bigcap_{i=1}^{3} M_z^i \cap M_y^j \tag{3.1}$$

The data storage is organized in *runs*, packages of 40000 trigger events. In Figure 3.9 the trends of the measured trigger rates of NERO and ROSSO detectors are reported respect to the run number, for a bunch of subsequent runs. Each plot shows the measured values and the mean line superimposed. The trigger rate represents a good parameter to control the proper operation of the detector; if a run has a trigger rate too far from the local mean value, it is probably corrupted, due to some malfunctioning. Those runs are thus ignored.
The data acquisition of the MURAVES experiment is planned to last for a very long time, due to the large size of the volcano and the very low rate of muons, especially from lower elevation directions. The long exposure of the telescope means working in various environmental conditions. In fact, the temperature, humidity and pressure change both during the day and between the different seasons. The apparatus reflects these external variations in its operation. The dependence of the detector performances

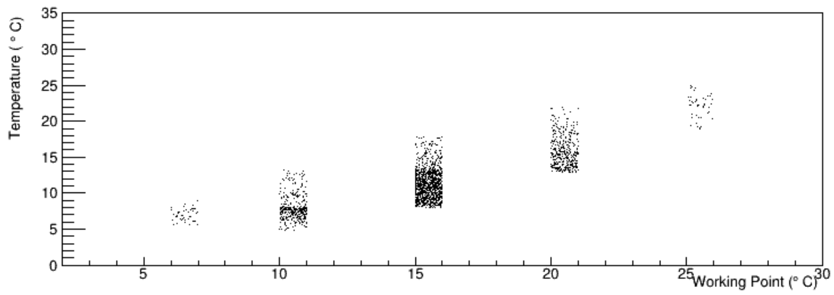

Figure 3.10: Environmental temperature as a function of the corresponding working point.

from the environmental changes must be kept under control. Several *working points* are thus defined and automatically set when significant changes occur. A working point is defined by a combination of temperature and bias voltage applied to the SiPMs. When the external temperature changes significantly, the appropriate working point is set and in consequence the temperature control system heats or cools the SiPMs. The temperature is chosen to be within 5-7 degrees from the external temperature, to avoid larger consumes and to stay safely distant from the dew point avoiding damages due to the possible condensation. The V_{bias} is consequently set, with the intent of maintaining the detection efficiency and the gain stable; to this purpose, the overvoltage $V_{ov} = V_{bias} - V_{bd}$ must be constant. Since the breakdown voltage increase linearly with the temperature, the bias voltage V_{bias} is increased or lowered to compensate V_{bd} fluctuations. Figure 3.10 shows the relation between measured environmental temperature and the working point temperature. Even if the system automatically changes the working point everytime it is needed, some performances variations have been observed between different working points. This is already visible by comparing the measured trigger rates. As shown in Figure 3.11 the distributions of trigger rates related to different working points are slightly different. It is observed for both NERO and ROSSO detectors. These variation needs to be accounted in the data analysis. For this reason the first attempt to a complete data analysis up to the density measurements has been conducted separating datasets related to different working points.

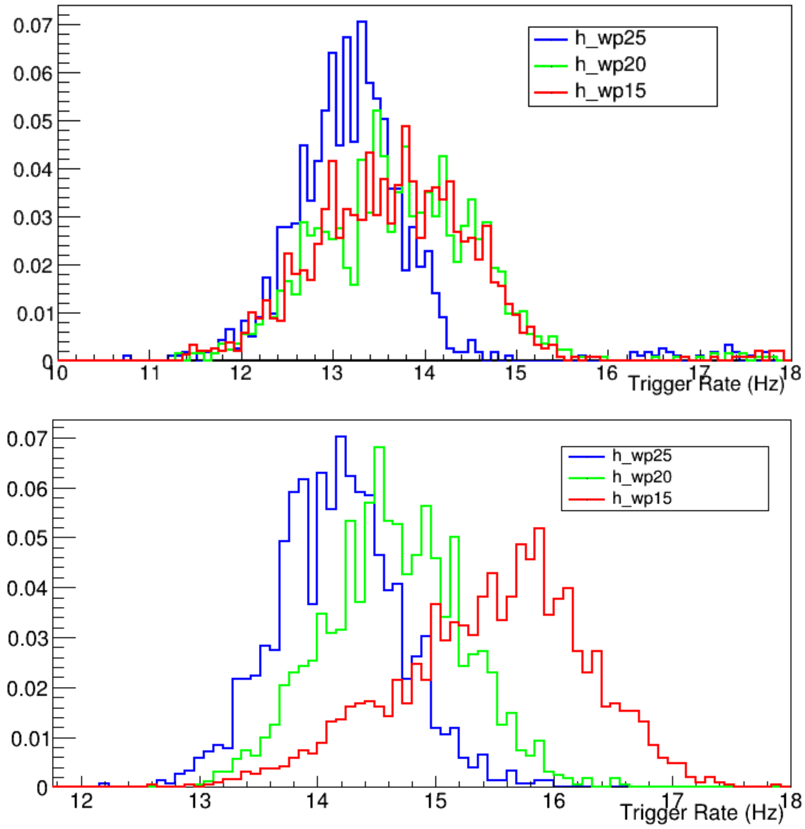

Figure 3.11: Trigger rate distributions for different working points. Top: NERO detector. Bottom: ROSSO detector.

3.4 Feasibility studies

As already mentioned, the MURAVES telescope has been installed at 600 m above the sea level, on a flank of the Vesuvius. As in can be seen in Figure 3.12, from this position muon that reach the detector after traveling though the body of the volcano comes from near-horizontal directions. The muon flux from these directions is strongly reduced respect to the vertical, as shown in Figure 3.13. Furthermore, the body of the Mt. Vesuvius is characterized by thicknesses in the range from the order of hundreds meters, in the summital part, to about 4-5 kilometers, in the bottom part. The rate of muons surviving the rock is highly suppressed when the thickness reaches the level of thousands meter, as shown in Figure 3.14. For these reasons, the evaluation of the density distribution along the body of the Vesuvius is a

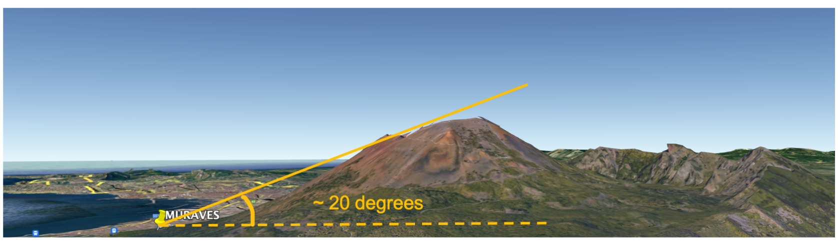

Figure 3.12: Pictorially representation of the directions of muons useful to image the body of the volcano.

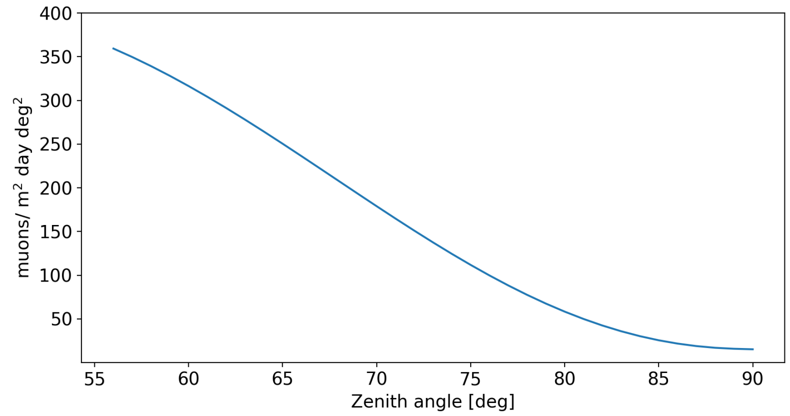

Figure 3.13: Cosmic-ray muons flux respect as a function of the Zenith angle. The flux is strongly suppressed from near-horizontal directions respect to vertical directions.

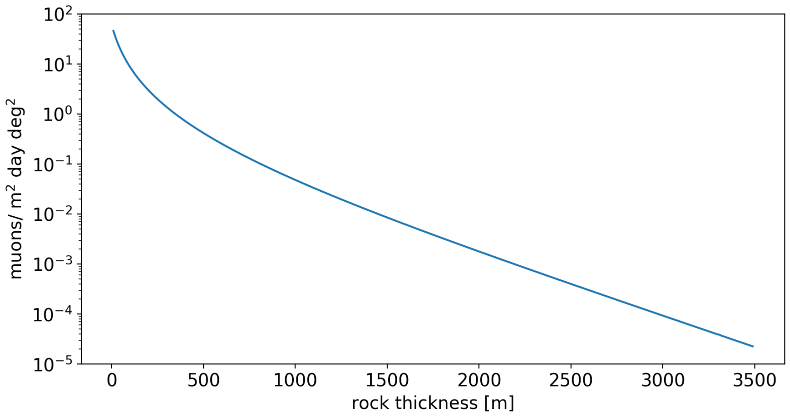

Figure 3.14: Rate of cosmic-ray muons escaping rock as a function of the rock thickness.

great challenge for a muon radiography experiment.
The achievable spatial and density resolutions depend on the collected statistics, that means on the data-taking time. It is thus necessary to estimate the exposure time needed to reach the desired resolution, by accounting for the specific rock thicknesses in the game and the expected atmospheric muon flux from the directions of interest.
The cone of the volcano is characterized by typical thicknesses in a range from ~ 100 m, at the highest elevations, to $\sim 1000 - 1500$ m at about 15 degrees, while the bottom part is roughly wider, reaching thicknesses of the order of 4-5 kilometers; this means that different parts of the volcano need different times to be resolved with the same resolution.
In Table 3.1 the average thickness for several slices of Mt. Vesuvius corresponding to different elevations are listed. Considering a uniform density ρ=2.65 g cm^{-3} and a desired density resolution of the 10%, the needed times, for different spatial resolutions and thicknesses, are listed in Table 3.2. These estimations have been obtained following the discussion by Lesparre et al. in [45]. Fixed the spatial resolution and the thickness, a density variation of

Elevation (deg)	Mean Thickness (m)
20-21	90
19-20	290
18-19	490
17-18	720
16-17	920
15-16	1100
10-15	1500
5-10	2700
0-5	4050

Table 3.1: Average thickness of several slices in elevation of the Mt. Vesuvius.

Th (m)	90	290	490	920	1100	2700	4000
Δx (m)				ΔT (months)			
1	24.7	113.5	318.3	1345.6	2125.8	13596.7	69585.8
2	6.2	33.0	74.0	336.4	531.4	3399.2	17396.4
5	1.0	4.5	11.7	47.1	76.6	538.2	2754.4
10	0.2	1.1	2.9	11.8	40.8	134.5	688.6
15	0.1	0.5	1.3	5.2	18.4	59.8	306.0
20	0.1	0.3	0.7	3.0	10.4	33.6	172.1
25	0.04	0.2	0.5	1.9	6.6	21.5	110.2
30	0.03	0.1	0.3	1.3	4.6	14.9	76.5

Table 3.2: Time needed to reach a 10% resolution on density measurement. The estimations are listed for different spatial resolutions and thicknesses typical of the different slices of the volcano (see Table 3.1).

the 10%, $\delta\rho = 0.1\rho$, corresponds to a variation of the observed muons

$$\Delta N(\rho, \delta\rho) = N(\rho + \delta\rho) - N(\rho) \tag{3.2}$$

where $N(\rho) = \Phi(\rho)\Delta T$ depends on the acquisition time. To distinguish the density variation $\delta\rho$ the condition

$$\Delta N > \delta N = \sqrt{N} \tag{3.3}$$

must be satisfied. The quantity $\delta N = \sqrt{N}$ represents the uncertainty on the measured number of muons N. The minimum time needed to reach the desired resolution is

$$\Delta T_{min}(\rho, \delta\rho) = \frac{\sqrt{N}}{\Delta\Phi(\rho, \delta\rho)} \tag{3.4}$$

and depends on the expected flux in the hypothesis of a density ρ. More details can be found in [45]. Times estimated in Table 3.2 refer to the full telescope sensitive area (3 m^2) and does not account for the flux reduction related to the detector efficiencies. These results demonstrate how the experiment is challenging. In fact, a statistics corresponding to more than 2 years is needed to reach a spatial resolution of 1 m and a density resolution of the 10% on the very superficial part of the summit (elevation higher than 20°) where the thickness is under 100 m. It is also clear that the lowest slopes of the volcano are highly prohibitive, indeed the estimated time necessary to resolve thicknesses of 4000 m with a spatial resolution of 30 m is over 7 years. In light of the above discussion, the experiment reasonably focuses to study the summit of the volcano.

3.5 Data Analysis

The goal of the experiment is to evaluate the density distribution of Mt. Vesuvius, measuring the flux of muons emerging from the volcano. The collected raw data need several manipulations before being ready to use. In the next few sections the data analysis steps and some preliminary results are described.

The first preliminary step of the data analysis is to convert raw data in readable informations. As already mentioned, data are stored as packages of 40000 trigger events, referred as runs. A text file is created for each run. It consists of 40000 rows, each fully describing a single event: board number, temperature, time stamp, and the 32 ADC values of each SLAVE board are written in the event-line.

3.5.1 ADC counts to PhotoElectrons conversion

A scintillating material undergoes to ionization when crossed by muons. This process yields some light, proportionally to the deposited muon energy. Photons, collected in the wavelength shifting fiber, reach the SiPM and convert in *photoelectrons*. The number of ADC counts is proportional to the number of produced photoelectrons. A dedicated control run is taken in random trigger mode before each data acquisition run, collecting 50000 events to be used to translate the ADC responses in the corresponding number of photoelectrons. The *1 phe* value, *i.e.* the ADC counts corresponding to a single photoelectron, and the *baseline* ADC value, called *pedestal*, to be subtracted from each ADC measurement, are evaluated for each channel from the corresponding ADC distribution resulting from the control run. An example of ADC counts distribution of an electronic channel is showed in Figure 3.15. As it can be seen, the distribution presents several peaks: the highest corresponds to the baseline value and must be subtracted from each measured value; the subsequent peaks correspond to the first, second, etc. photoelectrons and the

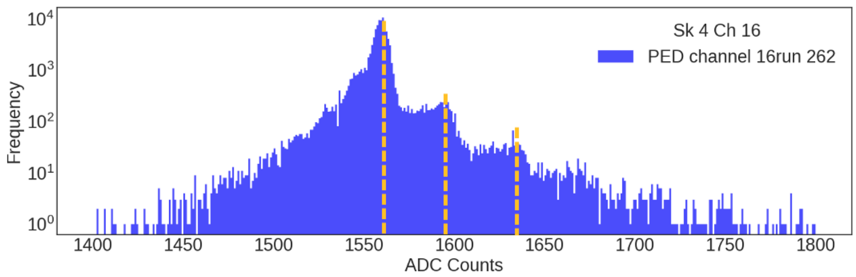

Figure 3.15: Example of ADC counts distribution of an electronic channel. The highest peak corresponds to the pedestal value, while the others to the first, second etc. photoelectrons.

distance between two adjacent peaks is the 1 phe factor. Once the baseline and 1 phe values have been obtained, the energy is converted in photoelectrons as

$$E_{phe} = \frac{N_{ADC}^{signal} - N_{ADC}^{ped}}{N_{ADC}^{1phe}} \tag{3.5}$$

In principle the ADC parameters should be stable in time. However, we observed some variations, often worsening, of the ADC spectra. This behavior is not equal for each channel; some channels presents worse effects than others which don't manifest significative modifications. It has been also observed that the worsening of the ADC distributions is related to the SiPMs themselves and not to the electronic channel. Due to these variations, the ADC to Photoelectrons conversion parameters are evaluated run by run, to avoid systematics in the energy deposit reconstruction. The electronic channels are 32×16 boards $\times$ 3 hodoscopes, that means 1536 channels, thus an algorithm, wrote in *python3*, is used to automatically obtain the conversion factor list, run by run, and insert them in the analysis chain. The algorithm searches for the highest peak and attributes the corresponding ADC counts to the pedestal value; then the difference between the ADC values corresponding to two consecutive peaks is considered as the 1 phe value. Sometimes the distribution is too smeared and the method fails; in this case the 1phe is posed equal to the closest channel for which the method succeeds. An example of this situation is shown in Figure 3.16. The algorithm also recognizes dead channels, and assigns a very high value (1000) as 1 phe, such that the corresponding contribution is automatically ignored. The typical ADC distribution of a dead channel is reported in Figure 3.17. As mentioned above, these parameters are quite stable, but they sometimes change when the operation conditions change. Figure 3.18 shows the ADC distributions of a board from the control data; for each channel, different runs (far in time, and corresponding to changes in environment conditions) are superimposed and demonstrate the

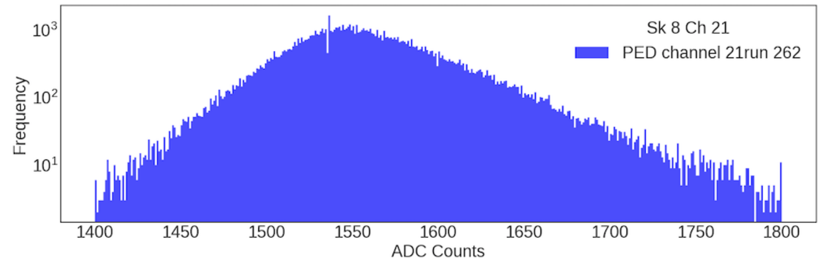

Figure 3.16: ADC channel with smeared dynamics. The channel is functioning, but the 1phe is not measurable; thus the 1phe value of the closest channel is attributed.

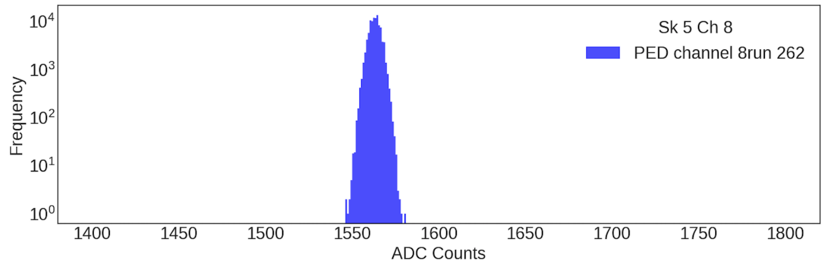

Figure 3.17: ADC counts distribution of a dead channel.

heterogeneous behavior of the spectra, that for some channels modifies more significantly than for others. In Figure 3.19, 1phes

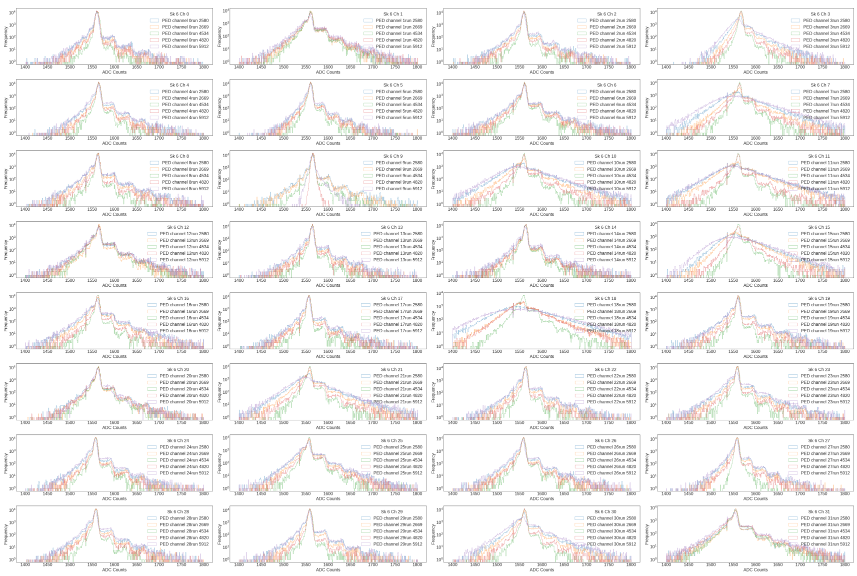

Figure 3.18: ADC pedestal distribution for the different channel of a board. Each channel show distributions corresponding to different runs.

of one board are reported in histograms, separated according to the working point. The distributions of three working points are showed in different colors: the red histogram corresponds to the 20°C working point, while the black and the blue ones correspond to 15°C and 25°C respectively. As it can be seen, the majority of the channels presents narrow distributions, while some channels are slightly wider, probably due to a smearing of ADC distributions, that partially hides the channel dynamics. It can be also seen that the distributions, and in particular the mean value, of the 1phe parameter, are slightly different between working points; it can be related to the voltage tuning applied to

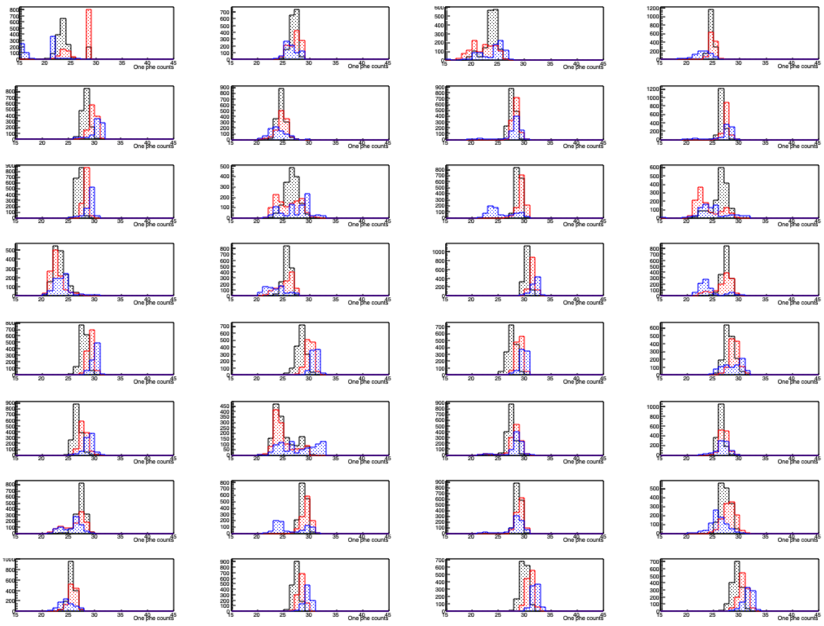

Figure 3.19: 1phe distributions of the 32 channels of a front-end board. Histograms are filled with the 1phes evaluated for the different runs; different histograms correspond to different working points: 20°C (red), 15°C (blue) and 25°C (black).

the devices when the working point is changed.

3.5.2 Track Reconstruction

The reconstruction of muon directions is crucial to obtain the correct image of the volcano and its interior mass distribution. An *energy clusterization* is first applied to the strips deposits. This procedure combines adjacent strips to construct energy clusters, to correctly assess the muon hit coordinates. Each strip deposit is considered if it exceeds an energy threshold, fixed to 6 photoelectrons according to the trigger threshold. The clustering algorithm is applied to the 64 strips of each view of each tracking station. A loop is performed over the strips: the first strip interested by a significant signal starts a new cluster; the subsequent strips are included in the cluster if they exceed the energy threshold. The cluster is completed and registered when the first strip not presenting a signal is encountered. The algorithm goes on and repeats the procedure when a new significative signal is encountered. When a cluster consists of a single strip, it is accepted only if its energy is higher than 10 photoelectrons. This is done to avoid single strips fired by dark counts. However, to adjust more precisely the position, in the single strip case, the two adjacent strips are included if they present a signal higher than 1 photoelectron. The effect of this regulation is clear in Figure 3.20 where the difference between the track position and the cluster position (residues) is showed in the case, taken as exemple, of the second station in the z-x view before and after the addition of the

adjacent strips to the single-strip clusters. This strategy is thus validated by the higher symmetry of the residues distribution with the addiction of adjacent deposits.
Each cluster is characterized by a total energy deposit and a

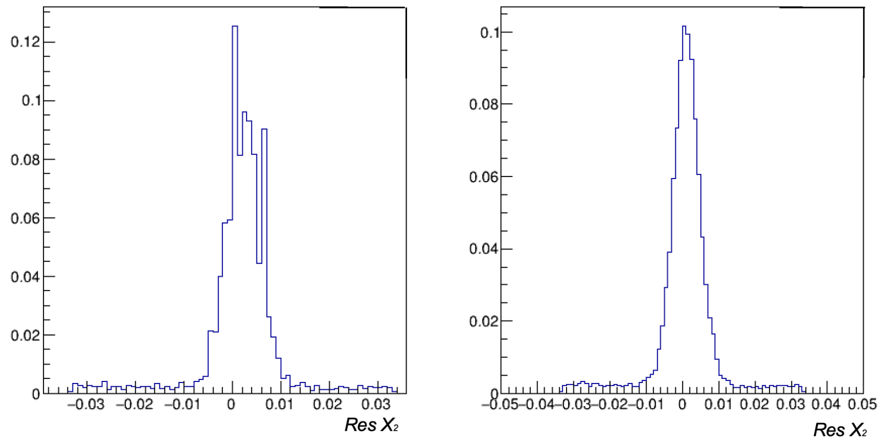

Figure 3.20: Residuals of clusters reconstructed on the second plane, vertical view. On the left the distribution before applying the finer tuning on the single strip clusters; on the right the post-tuning same distribution. The peaks present on the left disappear after the correction.

position. The former is the sum of the energies of the strips included in the cluster; while the latter is assessed with a weighted mean of the strips barycenter positions, where the weights are the strip deposits:

$$x_{cluster} = \frac{\sum_{strips} x_i E_i}{\sum_{strips} E_i} \tag{3.6}$$

The use of the formula in eq. (3.6) improves the spatial resolution. It can be applied to almost all the particles, since the triangular shape of the cross-section of the scintillator bars (see section 1.2.2) allows the particle to intercept, in most cases, at least two adjacent strips (see Figure 3.21). The energy deposit in each strip depends on the corresponding muon path length and on the distance from the fiber; this dependance helps to better evaluate the real intersecting point. The reached resolution has been measured and is described in section 3.5.4.
In Figure 3.22 the distributions of the strip energy deposits, of the strips involved in clusters, and of the reconstructed cluster energies are shown.
The clusterization algorithm is performed independently on

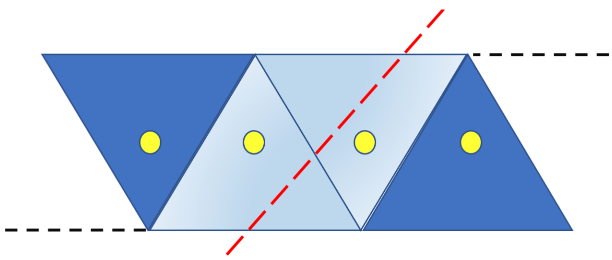

Figure 3.21: Scheeme of how a muon intercepts, in most cases, at least two scintillator strips thanks to the triangular shape of the bars. This feature is useful to improve the detector spatial resolution.

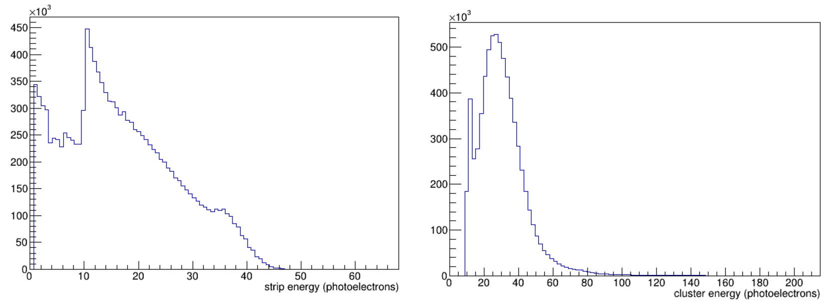

Figure 3.22: Left: distribution of the energies of cluster strips. Right: distribution of the energies of the clusters.

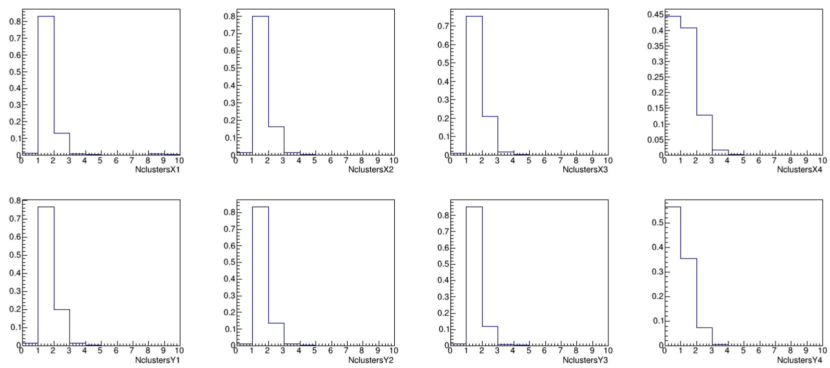

Figure 3.23: Number of reconstructed clusters. Top: z-view planes. Bottom: y-view planes.

both the z and y views of each station. Histograms in Figure 3.23 show the number of reconstructed clusters on each plane of both views. The plots have been obtained using an exemplary dataset of the Vesuvius data acquisition.
The most of the events, about the 93%, present at least one cluster on each of the first three layers simultaneously, while each view of each layer individually presents at least one cluster in the 99% of the events. Since the fourth layer is not involved in the trigger logic, it presents a cluster in less than half of the events, and simultaneous clusters on both z and y views are reconstructed in the 25 % of the events. In about the 23 % of the events all planes are interested by at least one cluster.
Once the clusters have been constructed on each plane, the tracking process can be performed. Planes *xy* and *xz* are considered separately to evaluate bi-dimensional tracks. The tracking procedure can be described by the following steps:

- all possible combinations of clusters from the first and third stations are considered;
- the linear function linking the two points is evaluated, and the coordinate on the middle plane is extrapolated;
- if a cluster closer than 5 cm to the expected position is found, a linear fit is applied to the three points;
- the best fit linear function represents the first track-candidate.
- Each of the obtained track-candidates is analytically extended to the fourth station: it is conserved if intersects

the sensitive plane and rejected if not. Thus, if any cluster exists, the closest one is associated to the track-candidate.

- A new linear fit is performed considering the four points. The resulting function is the final track-candidate.

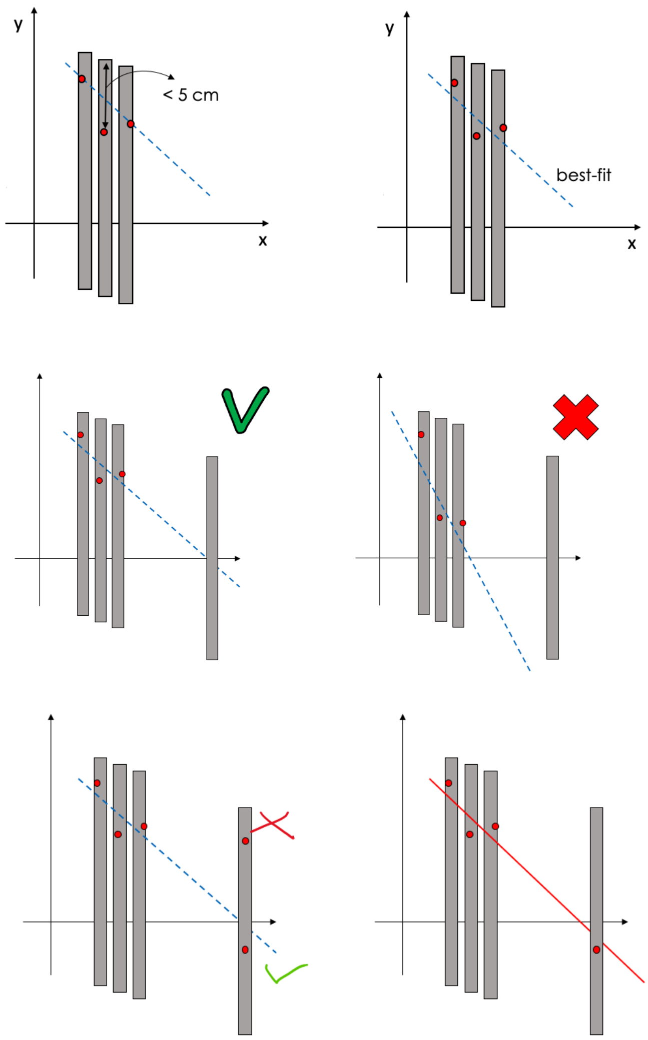

Figure 3.24: Steps of the tracking procedure of the MURAVES experiment. From top to bottom: a combination of clusters of the first and third planes is considered; a compatible cluster is searched in the middle plane and the best-fit track is evaluated. The track is accepted if intercepts the sensitive area of the fourth plane; the closest cluster, if exists is associated to the track. A new linear fit is performed involving four points.

The whole tracking procedure is summarized in Figure 3.24. The events presenting at least one track are ~ 5 % of the total triggers. The majority of these events (85%) present a single track; in those cases when more than one track-candidate are obtained, only one is maintained. The criterion to chose the best track needs to be as independent as possible from the specific detector performances and from the environment parameters. The degree of agreement of data with an hypothesized model is usually represented by the quantity:

$$\chi^2 = \sum_{i}^{n} \frac{(x_i^{model} - x_i^{data})^2}{\sigma_x^2} \tag{3.7}$$

called *chi-square*. Applied to the track-fit, a lower chi-square implies a better alignment of the clusters, thus this parameter can be considered to choose the best track when more than one have been reconstructed in the same event. The fourth plane of the MURAVES tracker is positioned behind the lead wall, that in some cases causes the deviation of the particles. The best track is chosen as the one with the minimum value of the quantity:

$$\chi^2_{3planes} \cdot |x_4^{model} - x_4^{data}| \tag{3.8}$$

where the first term accounts for the alignment of the clusters of the first three planes, and the second one represents the displacements of the cluster of the 4th plane respect to track reconstructed with the first three planes.
Once a single track has been chosen for each event, some quality selections have to be applied to the data. The criteria used in this work of thesis to select *golden* events are described in section 3.5.5.

3.5.3 Spatial Resolution

In this section, a method used to evaluate the spatial resolution of the telescope is proposed and described in full details.
The measurement of the spatial resolution on both z and y coordinates is necessary to apply the tracking procedure, and plays a crucial role in the evaluation of the track χ^2, on which the track selection criteria is based. Thus, a proper resolution has to be used to avoid any under- or over-estimation of this quantity.
The proposed method is based on the measurement of the muon passage point through the second plane: it is measured by of the sensitive elements of the plane, but can be also evaluated exploiting the positions measured on the first and third planes in the same event. Considering that an event consists in a muon traversing the whole detector, the linear function linking the two reconstructed clusters on the external planes, can be used to extrapolate the position of the muon through the second plane. This can be considered an expected position, s_2^{exp}. The difference between the expected position and the measured position is the residue:

$$Res_{s2} = s_2^{exp} - s_2^{cluster} \tag{3.9}$$

where s can be z or y.
Considering the spatial resolution on each coordinate equal for all the planes (there's apparently no reason to doubt about it) the

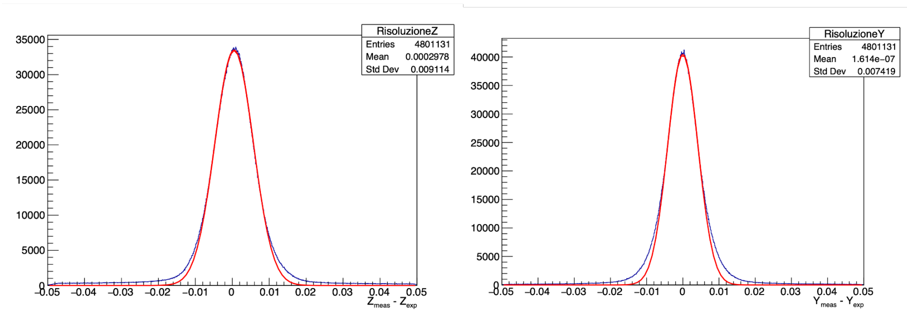

Figure 3.25: Residuals distributions of z (left) and y(right) (eq. (3.9)) of the detector ROSSO.

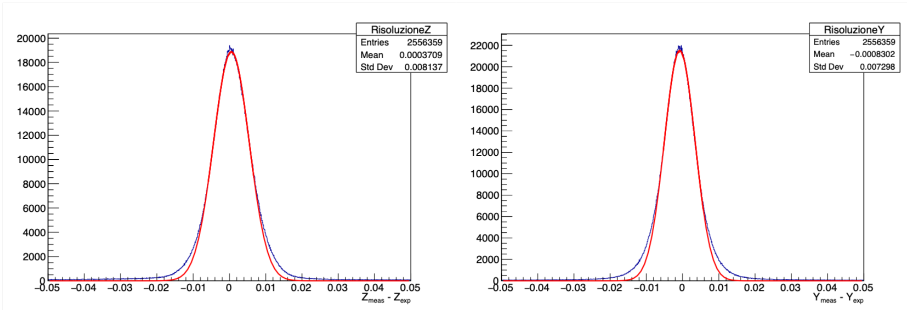

Figure 3.26: Residuals distributions of z (left) and y(right) (eq. (3.9)) of the detector NERO.

distribution of the quantity in 3.9 has a standard deviation:

$$\sigma = \sqrt{\frac{3}{2}}\sigma_x \tag{3.10}$$

The spatial resolutions on both y and z coordinates can be thus estimated by fitting the distribution of 3.9 from the measured events, and evaluating the quantity (3.10) from the fit.
In Figures 3.25 and 3.26 the obtained distributions of the residues in z and y for both ROSSO and NERO detectors are shown, together with the gaussian fit superimposed. The distributions present a good gaussian behavior, but with non-gaussian tales, as expected. Once evaluated the variance from fit results, the corresponding resolutions have been evaluated from the relation (3.10) and are listed in Table 3.3. The resulting values, compared between the two detectors are similar.

detector	z resolution (mm)	y resolution (mm)
ROSSO	4.3	3.4
NERO	4.0	3.5

Table 3.3: Resolutions on x and y views of ROSSO and NERO hodoscopes.

3.5.4 Fiducial Surface

To avoid not-physical asymmetries in the measured muon flux related to possible asymmetries of the detector efficiency, a fiducial sensitive area of the tracking planes has been defined. The goal is to reduce the discrepancy between muon fluxes coming

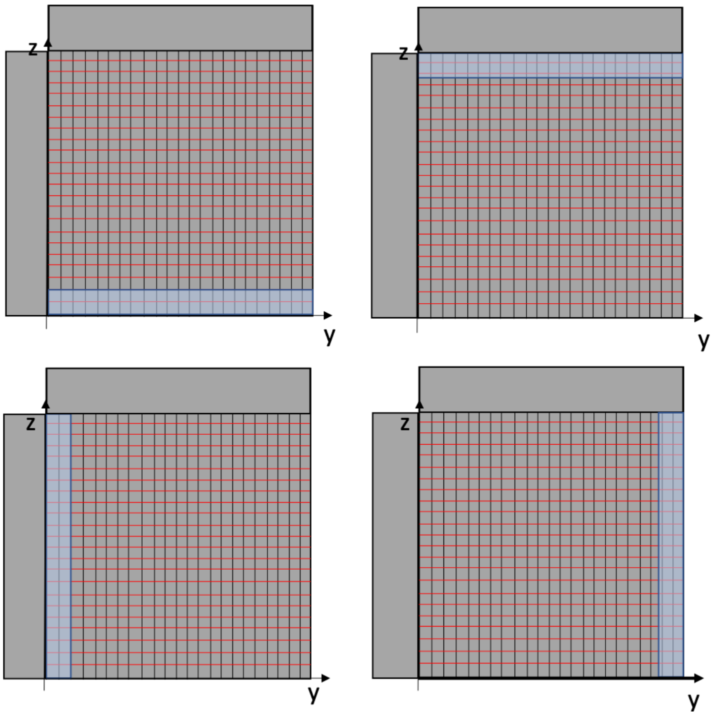

Figure 3.27: Scheme of a plane of the MURAVES hodoscopes. The regions in the blue semi-transparent windows have been progressively removed to check the consequent improvement in the *left/right* ratio.

from opposite directions. This analysis has been conducted evaluating the *left/right* flux ratio in a control angular region, chosen within the free-sky region to not be affected by the mount absorption.
Considering the free-sky flux in the angular ranges $\phi \in [170{,}190]$ deg and $\alpha \in [25{,}30]$ deg, and dividing it horizontally in the two regions $\phi \in [170{,}180]$ (left directions) and $\phi \in [180, 190]$ (right directions), the measured flux ratio $\Phi_{\mu}^{left}/\Phi_{\mu}^{right}$ results ~ 0.95. To improve this ratio toward unity, the considered sensitive area of the planes has been progressively reduced, excluding the extreme zones. The exclusion has been applied to each side of the yz plane individually; in Figure 3.27 these selections are pictorially represented. Removing a portion of the sensitive area from each side of the axis, progressively larger from 0 to 10 cm, with steps of 1 cm, the variation of $\Phi_{\mu}^{left}/\Phi_{\mu}^{right}$ has been evaluated as function of the cut. In Figure 3.28 the cases of reducing the surface from the left and right sides of the y-axis independently are shown. As it can be seen, significant improvement are obtained reducing the sensitive area from the negative side of the y-axis. The positive side reduction is not affecting the muon flux $\Phi_{\mu}^{left}/\Phi_{\mu}^{right}$ ratio. In Figure 3.29 the effect of removing the top and bottom part of the z-axis are shown. It is clear that these cuts are not effective in the improvement of the left/right flux agreement. Anyways, for symmetry, the same cut has been applied to both views. The resulting behaviors have

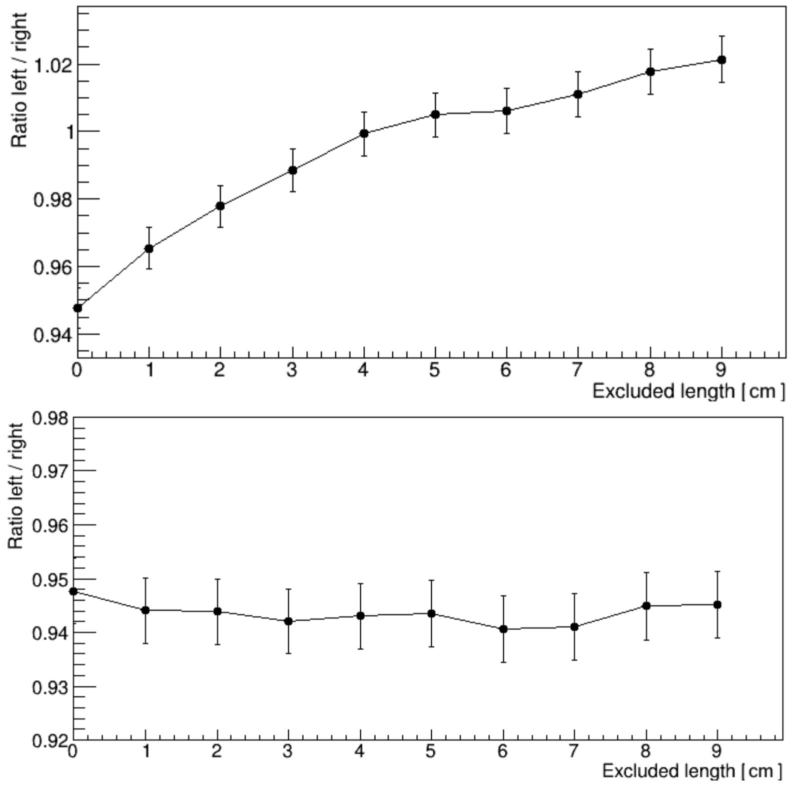

Figure 3.28: Ratio of the muon flux from the left and right directions, in function of the removed sensitive area by the right (top) and the left (bottom) sides of the y-axis.

been represented in Figure 3.30 comparing the two hodoscopes, ROSSO and NERO. The trends are vey similar, thus the same selection have been applied, at 5 cm, since a plateau region is clearly visible from 5 to 6 cm in Figure 3.30. After this reduction, the ratio $\Phi_{\mu}^{left}/\Phi_{\mu}^{right}$ is 1.007 and 1.016 for ROSSO and NERO respectively, and the single hodoscope sensitive area is ~ 0.90 m^2.

3.5.5 Track quality selection

Tracks reconstructed following the strategy described in section 3.5.2, are successively selected or rejected according to a quality criterion. The quality of the track is quantified by the degree of alignment of its clusters; thus a cut on the χ^2 has been applied. Considering the differences between datasets taken pointing to the Vesuvius and in calibration position, which include the different periods, environmental conditions and states of the system, the chosen upper limits of the ch^2 are different.
Currently, the adopted strategy is based on the assumption that the flux measured from the open sky directions overlying the volcano, must be comparable with flux measured in calibration mode, from the corresponding directions. Thus, a control region $\Delta\phi$, $\Delta\theta$ have been decided where the following condition is

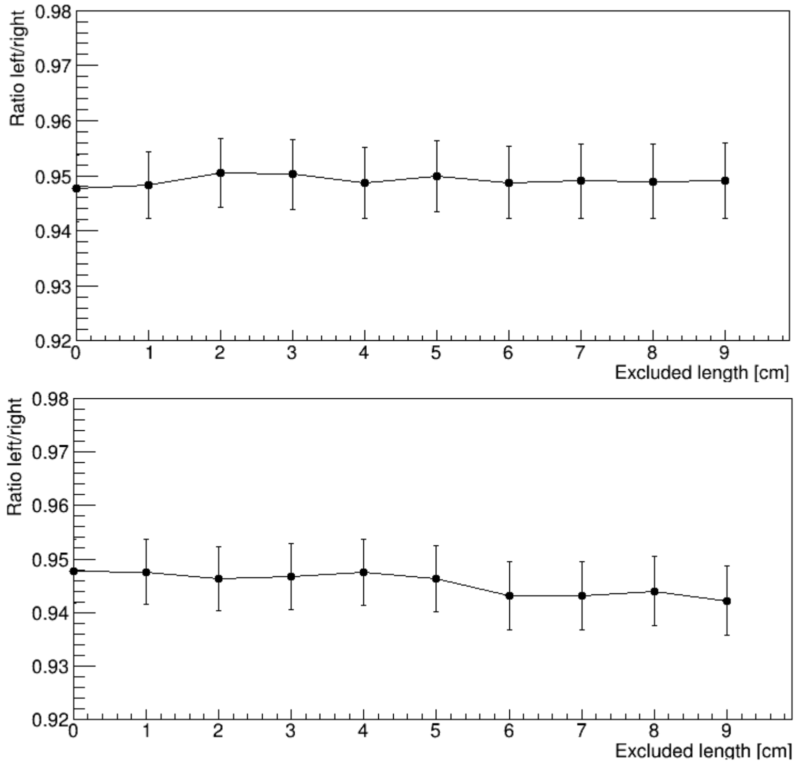

Figure 3.29: Ratio of the muon flux from the left and right directions, in function of the removed sensitive area by the right (top) and the left (bottom) sides of the z-axis.

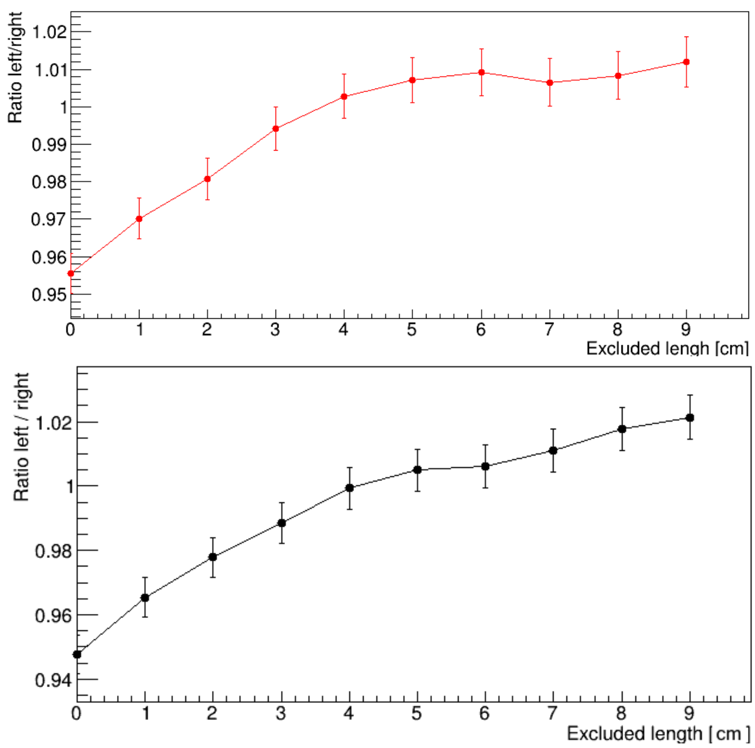

Figure 3.30: Comparison between ROSSO (top) and NERO (bottom) *left/right* asymmetry behaviors.

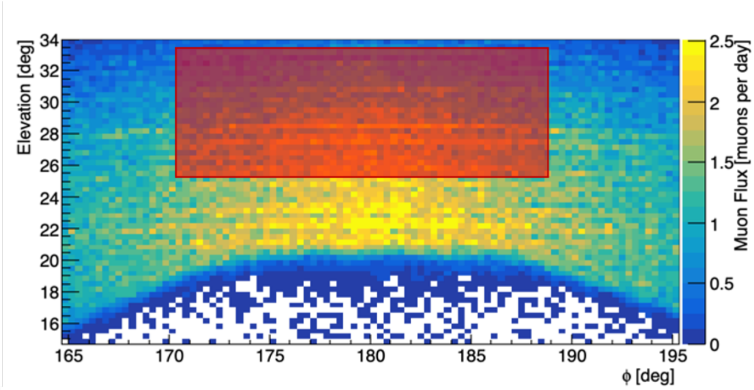

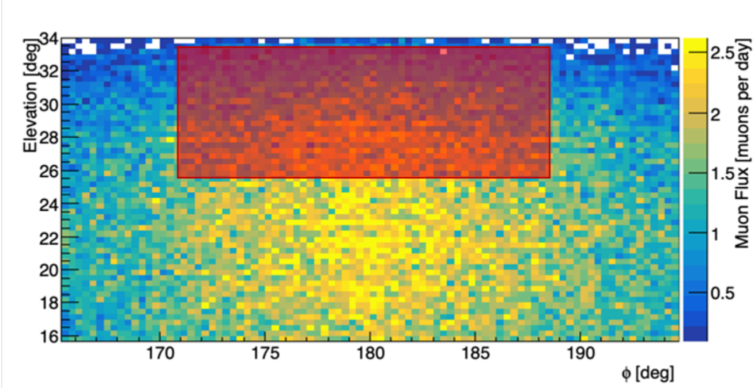

Figure 3.31: Free-Sky control region highlighted on both the flux distributions measured from the Vesuvius (top) and Calibration (bottom) datasets.

expected to be satisfied:

$$\frac{\Phi_{\mu}^{Ves}(\Delta\phi, \Delta\theta)}{\Phi_{\mu}^{Calib}(\Delta\phi, \Delta\theta)} = 1 \tag{3.11}$$

The control region is highlighted in Figure 3.31. It has been chosen enough distant from the Vesuvius contour to avoid systematics due to scattering or absorption through the highest part of the volcano.

The cuts to be applied to the χ^2 of the Vesuvius dataset and the Calibration dataset are decided on the base of the condition in 3.11. Different values are considered as maximum of χ^2, and the ratio $\frac{\Phi_{\mu}^{Ves}(\Delta\phi,\Delta\theta)}{\Phi_{\mu}^{Calib}(\Delta\phi,\Delta\theta)}$ is evaluated respect to different selection on both Vesuvius and Calibration datasets. In Figure 3.32 the flux ratio in the control region is represented as a function of the maximum χ^2 applied on the Vesuvius data. Different curves correspond to different maximum χ^2 applied to Calibration data. The doublets $(\chi^2_{Ves}, \chi^2_{Calib})$ fullfilling the condition in (3.11) are obtained, and a function $\chi^2_{Calib}(\chi^2_{Ves})$ is evaluated applying a polynomial fit. Figure 3.33 represents the estimated points $(\chi^2_{Ves}, \chi^2_{Calib})$ and the best fit curve. The obtained function of the χ^2 maximum values is used to evaluate the best selection to be applied to the data. The transmission, corresponding to an angular region where the Vesuvius is framed, is evaluated

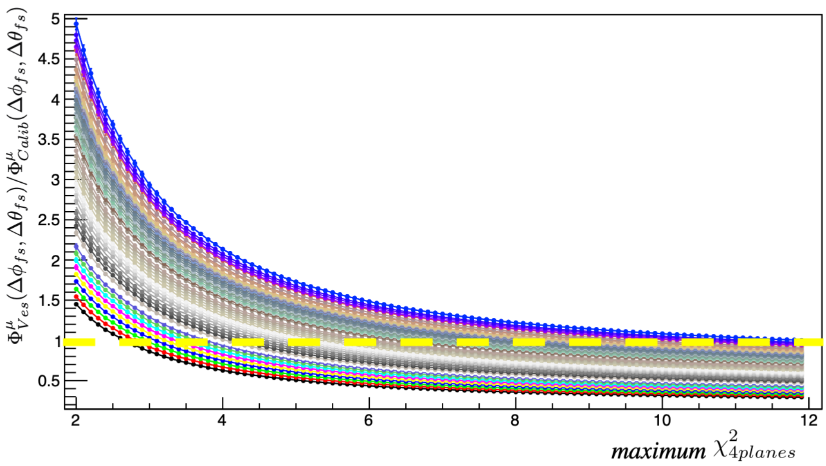

Figure 3.32: Ratio $\frac{\Phi^{Ves}_{\mu}(\Delta\phi,\Delta\theta)}{\Phi^{Calib}_{\mu}(\Delta\phi,\Delta\theta)}$ in the control region is represented as a function of the maximum χ^2 applied on the Vesuvius data. Different curves correspond to different maximum χ^2 applied to Calibration data.

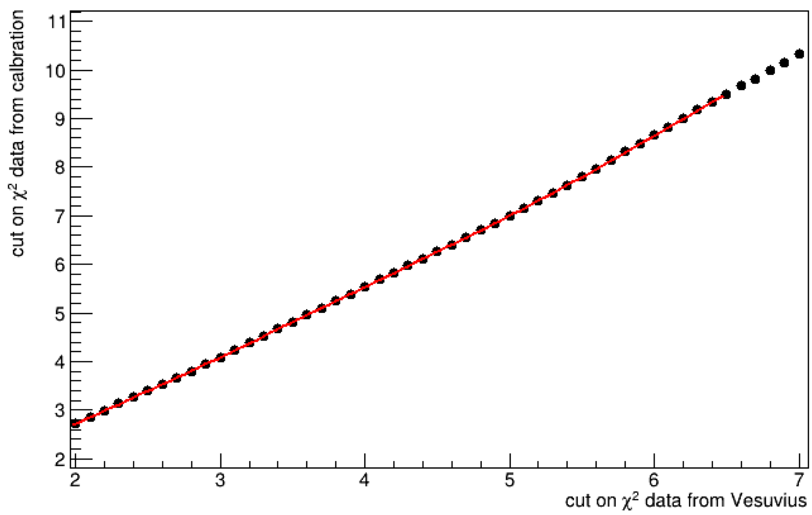

Figure 3.33: Evaluated (χ^2_{Ves}, χ^2_{Calib}) and the best fit function $\chi^2 Calib(\chi^2_{Ves})$.

varying the χ^2 selection, based on the resulting function in Figure 3.33. Figure 3.34 shows an example of the transmission as a function of the applied selection. Two different working points have been investigated. As it can be seen a flatter region is evident for both the working points, and it is the region where it is more convenient to set the maximum χ^2 value. The decision to apply the selection in correspondence of the *plateau* is also supported by the greater agreement between the two working points. Details about the specific cuts applied on the data are given in the *Results* section.

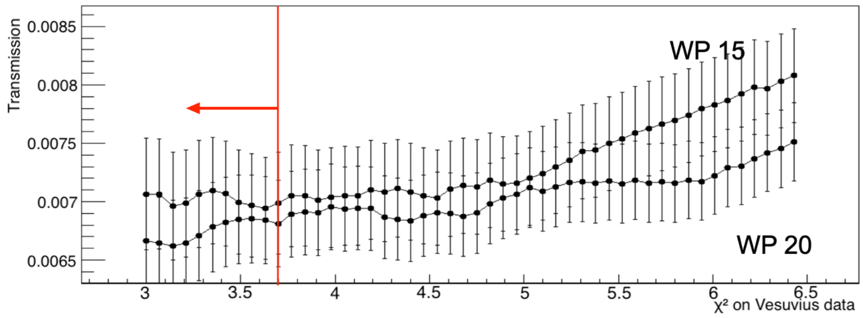

Figure 3.34: Measured transmission as a function of the χ^2 selection, in an angular region involving the volcano. Two different working points are represented, 15°C and 20°C. A plateau region is clearly distinguishable, and corresponds to also a greater level of agreement between the two working points, suggesting to chose the selection parameters around that zone.

3.6 Models and Simulations

The role of simulations and models in a muon radiography experiment is crucial to accomplish the purpose of the specific application. It is both needed to the preliminary feasibility studies and to perform the goal measurement itself.
The MURAVES experiment is based on a simulation chain from the transport through rock to the detector perrformancies. This engine is currently being developed and more and more details are being added.

3.6.1 The Vesuvius' structure

The muon transport through the volcano needs the amount of rock to be crossed by muons from each different direction to be precisely known. The profile of the volcano can be evaluated by making the use of a DEM (Digital Elevation Model) of the area around the volcano [46]. Currently the used DEM has a resolution of 5 m on x and y coordinates and 1 m on the quote. It has been furnished by the INGV (Istituto Nazionale di Geofisica e Vulcanologia) and is represented in Figure 3.35.
The Vesuvius' thickness map in the $\phi - \alpha$ plane, from the detector point of view, can be obtained by providing the DTM to an algorithm which assess the best stepping to easily obtain the rock thickness from the required direction. The used algorithm

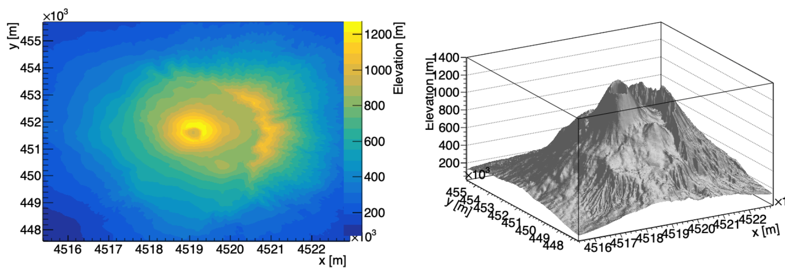

Figure 3.35: DEM of the surrounding area of the Vesuvius. Left: bidimensional histogram of the elevations. Right: 3D representation of the DEM. Both figures have been realized with the ROOT framework [47].

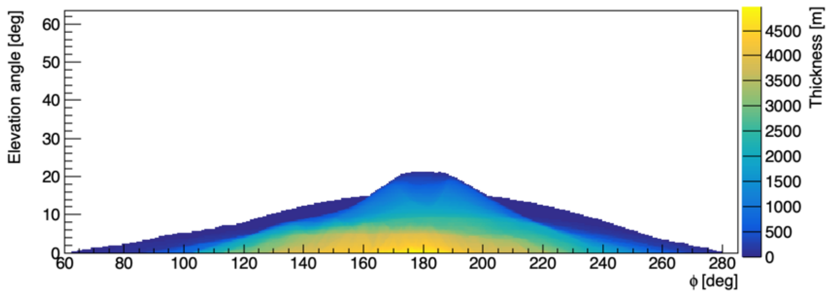

Figure 3.36: Vesuvius' thickness map, realized by the use of TURTLE [48].

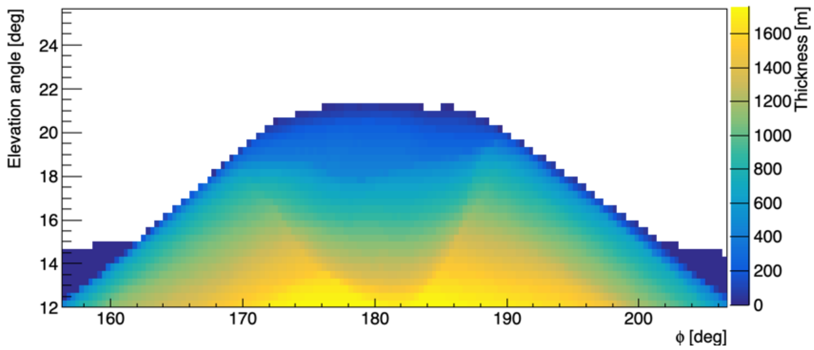

Figure 3.37: Thicknesses of Vesuvius in the summithal region.

is implemented in a tool called TURTLE, described in [48]. The resulting profile of the Vesuvius is represented in Figure 3.36 and has a binning of 1/3 degrees × 1/3 degrees deg. The base of the volcano is characterized by very prohibitive thicknesses ranging from 3 to 5 km in the central region. The dark blue halo is related to the remnant Mt. Somma, the ancient caldera from which the actual crater raised. The MURAVES experiment is realistically interested to the summital part of the cone, where the thicknesses are still high and challenging, but at least approachable (see also Section 3.4). The cone summit thicknesses are reported in Figure 3.37.

3.6.2 Muon transport through rock

Given the Vesuvius thickness map, the transport of muons through it from each direction is simulated with a backward Monte Carlo engine, implemented in the PUMAS library [49]. This library, wrote in C99, is intended to use backward Monte Carlo to exclusive sample a final state by reversing the simulation flow, significantly reducing the spent time. Authors developed the tool particularly for muon radiography applications, but it is friendly to other muon experiments. The cosmic muon flux is evaluated using the modified Gaisser's formula in eq. (1.8).
Since muon absorption depends on the opacity, the average density value can be set by the user in the simulation. In Figure

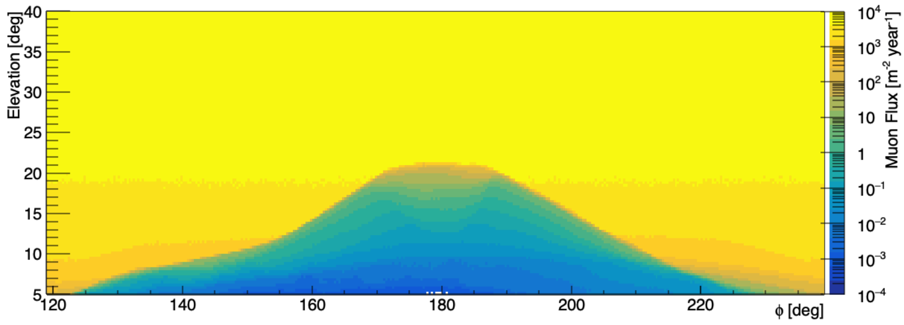

Figure 3.38: Expected muon flux through the Vesuvius body, impacting a vertical plane. The hypothesized density is ρ = 2.65 g/cm^3; the results is obtained with PUMAS library [49].

3.38 the muon flux expected to escape the Vesuvius is represented, without accounting the detector efficiencies. The simulation result shows that, if a density of 2.65 g/ cm^3 is hypothesized, from the summithal part the rate of muons is in the range from 1 to tens particles per year in angular bins of $1/3 \times 1/3$ degrees.

3.6.3 Detector simulation

To provide the correct muon flux expected to be measured in the experiment, the effect of the detector itself must be accounted. In particular, the geometrical factor $g(\Omega)$ and the energy cut E_{min}^{det} have been evaluated.

Geometrical factor

As explained in section 1.1.3, the measured muon flux depends on the effective surface $S_{eff}(\theta, \phi) = g(\theta, \phi) \cdot S$. Considering $S = 1$ m ^{2} the sensitive area of a plane, $g(\theta, \phi)$ represents the fraction of S that is really effective in the possible detection of a muon coming with the direction (θ, ϕ). This fraction is related to the disposition of the planes. A schematic representation can be found in Figure 3.39. The effective area S_{eff} can be analytically evaluated as follows. Considering muons coming from the first to the fourth plane, S_{eff} is obtained as:

$$S_{eff} = L_x \times L_y \tag{3.12}$$

where L_x,

$$L_x = \begin{cases} \ell - \Delta z_{1,4} + \frac{L_{14}}{|\cos\phi|} \tan\alpha & \text{if } \alpha < \arctan\frac{\Delta z_{14}|\cos\phi|}{L_{1,4}} \\ \ell + \Delta z_{1,4} - \frac{L_{1,4}}{|\cos\phi|} \tan\alpha & \text{otherwise} \end{cases}$$

and L_y,

$$L_y = \ell - L_{1,4} \tan\phi \tag{3.13}$$

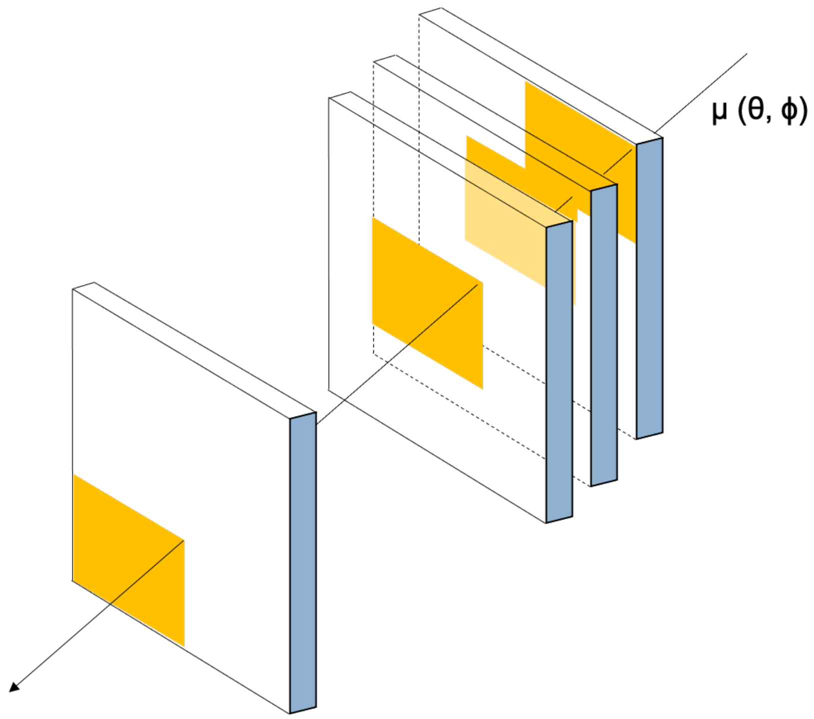

Figure 3.39: Schematic representation of the effective sensitive surface $S_{eff}(\theta,\phi)$ of the MURAVES hodoscope.

are the sides of S_{eff} parallel to the x- and y- axes respectively. The quantity $\ell = 1$m is the side lenght of the planes, $\Delta z_{1,4} = 0.30$ m is the height difference from the floor between the first and the fourth planes, $L_{1,4} = 1.72$ m is the distance between the same planes, and $\alpha = 90 - \theta$ is the elevation angle. The maximum observable elevation in this configuration is:

$$\alpha_{max} = \frac{\ell + \Delta z_1}{L_{1,4}} \sim 37 \text{ degrees} \tag{3.14}$$

for directions horizontally orthogonal to the plane. A scheme of the geometrical projections of the detector acceptance is represented in Figure 3.40. Similarly, to evaluate $g(\theta,\phi)$ in the case in which only the first three planes are considered, as in the trigger logic, it is sufficient to replace $L_{1,4}$ with $L_{1,3} = 0.51$ m and $\Delta z_{1,4}$ with $\Delta z_{1,3} = 0.10$ m.
Similar formulas can be also obtained to describe S_{eff} for muons coming from the back, *i.e.* from the fourth to the first plane.
The distribution of the geometrical factors $g(\theta,\phi) = \frac{S_{eff}(\theta,\phi)}{S}$, evaluated in the two different cases, considering or not the fourth plane, are represented in Figure 3.41 in the plane α, ϕ. To validate the analytical evaluation, a toy Monte Carlo simulation have been developed to synthesize the geometrical factors and compatible results have been obtained.

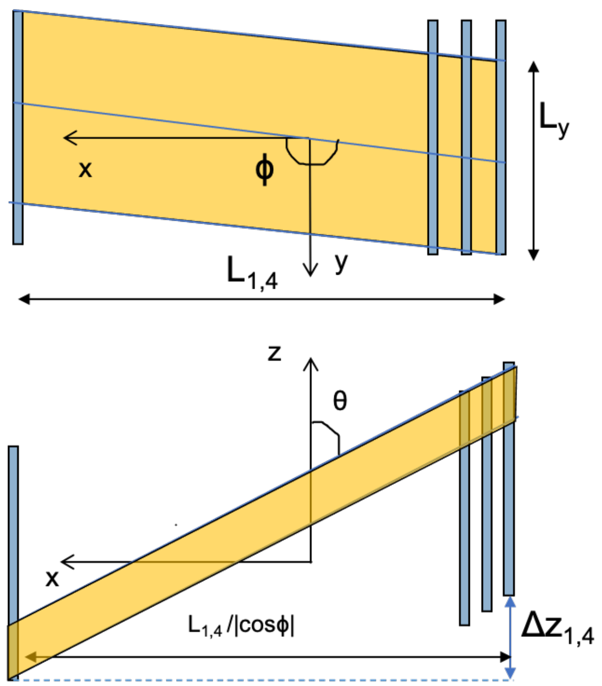

Figure 3.40: Projected schemes of the S_{eff} (θ,ϕ) of the MURAVES hodoscope, considering all planes in the geometry.

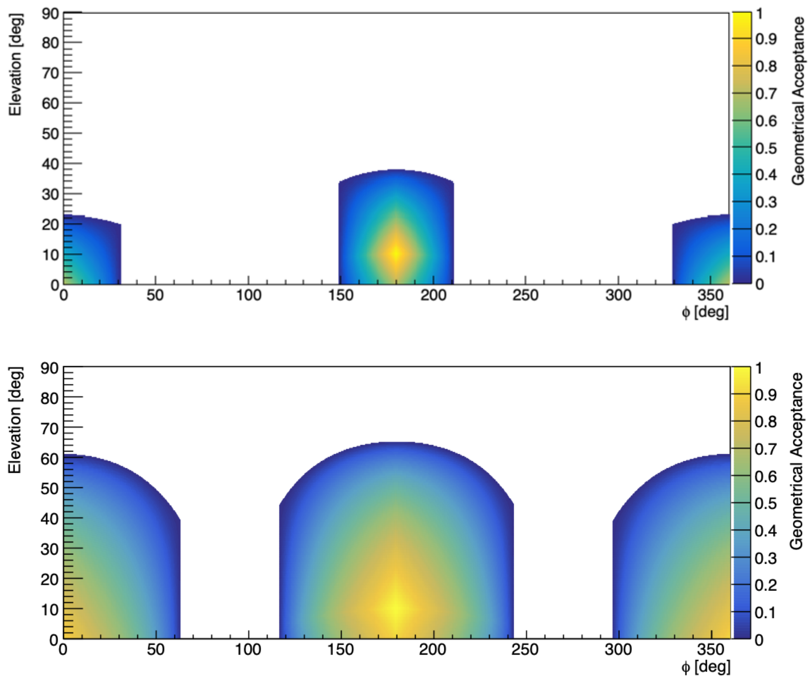

Figure 3.41: Geometrical acceptance of the hodoscope, considering four (top) and three (bottom) scintillator planes.

Detector energy cut

A muon, to be detected, has to cross all planes of the muon tracker; thus the energy needed to cross the detector without beeing absorbed in its material has to be accounted. A detailed evaluation of this energy has been performed following the stopping power values, listed in [6]. The materials to be considered are the aluminum shields of the planes, the plastic scintillator polistirene and the lead interposed between the last two planes. The energy thresholds, in the case when only three planes of the hodoscopes are considered and the case when all the tracking planes and the lead wall are taken into account, are represented as a function of the particle direction, in Figure 3.42. A muon

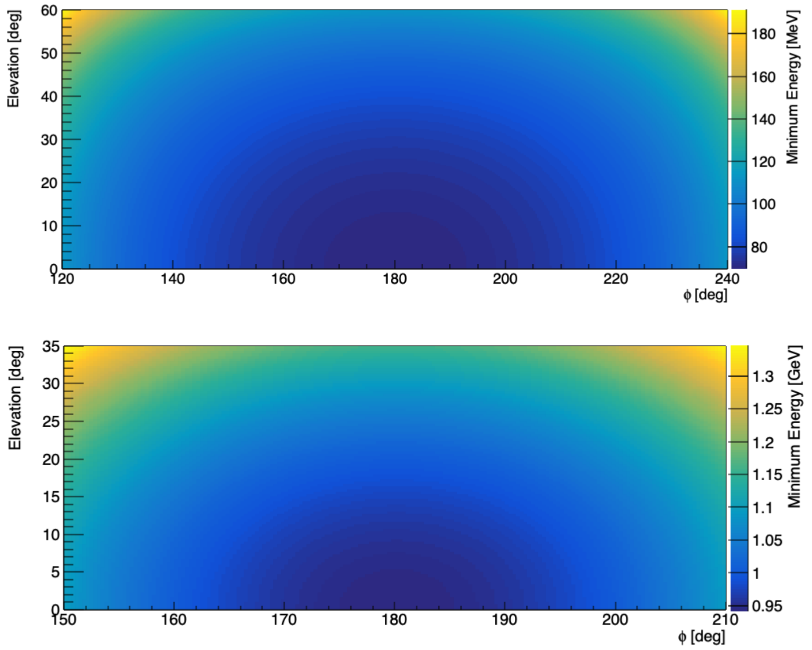

Figure 3.42: Minimum energy a muon needs to cross the first three planes of hodoscope (top) and the full hodoscope including the lead wall (bottom).

impacting the detector coming orthogonally respect to the planes, needs ~ 70 MeV to cross the first three tracking stations and ~ 940 MeV to survive the full hodoscope, lead included. In Figure 3.43 the minimum energy in the two cases, is represented in function of the elevation, for a muon coming from a direction that is horizontally orthogonal to the y-axis of the detector.

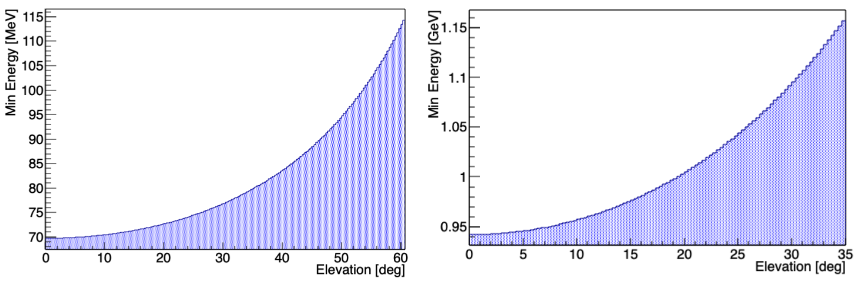

Figure 3.43: Minimum energy for a muon impacting at $\phi = 180$ deg in function of the elevation, to cross three scintillator planes, and the full hodoscope (lead included).

3.7 Results

The final purpose of the MURAVES experiment is to reach a density distribution measurement of the Vesuvius' Great Cone.

This purpose is highly challenging, due to the very low muon rates, long data-taking exposures and consequent issues of the detector functioning, already mentioned in section 3.5.1.
Currently, the data analysis results are separated respect to the muon tracker and the working point. A substantial statistics is available from ROSSO and NERO, while calibration data from the BLU detector is not yet available; therefore its data cannot be used to complete the data analysis.
Four dataset are used separately: two from ROSSO and two from NERO, taken in the two working points at 15°C and 20° C.
As already mentioned in Chapter 1, the density is usually evaluated from the muon transmission. The transmission is obtained dividing the muon flux measured from the Vesuvius by the flux measured from the open sky. The two fluxes are measured during separated data acquisitions, with the detector inversely oriented. Figure 3.44 pictorially shows the difference between the *Vesuvius data-taking* and *open-sky data-taking*.

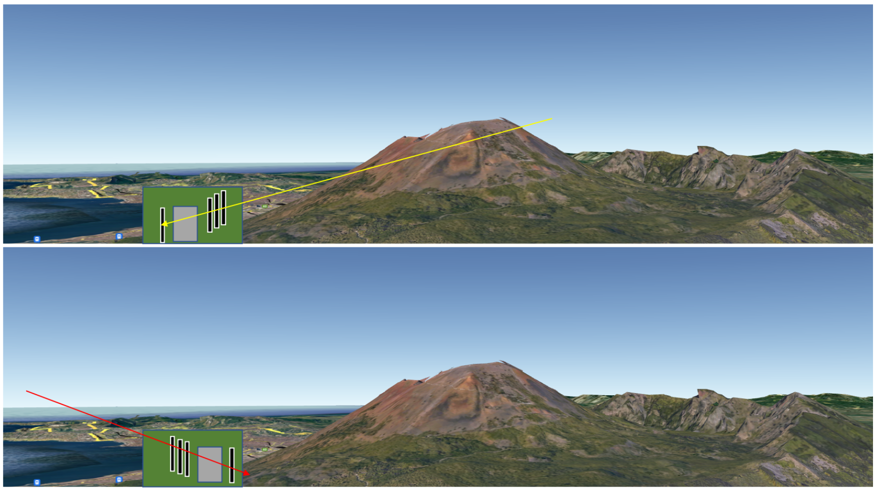

Figure 3.44: Pictorically representation of the detector orientation in Vesuvius data-taking (top) and open-sky data taking (bottom).

Vesuvius Datasets

The four datasets from the Vesuvius correspond to different active acquisition times, listed in Table 3.4. Events of the four datasets

Dataset	Time
ROSSO wp 15°C	51 days
ROSSO wp 20° C	40 days
NERO wp 15°C	43 days
NERO wp 20°C	26 days

Table 3.4: Corresponding times of the four datasets.

have been selected following the description in section 3.5; the χ^2 maximum value is 3.7 for all dataset. The bidimensional maps

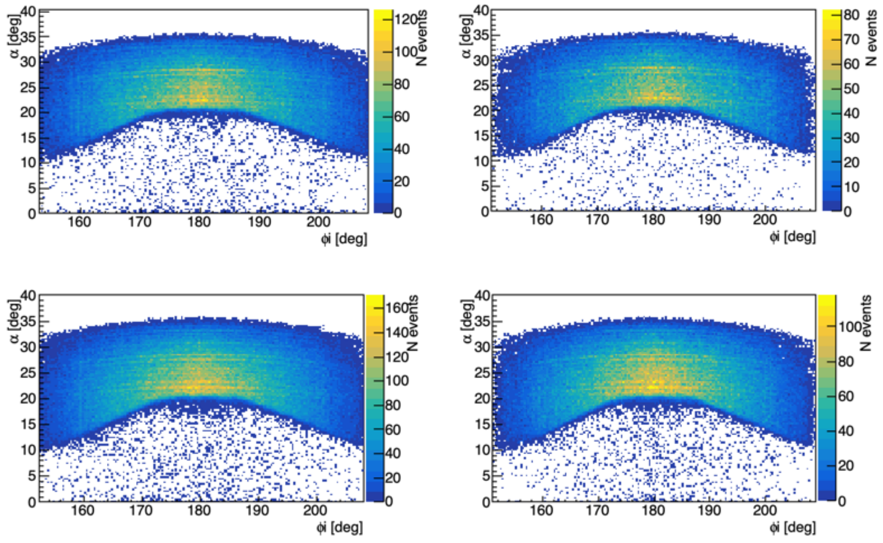

Figure 3.45: Bidimensional histograms of the number of selected events of the Vesuvius datasets. Top: NERO, working point 15°C (left); NERO, working point 20°C (right). Bottom: ROSSO, working point 15°C (left); ROSSO, working point 20°C (right). The binning is $1/3 \times 1/3$ degrees.

of the number of selected events in the plane $\phi - \alpha$ where ϕ is the horizontal angle and α is the elevation angle respect to the horizontal are represented in Figure 3.45.

Calibration Datasets

The calibration datasets correspond to less time respect to the Vesuvius datasets. However, the statistical uncertainty is negligible respect to the Vesuvius case. The duration of the open-sky acquisitions are listed in Table 3.5. The calibration events have

Dataset	Time
ROSSO wp 15°C	9.5 days
ROSSO wp 20° C	14.3 days
NERO wp 15°C	10 days
NERO wp 20°C	17 days

Table 3.5: Corresponding times of the four datasets.

been selected in function of the Vesuvius selection, as explained in section 3.5.5. The χ^2 maximum values are listed in Table 3.6. Figure 3.46 represents events distributions, after the χ^2 cut, as bidimensional maps, in $\phi - \alpha$ plane, of the calibration data.

Dataset	maximum χ^2
ROSSO wp 15°C	5
ROSSO wp 20° C	4.4
NERO wp 15°C	5.1
NERO wp 20°C	5.1

Table 3.6: Corresponding times of the four datasets.

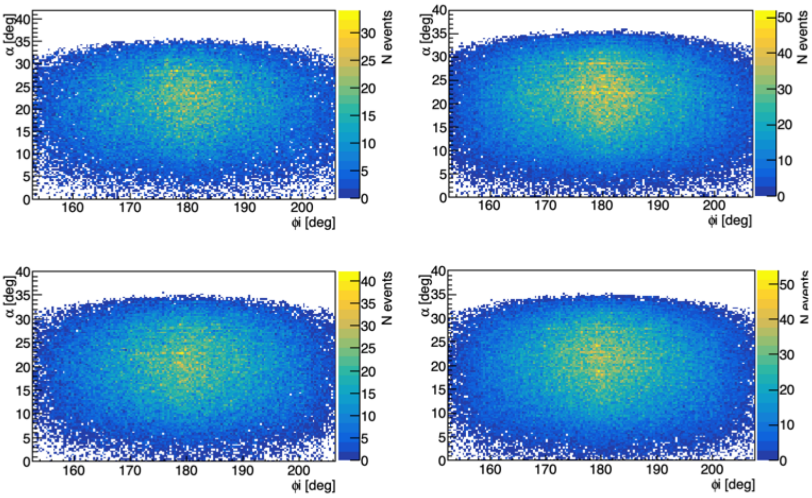

Figure 3.46: Bidimensional histograms of the number of selected events of the Calibration datasets. Top: NERO, working point 15°C (left); NERO, working point 20°C (right). Bottom: ROSSO, working point 15°C (left); ROSSO, working point 20°C (right). The binning is $1/3 \times 1/3$ degrees.

3.7.1 Density evaluation

The density evaluation strategy adopted at this stage of the experiment is described in the following.
The procedure needs both measured and simulated data; measured data consist in two fluxes of muons, one observed from the Vesuvius and the other from the open sky. The measured fluxes can be expressed as:

$$\Phi^{Ves}_{meas}(\phi,\alpha) = S_{eff}(\phi,\alpha)\cdot\epsilon_{Det}(\phi,\alpha)\cdot\epsilon_{tr}\cdot\epsilon^{Ves}_{\chi^2}\cdot\Phi^{Ves}_{real}(\phi,\alpha)+\delta\Phi^{Ves}_{noise} \tag{3.15}$$

$$\Phi^{os}_{meas}(\phi,\alpha) = S_{eff}(\phi,\alpha)\cdot\epsilon_{Det}(\phi,\alpha)\cdot\epsilon_{tr}\cdot\epsilon^{os}_{\chi^2}\cdot\Phi^{os}_{real}(\phi,\alpha)+\delta\Phi^{os}_{noise} \tag{3.16}$$

In the above equations, measured fluxes depend on the effective surface S_{eff}, the detector and trigger efficiencies, ϵ_{Det} and ϵ_{tr} respectively, and a selection efficiency ϵ_{χ^2} related to the cut applied in the analysis on the χ^2 parameter. The effective surface and the detector efficiency are expected to be equal in Φ^{Ves}_{meas} and Φ^{Calib}_{meas}, even if some higher order corrections could apply, due to the necessary handling of the tracker planes when the orientation is inverted from Vesuvius to Calibration, and small changes of efficiencies could occur due to long exposure of the apparatus and due to the different datasets. The trigger rate efficiencies can also be considered comparable, since the trigger rates are measured of the same order of magnitude in both the data acquisitions. The analysis efficiency ϵ_{χ^2}, in principle, cannot be considered equal for Vesuvius and Calibration data, due to the different distributions of muon energy. In fact, muons who traversed the mountain before reaching the detector are expected

to have lower energy respect to muons coming from open sky. This is reflected in the effect of the lead wall which deflects low energy muons more than high energy ones. These efficiencies cannot be assessed on the basis of measured data alone, but must be estimated through detailed and realistic simulations of the apparatus and of the expected fluxes. Currently the simulation is not jet detailed enough to fournish the correct efficiencies.
The terms $\delta\Phi^{Ves}_{noise}$ and $\delta\Phi^{os}_{noise}$ in the above expressions (3.15) and (3.16) are the hypothetical remaining contributions of noise and backgrounds; if those contributions are considered negligible, the measured transmission would be:

$$T_{meas}(\phi, \alpha) = \frac{\epsilon^{Ves}_{\chi^2}}{\epsilon^{Calib}_{\chi^2}} T_{real}(\phi, \alpha) \tag{3.17}$$

with the only dependance on the ratio $\frac{\epsilon^{Ves}_{\chi^2}}{\epsilon^{Calib}_{\chi^2}}$.
The measured transmission should be compared with the expected transmission as a function of the hypothesized density. The quantity $T_{real}(\phi, \alpha)$ can be simulated through the muon transport tool described in sec 3.7.2. However, the lack of information about the term $\frac{\epsilon^{Ves}_{\chi^2}}{\epsilon^{Calib}_{\chi^2}}$ suggests to try a data-driven approach. Based on volcanological knowledge, a density hypothesis is made in a region of the volcano: an average density ρ_0 is assumed in the region $\Delta\phi_0, \Delta\alpha_0$. From this hypotesis the unknown paramenter can be *estimated* from data:

$$C = \frac{\epsilon^{Ves}_{\chi^2}}{\epsilon^{Calib}_{\chi^2}} \approx \frac{T_{PUMAS}(\Delta\phi_0, \Delta\alpha_0; \rho_0)}{T_{meas}(\Delta\phi_0, \Delta\alpha_0)}. \tag{3.18}$$

The estimated parameter C can be used to correct the generic transmission $T_{meas}(\phi, \alpha)$. The corrected transmission $T'_{meas}(\phi, \alpha)$, can thus be used to evaluate the density.
The lack of statistics makes it necessary to enlarge the angluar regions where to measure an average density. In this work of thesis, six angular regions have been chosen, highlighted in Figure 3.47. The regions have been chosen large enough to reach a statistical uncertainty around and not much higher than 10%. The ϕ and α limits of the regions have been set to focus on the investigation of the expected stratified structure, *i.e.* the presence of horizontal layers of different densities, expected on the basis of volcanological studies, and on the possible density asymmetry between the left and right sides of the Vesuvius.

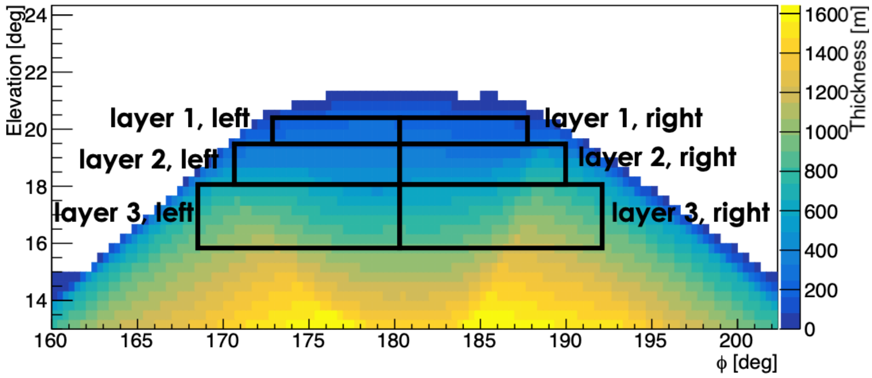

Figure 3.47: Angular regions where the average density has been evaluated.

The number of events and the statistical uncertainties in each of the chosen regions are listed in Table 3.7.

	N events		Stat. unc. (%)	
Dataset	left	right	left	right
	Layer 1			
ROSSO wp 15°C	428	439	0.05	0.05
ROSSO wp 20°C	346	323	0.05	0.05
NERO wp 15°C	231	258	0.05	0.05
NERO wp 20°C	128	258	0.07	0.06
	Layer 2			
ROSSO wp 15°C	164	140	0.08	0.08
ROSSO wp 20°C	106	109	0.10	0.10
NERO wp 15°C	78	79	0.11	0.11
NERO wp 20°C	61	63	0.13	0.13
	Layer 3			
ROSSO wp 15°C	61	76	0.12	0.11
ROSSO wp 20°C	58	63	0.13	0.13
NERO wp 15°C	47	47	0.14	0.15
NERO wp 20°C	27	30	0.19	0.18

Table 3.7: Events and statistical uncertainties of the four datasets in the six regions.

Density evaluation: procedure

The strategy developed to evaluate an average density in an angular region is described in the following. The procedure starts by simulating the expected transmission varying the overall density value. A function $T_{\Delta\phi,\Delta\alpha}(\rho)$ is then derived from the distribution of the expected transmission as a function of density. An example is shown in Figure 3.48. The inverted function $\rho_{\Delta\phi,\Delta\alpha}(T)$ is used to corresponds a density value to the measured transmission. The measured, and then corrected, transmission $T'(\Delta\phi, \Delta\alpha)$ is affected by its uncertainty, $\sigma_{T'}$. Two limit densities can be evaluated

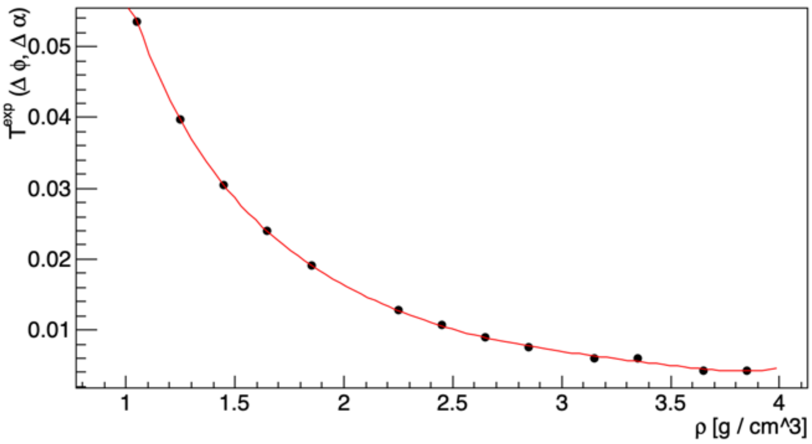

Figure 3.48: An example of the function $T_{\Delta\phi,\Delta\alpha}(\rho)$ derived fitting the scatter plot of the transmission, resulting from simulations of different density hypotheses. The simulations have been performed with PUMAS changing the density parameter.

corresponding to the 1 σ fluctuations of the transmission; the upper limit ρ^{up} is evaluated as $\rho^{up}_{\Delta\phi,\Delta\alpha} = \rho_{\Delta\phi,\Delta\alpha}(T'_{meas} - \sigma_{T'})$ while the lower limit $\rho^{low}_{\Delta\phi,\Delta\alpha} = \rho_{\Delta\phi,\Delta\alpha}(T'_{meas} - \sigma_{T'})$. This procedure has been applied to each of the chosen angular regions.

Density evaluation: results

Following the indications of volcanologists, a density hypothesis has been made in the region indicated as *layer 1, left*. The assumed density is 2.65 g / cm^3, corresponding to the *Standard Rock*. The resulting densities, evaluated following the procedure explained above for each dataset and in each chosen region, are shown in Figure 3.49. The plots present also the average density resulting from the combination of the four measurements, with 1 and 2 σ colored bands. As it can be seen in Figure 3.49, the densities resulting from the different datasets are not always in good agreement; in some cases the disagreement overcomes 2σ. The observed disagreement suggests the existence of sources of systematic error, which depend on the particular dataset, that is, on the particular detector and on the specific working conditions. These considerations led to the decision to measure the relative density between the two regions of the same layer. The ratio ρ_{right}/ρ_{left} is thus evaluated for each layer and each of the four datasets. Results are reported in Table 3.8 and in Figure 3.50. The average line and 1-2 σ bands are shown as well. Plots in Figure 3.50 clearly show a reduction of the disagreement between the various datasets, confirming that the density disagreements, observable in Figure 3.49, derive particularly from systematic effects related to the detector and the working point. The discrepancies of the relative densities between the different datasets remain within 1 σ. These results show a discrepancy

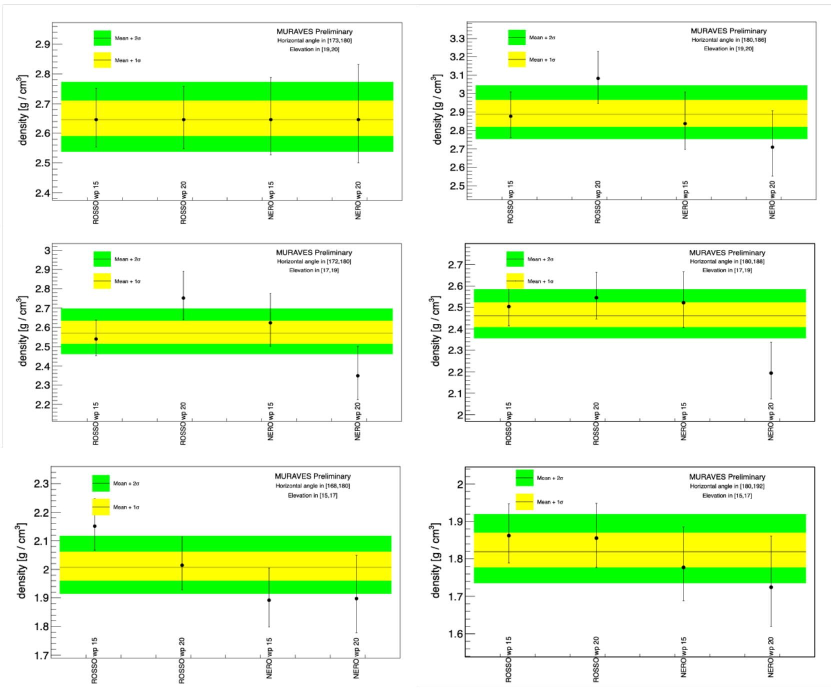

Figure 3.49: Densities measured in the six chosen angular regions following the method described in the text. A density of 2.64 g/cm^3 is hypothesized in the region $\phi \in$ [173,180] degrees $\alpha \in$ [19,20] degrees. Only statistical uncertainties have been accounted.

Table 3.8: Right/left asymmetries and average of the four datasets.

	ROSSO wp 15°C	ROSSO wp 20°C	NERO wp 15°C	NERO wp 20°C	Average
Layer 1	$1.08^{+0.11}_{-0.09}$	$1.16^{+0.12}_{-0.10}$	$1.07^{+0.14}_{-0.11}$	$1.02^{+0.17}_{-0.13}$	$1.09^{+0.06}_{-0.05}$
Layer 2	$0.99^{+0.09}_{-0.08}$	$0.92^{+0.11}_{-0.09}$	$0.96^{+0.13}_{-0.10}$	$0.93^{+0.14}_{-0.11}$	$0.96^{+0.06}_{-0.05}$
Layer 3	$0.87^{+0.09}_{-0.08}$	$0.92^{+0.09}_{-0.08}$	$0.94^{+0.11}_{-0.09}$	$0.91^{+0.11}_{-0.14}$	$0.90^{+0.04}_{-0.05}$

respect to 1 of the density ratio ρ_{right}/ρ_{left} in the uppermost layer, indicating an higher density on the right side. However, the significance level of this discrepancy is 1.5 σ, that is still too low to be interpreted as a density asymmetry. The same goes for the deeper layers; discrepancies between the two sides are observed, but opposite respect to the first layer, with significance levels of 0.67 and 2 σ in layer 2 and 3 respectively.
Compatible results emerge if the hypothesized density value or the region chosen as reference are changed. Furthermore, if the measured transmission is used without any hypothesized, and thus any corrections, the results in terms of right/left density ratios still agree with those already showed. Figure 3.51 reports the density ratios ρ_{right}/ρ_{left} obtained without any assumption on the density.

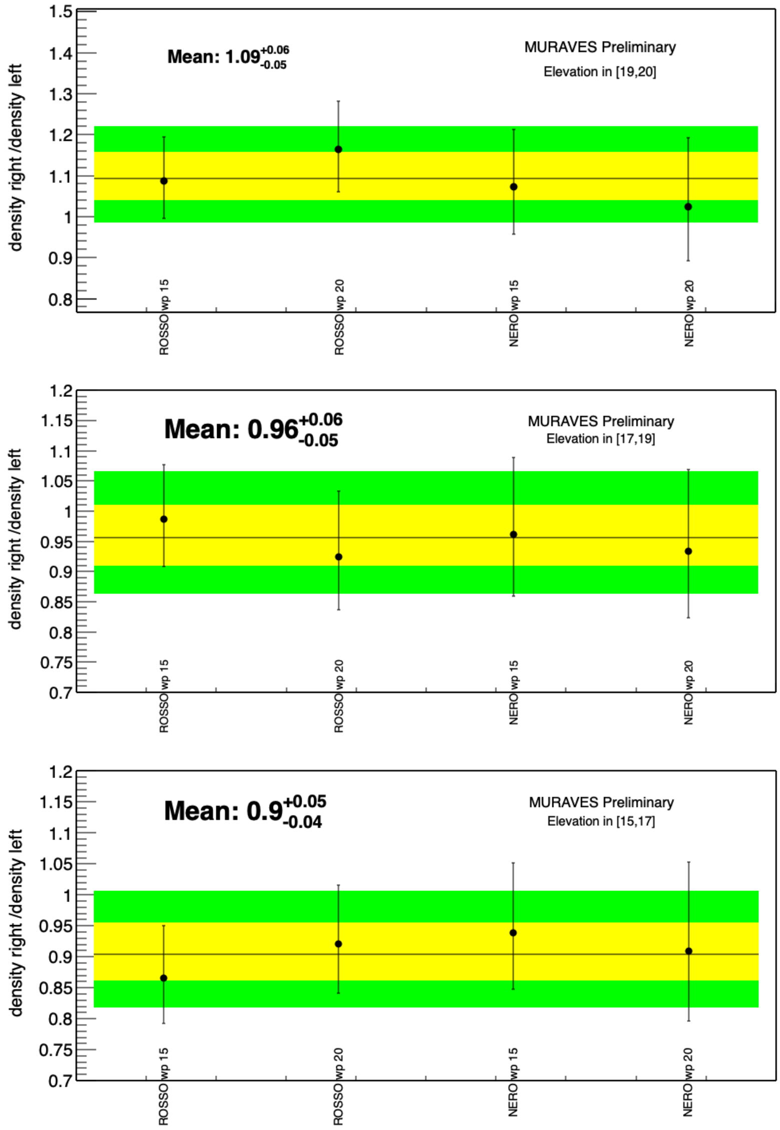

Figure 3.50: Right/left asymmetries. From top to bottom: Layer 1, Layer 2, Layer 3.

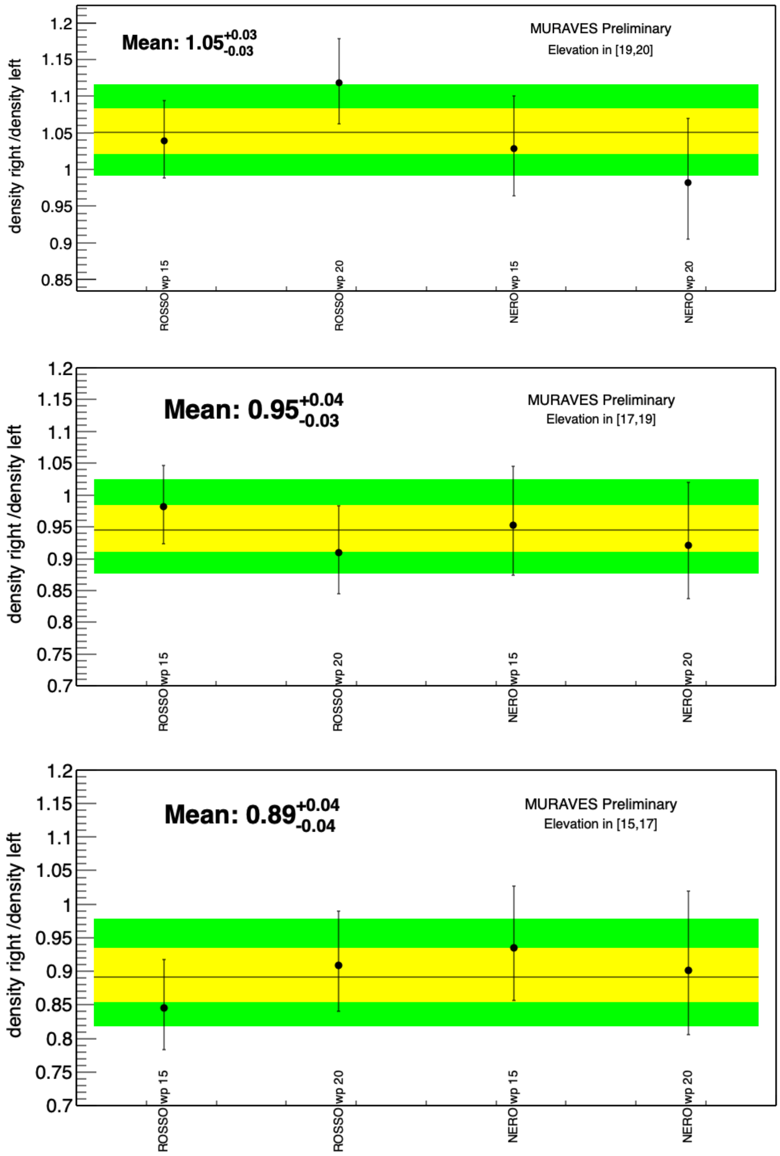

Figure 3.51: Right/left asimmetries without any hypothesis. From top to bottom: Layer 1, Layer 2, Layer 3.

3.8 Discussion and future plans

MURAVES is a highly challenging experiment due to different aspects: high amount and heterogeneous data have to be managed, since data are acquired with three independent muon trackers and in different environmental and working condintion for long acquisition times. It is necessary to control the proper functioning of the devices during very long exposure times; highly accurate and detailed simulations have to be provided, and highly precise measurements have to be achieved to reach the goal of the experiment, given the high impact of possible background contaminations on a density assessment.
This work of thesis represent the beginning phase of the data acquisition and analysis. It is devoted to a first approach to the understanding of the data and to the realization of the base analysis and simulation strategies. A well organized and easily accessible data structure has been implemented, and a complete analysis strategy, comprehending the full data processing, from the acquisition to the density assessment, has been developed. Much more work is ongoing or scheduled for the early future. The data acquisition is still running, and will include the complete telescope. The data analysis will be improved and tested on new data. New simulation strategies are under test and more details are being included.
Several investigations are planned to be conducted, such as the possible environmental pressure and temperature influences on the measured fluxes. Possible systematics will also be assessed, and background contaminations will be taken under control exploiting more realistic simulations.
The increasing statistics and the higher level of details coming in the near future will be used to confirm the current results and to increase the resolutions of the measurements.

Mu-Ray@Mt. Echia: 3D muography of an unknown cavity

4

4.1 The Mu-Ray project

The Mu-Ray detector, described in section 1.2.2, was designed for volcanology applications, as a prototype of the MURAVES experiment. However, it has been mostly exploited in archaeology investigations and underground inspections. It was intended to primarily prove the validity of the muographic technique to perform the desired measurement, *i.e.* the mass distribution inside an object of large dimensions, and, according to this purpose, has been installed in the underground of Mt. Echia, a little hill in the city of Naples, in Italy. This location is characterized by several underground chambers that can be taken as test structures to prove and characterize the potentialities of muon radiography in the search for underground void regions.

4.2 Mt. Echia

Mt. Echia (Figure 4.1) is a headland with a maximum altitude of about 60 m a.s.l. consisting mainly of yellow tuff; it is located in the San Ferdinando quarteer of the city of Naples, also called *Pizzofalcone*. The subsoil preserves testimonials of an ancient history; its complex of cavities was excavated since prehistory when religious rites were used to take place there. This system of cavities has recently become the subject of systematic investigations and it is partially available to visitors who are curious about the underground history of Naples, with access through the so-called *Galleria Borbonica* that was excavated around the middle of the 19th century. The dispositions of the cavities, located at different heights, is optimal to apply muon radiography. The presence of a cavity is expected to manifest as a local excess of muons respect to the expected flux in the hypothesis of completely fullfilled rock overwelming the detector. The Mu-Ray telescope has been installed, with the sensitive planes arranged horizontally, in two different locations at the lowest accessible level. Successively, an other telescope, called MIMA [50], has been installed in a third location. MIMA (Figure 4.2) is a plastic

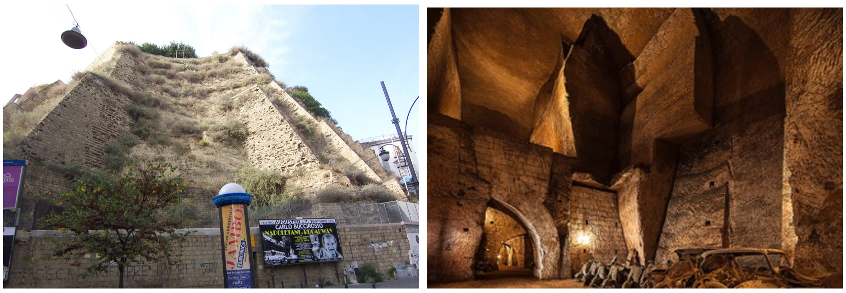

Figure 4.1: Mt. Echia, viewed from the outside (left) and from the inside (right).

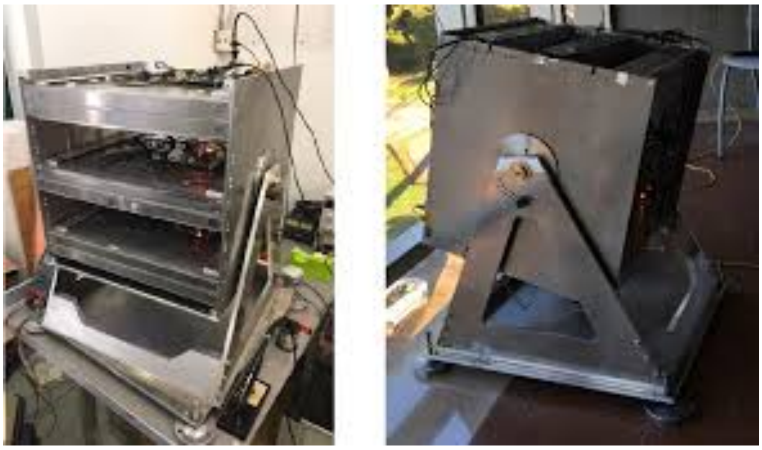

Figure 4.2: The MIMA telescope.

scintillator detector similar to Mu-Ray, consisting of three planes of rectangular scintillator bars, with a sensitive area of 45 cm^2 and it has been realized in synergy between the Universities of Florence and Naples and the INFN. Scintillator bars are directly connected to SiPMs without any optical fiber. The detector is provided by an external structure that can be rotated assuming the preferred orientation.

During the data acquisition periods the underground environmental parameters, temperature, humidity and dew point, have been monitored and found to be quite stable, as can be seen in the plot on Figure 4.3. The first Mu-Ray data acquisition lasted 26 days, corresponding to 14×10^6 acquired trigger events, and the second lasted 8 days, corresponding to 5×10^6 trigger events. MIMA data acquisition lasted 50 days, registering a total of 5×10^6 trigger events.

The trigger logic, applied to both telescopes, requires coincident signals from all planes.

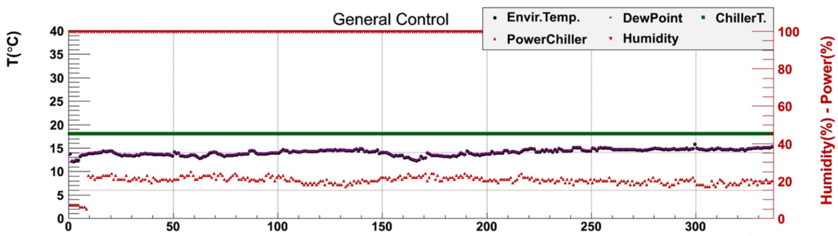

Figure 4.3: Stability of the main environmental parameters: temperature, dew point temperature, chiller temperature and power, relative humidity

4.3 2D muographies

Data taken from each location have been analyzed and cleaned from spurious events. Each event consists in a well-aligned three-dimensional track, defined by the angular coordinates (α, ϕ), where α is the elevation angle and ϕ is the horizontal angle.
Bidimensional maps of the relative transmission $R(\alpha, \phi)$ have been represented in the plane $\phi - \alpha$ with bins of 1×1 deg. The relative transmission is defined as:

$$R(\alpha, \phi) = \frac{T_{obs}(\alpha, \phi)}{T_{exp}(\alpha, \phi; \rho)} \tag{4.1}$$

where T is the transmission defined in eq. (1.17). The expected transmission $T_{exp}(\alpha, \phi; \rho)$ is evaluated with a toy Monte Carlo simulation (see section 4.5) and the ADAMO measurements [51] have been taken as reference for the expected atmospheric muon flux at sea-level. The muon transmission through rock from each direction (α, ϕ) is simulated knowing the corresponding thickness $x(\alpha, \phi)$. Thicknesses are evaluated from the DEM (Digital Elevation Model) of the surrounding area, represented in Figure 4.4. The space overlying the detector is considered fullfilled by yellow tuff, with a density of 1.7 g cm^{-3}, as suggested by the density measurement described in [52]. $R(\alpha, \phi)$ can take values:

- < 1 if, in the corresponding direction (α, ϕ), the opacity $X = x\rho$ is higher than expected. It means longer thickness x or higher density.
- $= 1$ if the expectations are confirmed.
- > 1 if, in the corresponding direction (α, ϕ), the opacity is lower than expected. It means shorter thickness x or lower density.

Thus, if muons encouter a cavity not accounted in the simulation, the condition $R > 1$ should be observed in the corresponding directions.
The three locations where the detectors have been installed are indicated, as colored circles, in Figure 4.5, representing a CAD model of the complex of cavities in the underground of Mt. Echia.
The relative transmission maps resulting from the two Mu-Ray data acquisitions are reported in Figure 4.6. Regions where R significantly exceeds 1 are green in the adopted color scale.
Results from the first investigated location (Figure 4.6 top), have been compared with simulated signals, accounting for known

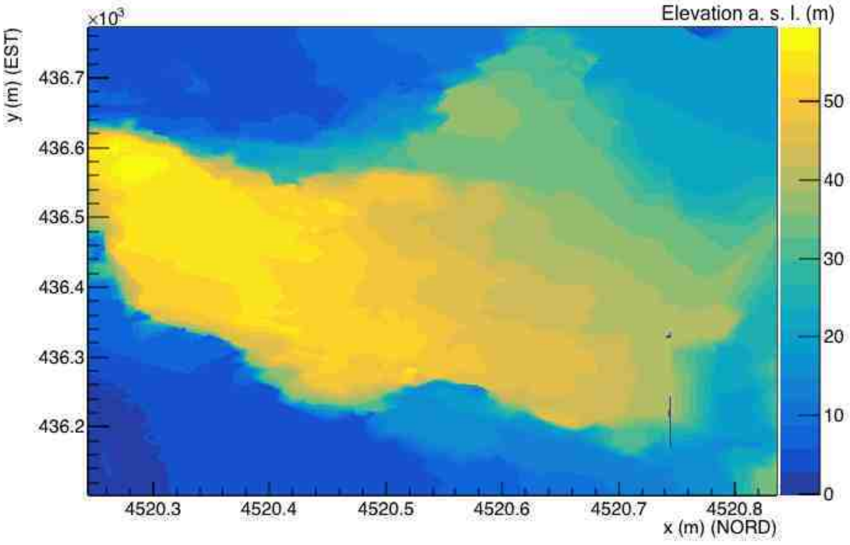

Figure 4.4: Digital Elevation Model (DEM) of the area surrounding Mt. Echia. The histogram is realized using the software ROOT.

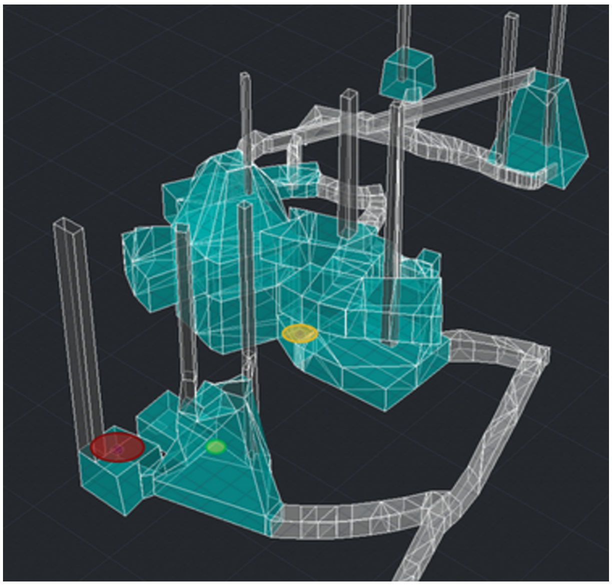

Figure 4.5: CAD Representation of the cavity complex in the underground of Mt. Echia. The three colored circles represent the installation points of the telescopes: Mu-Ray has been installed in the locations indicated with the red and yellow circles, while MIMA has been installed in the location indicated with the green circle.

cavities. Black dots in Figure 4.7 define the contours of the simulated signal corresponding to a particular chamber, taken as *test* chamber. The comparison between expected and observed signals shows a great correspondence.

Other signals, *i.e.* regions with an excess of muons, not corresponding to any of the known chambers emerged from both the muographies obtained with Mu-Ray, opening to the possibility of new surveys of the site. The MIMA muon tracker was thus positioned in a strategic location and orientation to add more and critical information to the images already obtained. The position to install MIMA has been chosen to look at the space region where Mu-Ray previous results showed the possible presence of an unknown void, but from a different point of view. Three different points of view allow to disentangle the possible sources

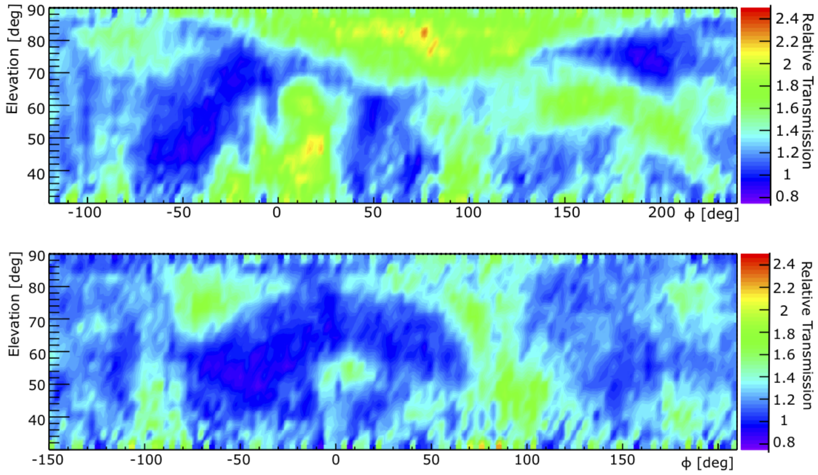

Figure 4.6: Relative Transmission map, measured from the first (top) and second (bottom) Mu-Ray installation point.

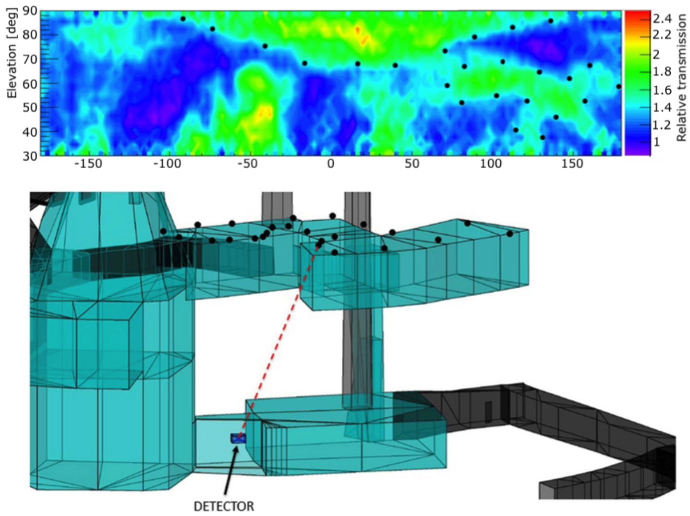

Figure 4.7: Top: Relative transmission $R(\alpha, \phi)$; the black dots lie on the contour of one of the structures which are observed. Bottom: Projection of the black dots in the top figure at z = 25 m, corresponding to the ceiling of a known structure. The drawings were obtained using the software *root* and Autodesk AutoCAD 2015.

of signals and is the minimum number of views, arranged in the best way to surround the object as much as possible, to attempt a three-dimensional reconstruction of a void observed in single muographies.
Muon Radiography obtained with MIMA is represented in Figure 4.8, cleaned from very low statistics bins.

4.3.1 Signal selection

As already explained above, the presence of a void or a low density anomaly manifests itself as a region of the muography in which R is greater than 1. Since the relative transmission can fulfil this condition also due to systematics or statistical fluctuations, an algorithm based on signal clusterization has been developed to select only significant regions [53]. The algorithm assumes that the 1D-distribution of the relative transmission R is the sum

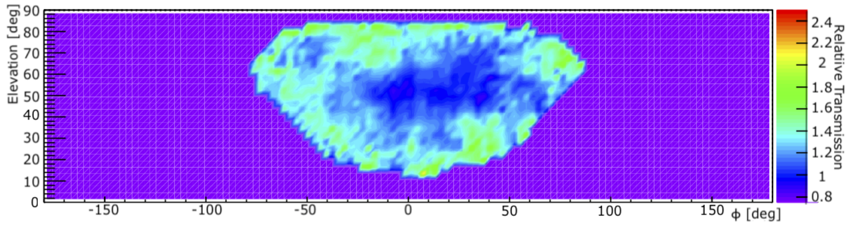

Figure 4.8: Muographic image obtained from MIMA tracks.

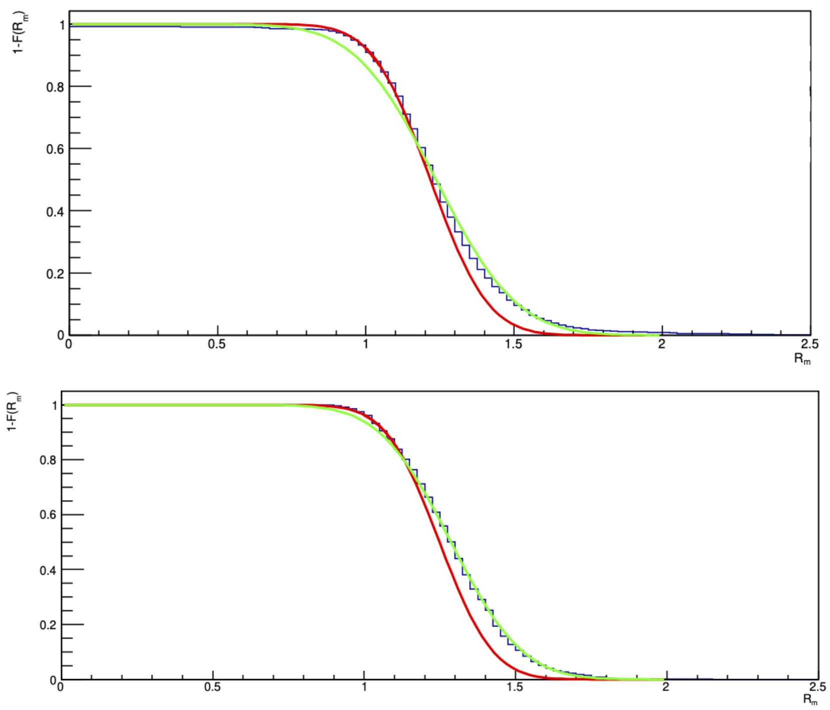

Figure 4.9: Fits of the cumulative distributions of the relative transmission R of the muography taken with the MU-RAY muon tracker at the location B (a) and with the MIMA muon tracker (b). The distributions are fitted by two Gaussian components, one corresponding to transmission through rock without voids (red) and another corresponding to trasmission through rock with voids (green).

of two gaussian components. A first component is generated by the directions from which muons don't encounter voids, and the other corresponds to directions intercepting void regions. Fitting the cumulative distribution of R with two gaussian cumulative curves, the two components have been separated. The cumulative distributions and the curves resulting from the fits are represented in Figure 4.9. These curves have been used to set thresholds to define a signal cluster. The algorithm first searches for signal *seeds*; a seed is a bin of the muography where the probability of the hypothesis that only rock is encountered in the corresponding directions is smaller than 2.5%. This condition corresponds to a threshold for R values, evaluated from the first fitted curve, that is 1.51 for Mu-Ray and slightly different (1.52) for MIMA. Then, adjacent points are aggregated to each cluster, progressively lowering the threshold. Cluster reconstruction stops when no further neibour points have a value of R high enough to be associated to the cluster. The final threshold, 1.37 for MU-RAY and 1.39 for MIMA, corresponds to a probability of the *no-void* hypothesis of the 16% but the request of proximity to

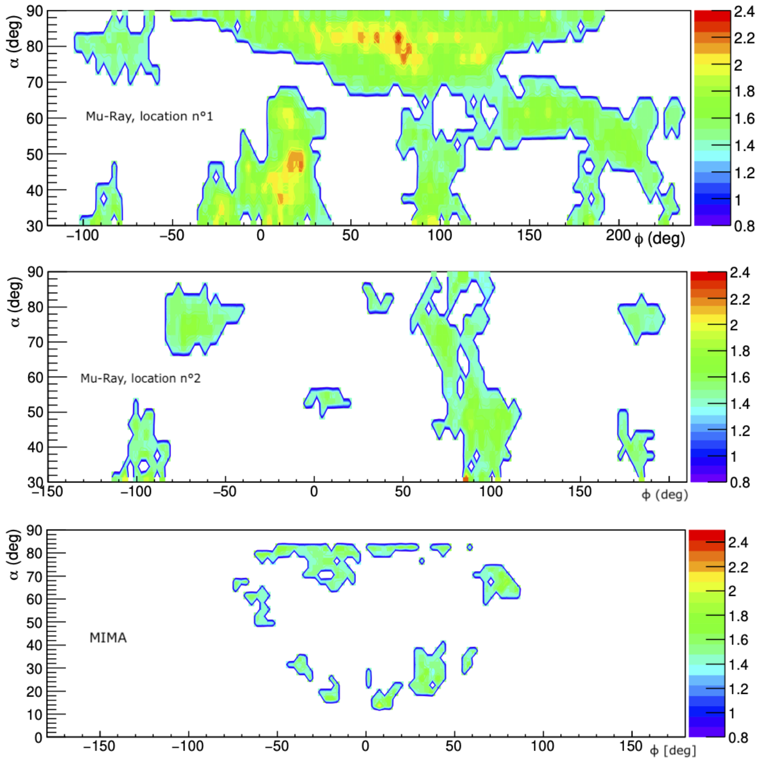

Figure 4.10: Muon radiographies after the application of the selection algorithm.

a *seed* ensures a low background level. Clusters obtained from the application of this algorithm to the muographies in Figures 4.6 and 4.8 are shown in Figure 4.10.

4.4 3D reconstruction

Each of the three *clusterized* muographies in Figure 4.10 presents a signal not associated to known chambers. These signals are highlighted in Figure 4.11 and correspond to directions overlapping in a region of space. These signals have been combined in a three-dimentional reconstruction of the possible source [53], applying the following procedure: defined a grid of points in a cubic volume that encloses the region of space where a cavity is supposed to be, a recursive retroprojection of each point has been applied. If the point, projected on each muography is comprised in a signal cluster in each of the muographies, it is considered inside the 3D model of the unknown chamber. The obtained 3D model is shown in Figure 4.12 in a reference system centered on the installation point of the MIMA detector. It appears as an inclined cavity with a width of about 4 m, a height of 3–4 m and a length of about 7 m. Figure 4.13 shows the hidden cavity inserted in the CAD model of the known cavities. This reconstruction in space of the hidden cavity demonstrates the power

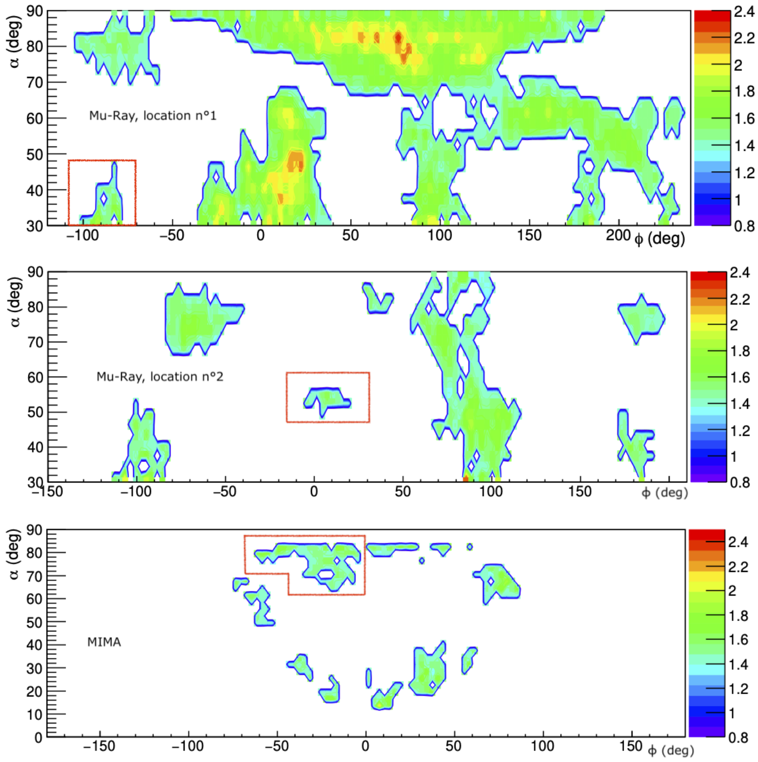

Figure 4.11: Muon radiographies after the application of the selection algorithm; the red rectangles indicate signals not associated to known chambers.

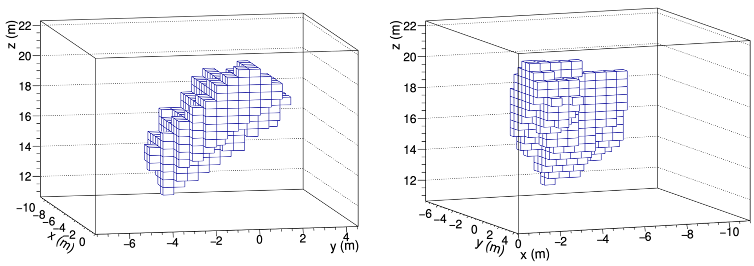

Figure 4.12: 3D reconstruction of an hidden cavity, obtained applying the algorithm described in the text. The origin corresponds to the MIMA installation point.

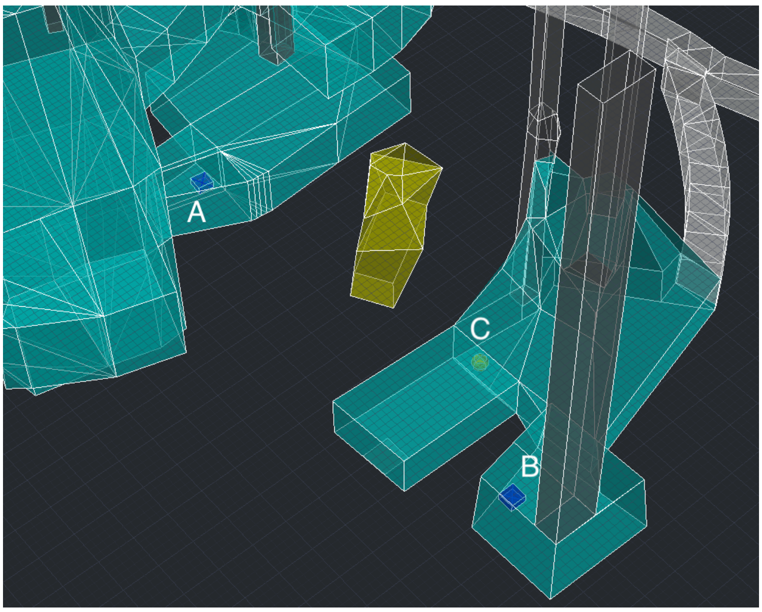

Figure 4.13: The reconstructed cavity, modelled according to the muographic 3D reconstruction and inserted in the CAD modelization of the Mt. Echia undergrond. "A" indicates the Mu-Ray location n°1, "B" the Mu-Ray location n°2, "C" the MIMA location.

Figure 4.14: Positioning of the hidden chamber on the surface.

of our approach to 3D muography in identifying, localizing and reconstructing in space hidden anomalies in complex systems, resolving the ambiguities that affect 2D single muographies. The muographic 3D reconstruction also allowed the positioning of the cavity in absolute geographic coordinates (Figure 4.14), making possible a survey in the corresponding surface area. From this survey a first indication of the real existance of the reconstructed chamber has been found. In fact, a borehole has been found, likely connected to the deeper chamber. A picture of the discovered borehole is reported in Figure 4.15.

Figure 4.15: The result of a survey around the estimated position of the unknown reconstructed chamber.

4.5 Simulations

The simulation engine of this project has a crucial role for both the realization of muon radiographies themselves and for the development and test of the 3D reconstruction algorithm.

4.5.1 Muon flux and transmission

Muographies in Figure 4.6 and 4.8 represent the measured transmission respect to the expected transmission in the hypothesis that no voids exist. To evaluate the expected transmission it is necessary to simulate the muon transport through the yellow tuff. A rock density of 1.71 g cm^{-3} has been considered. The amount of rock muons are expected to cross from each direction before arriving to the detector has been evaluated using the digital elevation model (DEM) of the surrounding area (Figure 4.4). An example of thickness distribution in the $\alpha - \phi$ plane corresponding to one of the Mu-Ray installation locations is reported in Figure 4.16; it shows that the vertical thickness of yellow tuff is about 30 m, while the maximum value of about 180 m corresponds to the horizontal direction, *i.e.* elevation = 0 deg. Anyway, this elevation is under the detector geometrical acceptance; thicknesses corresponding to directions inside the geometrical acceptance of Mu-Ray lay in the range $[30, 70]$ m. The

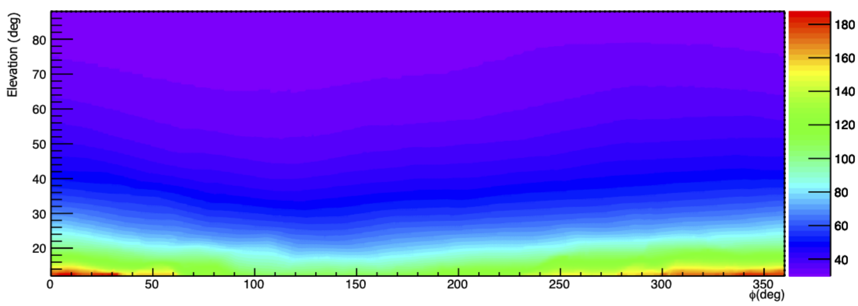

Figure 4.16: Rock thicknesses as sow from one of the installation points of Mu-Ray.

minimum energy needed by muons to cross a thickness $\bar{x}$ in the yellow tuff has been estimated by integrating the approximated formula in eq. (4.2)

$$\frac{dE}{dX} = 1.888 + 0.077 \log \frac{E[MeV]}{105.6} + 3.9E[MeV] \cdot 10^{-6} \quad (4.2)$$

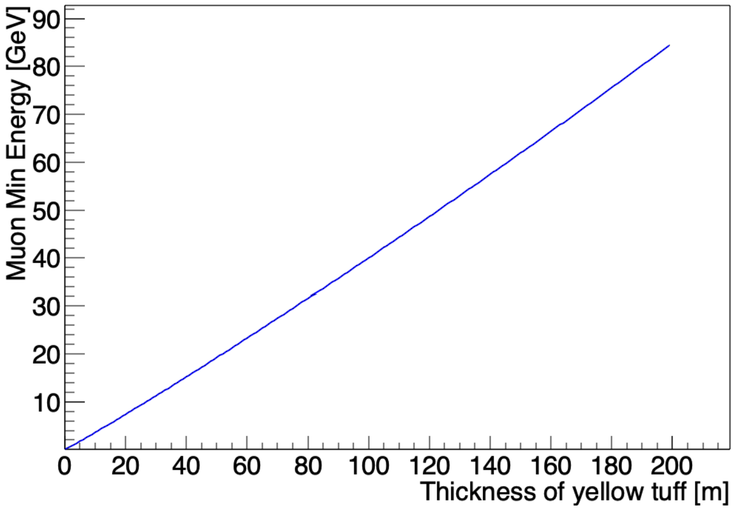

Figure 4.17: Minimum energy needed by muons to survive the yellow tuff ($\rho = 1.71$ g cm^{-3}) respect to the thickness.

introduced in [54] to describe the muon stopping power:

$$E_{min}(\bar{x}) = \int_0^{\bar{x}} \frac{dE}{dx} dx \tag{4.3}$$

$E_{min}(x)$ is represented in function of the thickness x in Figure 4.17. Once the minimum energy for each incoming muon direction has been evaluated, the incoming differential muon flux from the ADAMO measurements [51] has been integrated over the corresponding energy interval. The same procedure is applied to obtain the expected free-sky flux, considering the minimum energy to cross the detector as lower integration limit. The expected transmission is thus calculated as the ratio of the expected flux from the rock and the expected free-sky flux.
In Figure 4.18 the expected transmissions from the three points are represented as a function of the zenith θ and horizontal ϕ angles.

4.5.2 Void shapes, muographic signals and 3D reconstruction

The 3D reconstruction algorithm described in section 4.4 has been tested on synthetic data before being applied to real data. Voids differently shaped have been simulated and included (subtracted) in the rock thicknesses.The 3D algorithm has thus been applied to the resulting transmissions and the obtained 3D model has been compared to the real object.

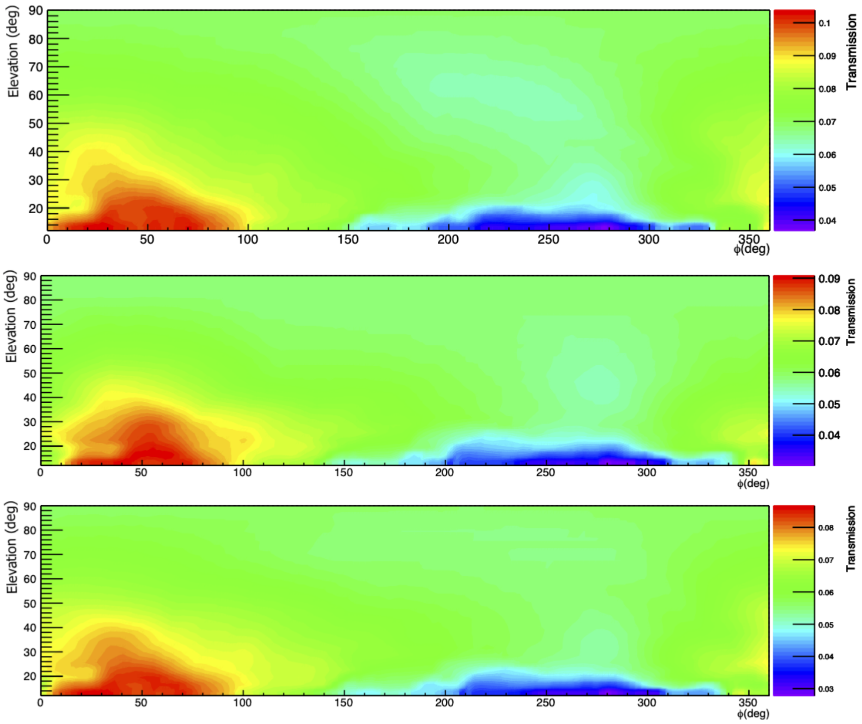

Figure 4.18: Expected transmissions from the positions of Mu-Ray (top,middle) and MIMA (bottom).

In Figure 4.19 the distributions of the expected relative transmissions from each of the real detector locations are reported in the case of a sphere off 3 m radius, simulated approximately in the position of the discovered chamber (section 4.4). Each transmission presents a *shadow* in correspondence of the muon directions intercepting the sphere. The resulting 3D model is shown in Figure 4.21 while the real sphere is represented in Figure 4.20. The obtained 3D muography appears similar to the original sphere but shows an halo above and behind the real object. This halo originates because two of the three point of views partially overlap. The same behavior has been observed in the case of a simulated cubic void, as it can be seen in Figure (4.22), where the real object (blue) is superimposed to the reconstructed model (red). This halo could be reduced by placing the trackers at angles that are more favorable for a triangulation or by increasing the number of trackers locations beyond the minimal number of three used in this work.

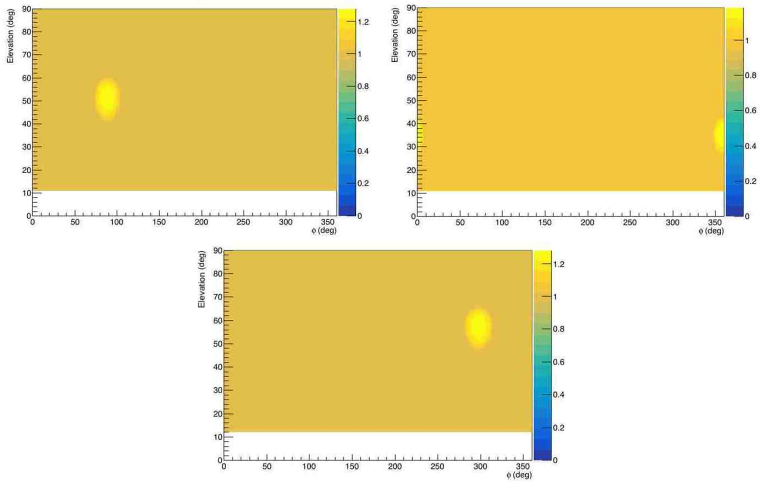

Figure 4.19: Expected relative transmissions of a simulated void sphere of 3 m radius located in the position of the discovered hidden cavity. Top: Mu-Ray, location n°1. Center: Mu-Ray, location n°2. Bottom: MIMA.

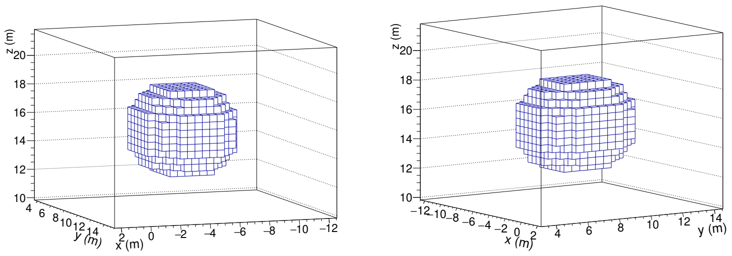

Figure 4.20: The real sphere, simulated to test the 3D simulation algorithm.

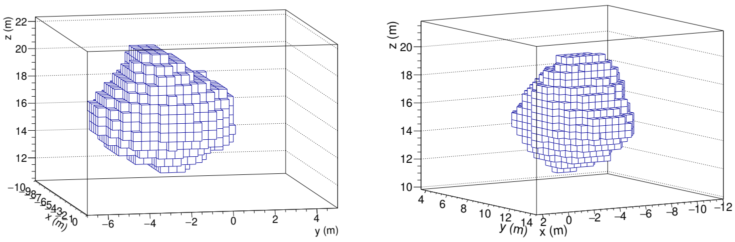

Figure 4.21: The 3D sphere modeled with the 3D reconstruction algorithm described in the text. The reconstructed shape is comparable with the real sphere, except for an halo above and behind the real object.

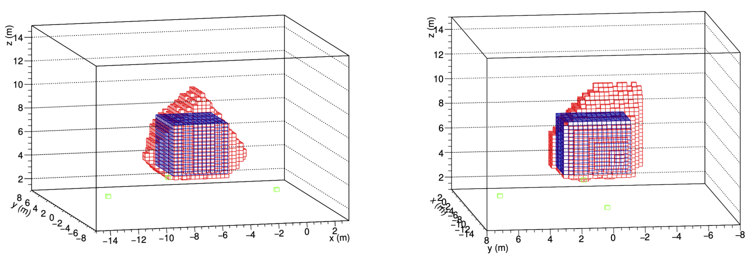

Figure 4.22: Simulated cubic void (blue), of a 6 m side length, and the corresponding reconstructed 3D model (red).

Borehole cylindrical detector 5

The borehole cylindrical detector, described in section 1.2.4, has been designed, realized and developed by the Muon Radiography group of the University of Naples Federico II and INFN. This detector responds to the necessity of a compact and easy to move muon telescope in such cases when one has to deal with the difficulty of finding a proper location where to install the instrument. Often archaeologic and civil applications require to install the detector underground; in some cases a soil perforation is realized on purpose. The cylindrical muon telescope is shaped in the smartest way to be thrusted in a typical drilled well. In this chapter the data analysis, the tests and first applications of the borehole cylindrical detector will be presented.

5.1 Data Analysis

The cylindrical detector trigger requires at least one bar and one arc of the same semicylinder simultaneously fired. A muon crossing a bar, in almost all cases, crosses also an adjacent arc, as represented in Figure 5.1. Even if the trigger logic includes each arc and each bar of the same semicylinder, the two elements should be geometrically correlated, if fired by the same particle. A semicylinder consists in two stacks of arcs, referred as left arcs and right arcs, as represented in Figure 5.2; thus bars with ϕ_{bar} in [0, 90] degrees, geometrically correspond to the right arcs, while bars with ϕ_{bars} in [90,180] degrees correspond to right arcs. If this geometrical condition is fulfilled, the signals are considered in the tracking. The correspondence between the fired arc and bar verifies in almost 90% of the events, referring to a free-sky data acquisition in vertical position. In Figure 5.3 this correspondence is evident in the distribution of the cluster position of the bars, in the two cases when the fired arc is on the right or on the left part of the semicylinder.
The data analysis has some common procedures with the MURAVES analysis (see Chapter 3); in particular the evaluation of the SiPMs pedestal and 1phe values (section 3.5.2) is realized applying the same algorithm. The data taking periods of the

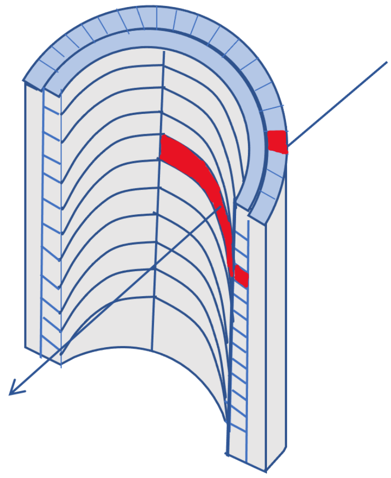

Figure 5.1: Scheme of the passage of muons through a semicylinder. It crosses almost always a bar and the adiacent arc.

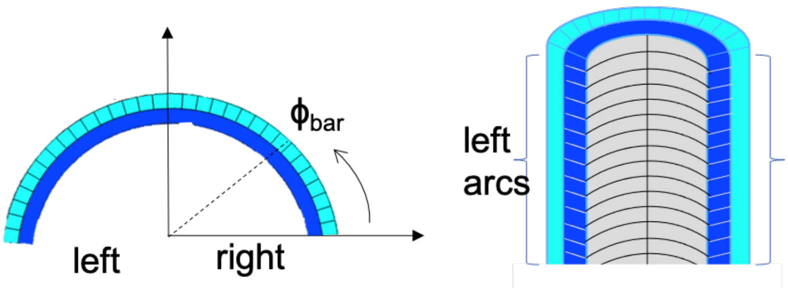

Figure 5.2: Scheme of the geometry of a semicylinder. Right arcs must correspond to bars with ϕ_{bar} in [0,90] degrees; left arcs must correspond to bars with ϕ_{bar} in [90,180] degrees.

cylindrical detector are in general shorter respect to MURAVES, since it is designed for small investigations respect to volcanoes; thus the SiPMs work in almost constant conditions. For this reason, the same ADC counts-to-photoelectrons conversion factors have been applied to all runs of the same dataset, *i.e.* data acquired in the same conditions and in continuous time.
The same MURAVES clusterization procedure is applied on bars and arcs. A signal is considered if it exceeds 5 photoelectrons, reflecting the trigger threshold. The energy of the cluster becomes the sum of the energies of the involved elements; while the position is the weighted mean. Considering a ylindrical coordinates system, arcs measure the z coordinate while bars measure the ϕ coordinate (Fig. 1.16). The corresponding cluster positions are evaluated as:

$$\phi = \frac{\sum_{bars} E_i \phi_i}{\sum_{bars} E_i}, \; z = \frac{\sum_{arcs} E_i z_i}{\sum_{arcs} E_i} \tag{5.1}$$

In a vertical free-sky data acquisition, clusters of bars are composed of less than 3 elements in the 90% of the events, and are single-bar in the 62% of the events. Single-arcs represent the 44%

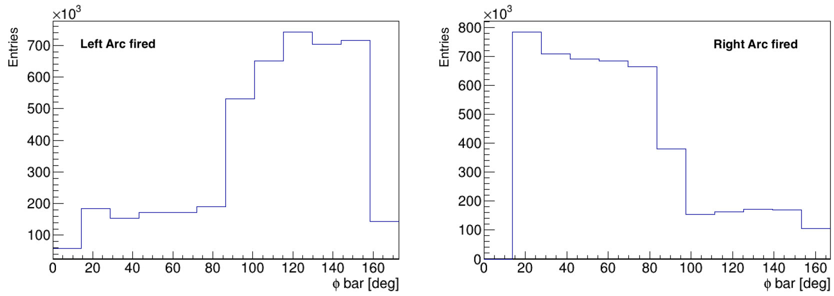

Figure 5.3: Cluster position distribution for the bars on a semicylinder. On the left, the case of left arcs fired. On the right, the case of right arcs fired. Clusters not corresponding to the *correct* arc-stack, are considered not correlated and thus rejected.

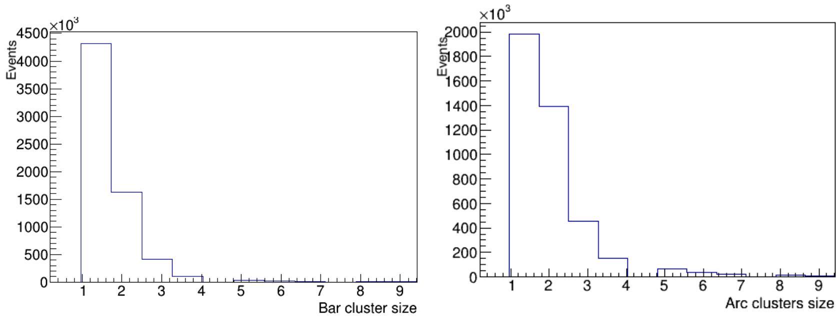

Figure 5.4: Left: cluster size distribution of bar clusters. Right: cluster size distribution of arc clusters.

of the events while arc clusters with size < 3 represent the 81 % of the cases. Bar and arc cluster size distributions are shown in Figure 5.4.

If an event presents at least two points with the double signal *bar/arc*, as explained above, a track (or more) can be defined. All possible tracks are evaluated as the straight lines connecting each combination of the reconstructed clusters. The 72 % of the events in a vertical free-sky data acquisitions do not present any track; this is mainly due to the fact that a single point is required in the trigger rate but two point are necessary to construct a track. The number of tracks in each event is represented in Figure 5.5.

Each track is defined by the couple of angular coordinates (θ,ϕ) that are evaluated from the measured coordinates, z and ϕ, through the relations:

$$\phi_{trk} = \frac{\phi_{in} + \phi_{out} + k\pi}{2} \tag{5.2}$$

$$\theta_{trk} = 2\frac{\sqrt{|R_{arc}^2 - R_{bar}^2 \cos^2 \frac{\delta}{2}|}}{\Delta z} \tag{5.3}$$

where $\delta = \phi_D - \phi_A$ (see Figure 5.6). Formula (5.3) accounts for the difference between the position where the muon crosses the bar, that gives the measured ϕ and the position where the muon crosses the corresponding arc, that is related to the measured z.

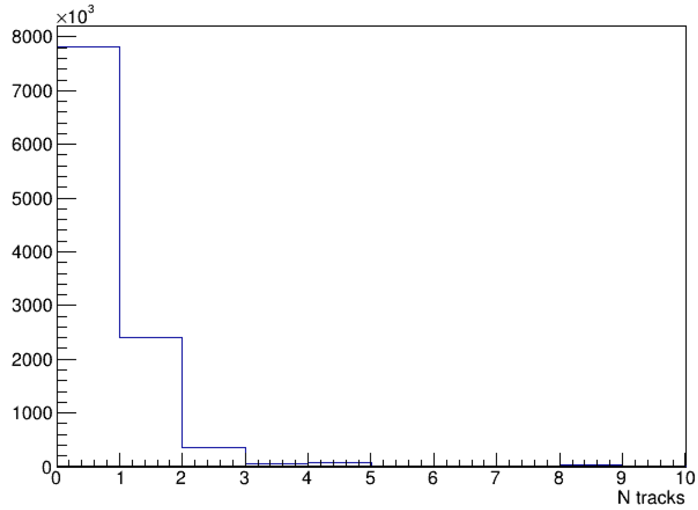

Figure 5.5: Distribution of the number of tracks reconstructed in each event. Data refer to a free-sky data acquisition in vertical position.

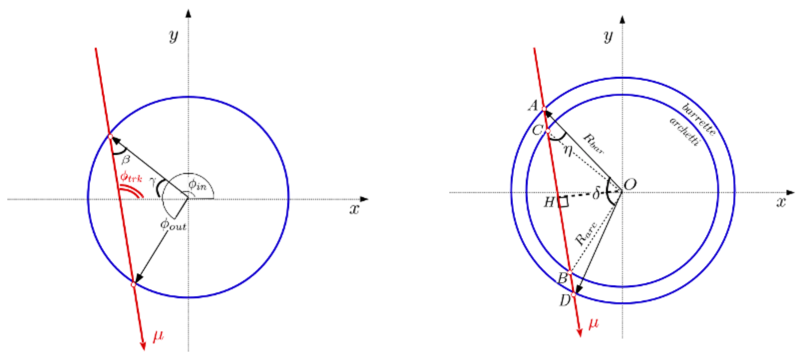

Figure 5.6: How the track coordinates are obtained from the measured ϕ and z

5.2 Free-Sky tests

The first data acquisition of the cylindrical borehole detector, after the test phase, has been a free-sky acquisition, on the roof of the department of Physics at the University of Naples. The detector has been oriented vertically, *i.e.* with the z-axis corresponding to $\theta = 0$. The measured trigger rate in this configuration is ~ 33 Hz while the tracking rate is 9.8 Hz. The discrepancy is due to both the events where the bar and arc, responsible of the trigger coincidence, are not correlated, and the events where a single point is registered, not enough to be considered as a particle signal. The vertical free-sky dataset consists of about 91.6 hours, for a total of 10880000 trigger events. The 28 % of these events provides at least a track; these events have a single track in the 80% of the cases; while the 12% presents two tracks and the remaining 8 % more than two tracks. In the events where more than one track is reconstructed, only one must be selected. The best track is considered to be the track with the highest total energy, *i.e.* the sum of the energies of all clusters involved in the track. The choice of this selection criteria is imposed by the

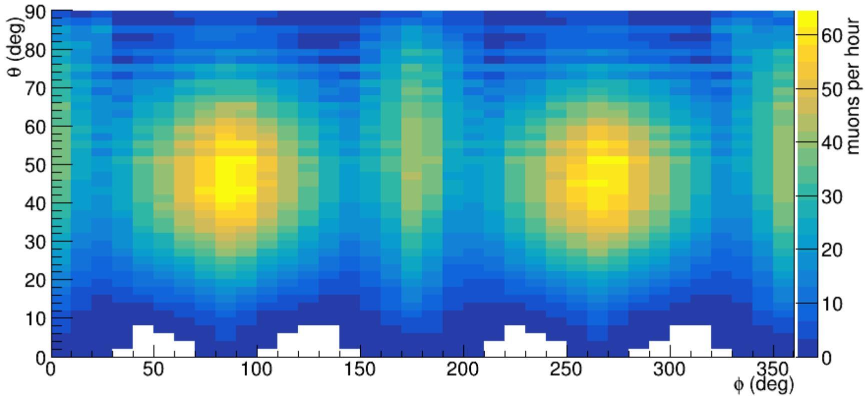

Figure 5.7: Tracks observed by the detector when exposed to the muon flux from free-sky, for 90.6 hours. The geometrical dead zones at low zenith angles are distinguishable. The angular binning is $(\Delta\theta, \Delta\phi) = (2°, 10°)$.

fact that tracks are composed by only two points, such that no alignment considerations can be done.

The observed (θ, ϕ) distribution of this dataset is shown in Figure 5.7. It has been compared with the expected muon flux obtained from a toy Monte Carlo simulation, shownin Figure 5.8. The toy Monte Carlo consisted in the simulation of an approximated geometrical factor distribution, shown in Figure 5.9. The approximation consists in ignoring the discretization of bars and arcs, and thus the dead spaces between the scintillating elements. The expected muon flux has been obtained by combining the simulated geometrical factors with the expected muon flux from the Gaisser's model in eq. (1.8). Figure 5.10 shows the

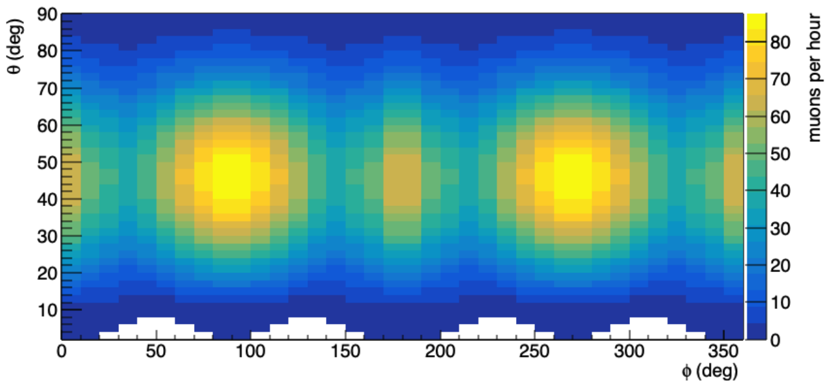

Figure 5.8: Expected muon flux evaluated with a toy Monte Carlo. The toy doesn't account for detector efficiencies except of the geometrical acceptance, shown in Figure 5.9. The flux has been evaluated from eq. (1.8).

distributions of the measured and expected fluxes, integrated over the horizontal angle ϕ, as a function of the Zenith angle θ. Distributions in Figures 5.8 and 5.7 are in good agreement considering that the simulation is not detailed.

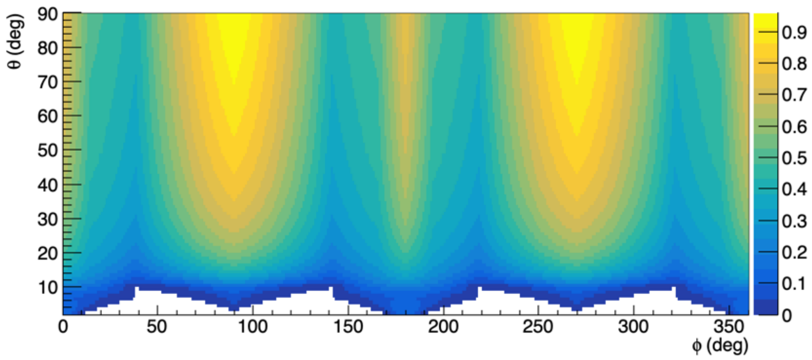

Figure 5.9: Simulated geometrical acceptance of the borehole cylindrical detector in the vertical position. It has been obtained by a toy Monte Carlo, not considering the separation between the sensitive elements.

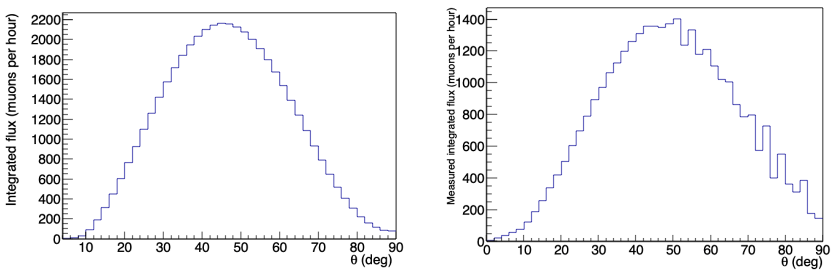

Figure 5.10: Left: expected muon flux integrated over the horizontal angle. Right:measured muon flux integrated over the horizontal angle.

5.3 Measurement campaign @ Galleria Borbonica

To test the newly developed muon detector on a real field, it has been installed in the scenario of the *Galleria Borbonica* in the underground of Mt. Echia, already known by the past experience within the Mu-Ray project (Chapter 4). This choice has been motivated by several advantages; first of all, the practicality of the site, meaning that it is near, easily accessible, and well known. At the same time this site still offers challenges and interesting possible investigations, due to the hugeness of the galleries, and the mysteries that are still not completely understood. A second motivation driving to the choice of test the detector in this scenario is the possibility to apply and refine the 3D reconstruction algorithm (sec. 4.4) by easily moving the cylindrical detector in different points around a target chamber. The cylinder is easier to move respect to a planar muon tracker and gives the possibility to acquire data from several points around the a particular targeted object. Therefore, to summarize, the Galleria Borbonica site allows to both test the proper functioning of the cylinder in a typical muon radiography environment, and to perform and improve the three-dimensional reconstruction algorithm using known chambers.

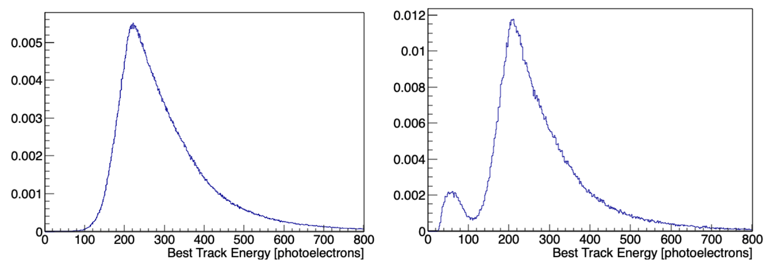

Figure 5.11: Comparson between the track energy distribution in the free-sky data acquisition, and the same distribution for data acquired in the Galleria Borbonica underground site. In both cases the cylinder have been installed vertically.

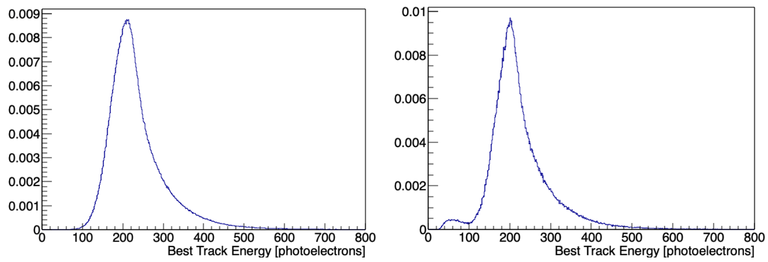

Figure 5.12: Comparson between the track energy distribution in the free-sky data acquisition, and the same distribution for data acquired in the Galleria Borbonica underground site. In both cases the cylinder have been installed horizontally.

5.3.1 Data Acquisition

The detector has been moved in 5 different locations; in the first location it has been installed horizontally, while in the other positions it has been installed vertically.
The first data acquisition showed an unexpected high trigger rate, then confirmed by the other points. The measured trigger rate was ~ 63.7 Hz, significantly higher than the free-sky trigger rate in the same orientation (horizontal), that was measured to be ~ 40 Hz. The vertical positions, presented this discrepancy as well. It is obviously impossible to address this rate to muons, since, under tens meters of tuff, the muon rate is expected to reduce to about the 10%. The muon rate reduction is in fact confirmed by the evaluated tracking rate, that is ~ 1.2 Hz in the gallery and ~ 12 Hz in free-sky (similar results in the vertical position). The source of this not-muons triggers is still not well understood, but it is probably due to photons produced by the radioactivity of the tuff and capable of survive the 2 mm steel shell of the cylinder reaching scintillators and provoking a trigger signal. Some considerations has thus been done to free the statistics from this contamination. This background in most cases doesn't generate a coincidence of 4 clusters, however, in the reconstructed tracks a polluted ~ 5.5 % contribution has been identified and rejected. These tracks have be recognized by considering their total energy, *i. e.* the sum of the energies of the four clusters composing the track. As can be deduced from the energy distribution comparison between gallery and free-sky data reported in Figures 5.11 and 5.12, data acquired in the gallery present a secondary peak at about 50 photoelectrons, not seen in the free-sky case. It has been checked that this

component is not addressable to some noisy element. On the basis of these observations, it is necessary to remove this contribution from the data. To this purpose, tracks with energy above 100 photoelectrons have been selected.

5.3.2 Dead time correction

The measured muon flux has to be corrected for the DAQ dead time that depends on the trigger rate and is thus different between free-sky acquisition and underground data acquisition. This correction accounts for the inactivity of the system the time immediately after a trigger. This dead time is independent from the event and the acquisition rate, and is $T_{dead} = \nu_{max}^{-1} = 4$ ms, where $\nu_{max} = 250$ Hz is the DAQ maximum rate. The real rate of particles is thus related to the measured rate by the formula:

$$\nu_{real}^{\mu} = \frac{\nu_{meas}^{\mu}}{1 - \frac{\nu_{tr}}{\nu_{max}}} = \frac{1}{\epsilon_{DAQ}} \nu_{meas}^{\mu} \tag{5.4}$$

The efficiency ϵ_{DAQ} has been measured of ~ 0.75 for free-sky data acquisitions and ~ 0.67 for underground data acquisitions.

5.3.3 Results and comparisons

As mentioned above, the cylindrical muon telescope has been installed in five locations within the Mt. Echia's underground. In each location the exposure lasted a reasonable time to reach a mean statistical error of the order of the 10%, in angular bins large 3×3 deg^2. In table 5.1 the collected statistics and the durations are reported for each dataset. Figure 5.13 shows the distribution of events obtained from the different five locations in a bi-dimensional map (θ,ϕ) of bins large 3×3 deg^2. The *Point 1* location is inside the so-called *Pool room*, where the Mu-Ray

Location	Tracks	Time (days)
Point 1	562873	5.4
Point 2	252191	3.8
Point 3	445116	11.5
Point 4	305137	6.4
Point 5	703058	13.2

Table 5.1: Collected tracks and relative acquisition durations of the 5 datasets, taken from different locations. Dead-times are already subtracted.

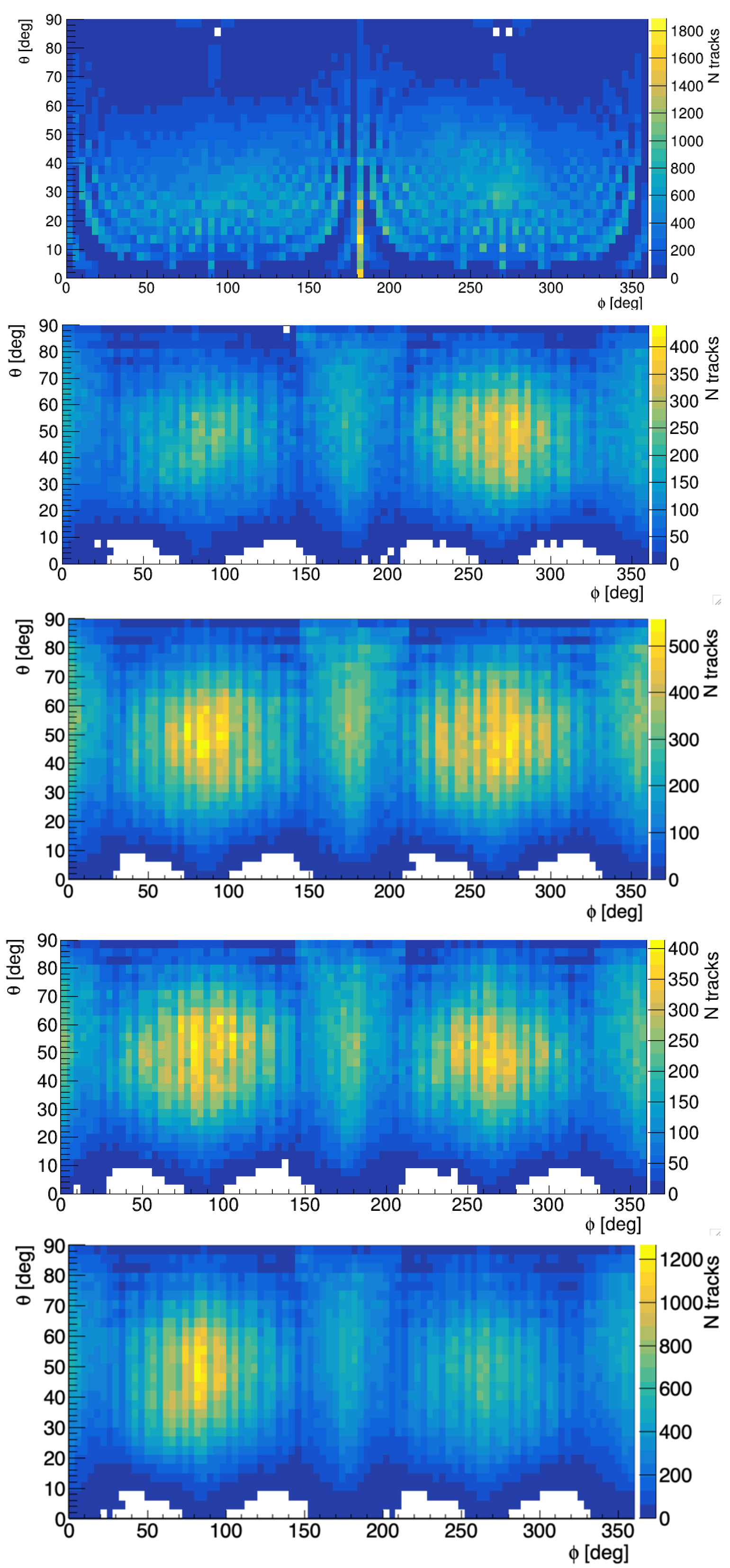

Figure 5.13: Track distributions in θ, ϕ coordinates, From top to bottom: Point 1 (pool room), Point 2 (tank room), Point 3 (corridor), Point 4 (other corridor), Point 5 (tank room).

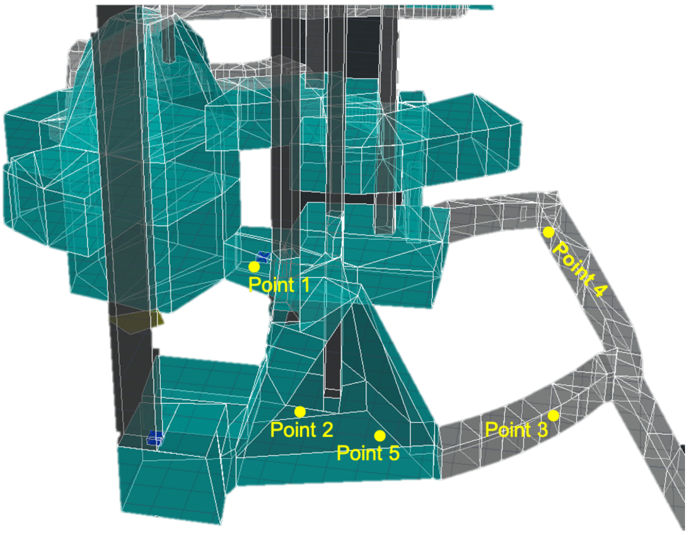

Figure 5.14: Locations where the cylinder has been installed in the Mt. Echia underground. The locations are highlighted in thee CAD model of the known complex of cavities.

telescope was already installed in the past. Here the detector has been installed horizontally, thus the corresponding distribution appears different from the others. Points 2 and 5 are inside the *tank* room and the Points 3 and 4 are located inside two corridors. The different locations are highlighted in Figure 5.14.

Comparison with Mu-Ray previous results

A first check to verfy the proper functioning of the new borehole cylindrical detector comes from the comparison between the resulting muographies from the Pool room location (Point 1) from the cylinder and Mu-Ray data. As it can be seen in Figure 5.15, Mu-Ray and the cylindrical detector have been installed in very close positions. Figure 5.16 shows the two relative transmission distributions obtained from the two different detectors. It is evident that the two detector see the same signals. In Figure 5.16 the muon radiography from the cylinder is cut below an elevation of 30 degrees to be comparable with the Mu-Ray geometrical efficiency.

Muon Radiographies from the tank

As already mentioned, the cylinder was moved in two different locations in the so-called tank room. The corresponding relative transmission have been evaluated without considering any cavity in the expected transmission. They are represented in Figure 5.17. Both muographies have a region with R greater than 2. The two regions are compatible with each other. To better understand the source of this highly significative signals, the structure of

Figure 5.15: The cylindrical detector (left) and the Mu-Ray detector (right) installed around the same point in the Pool room.

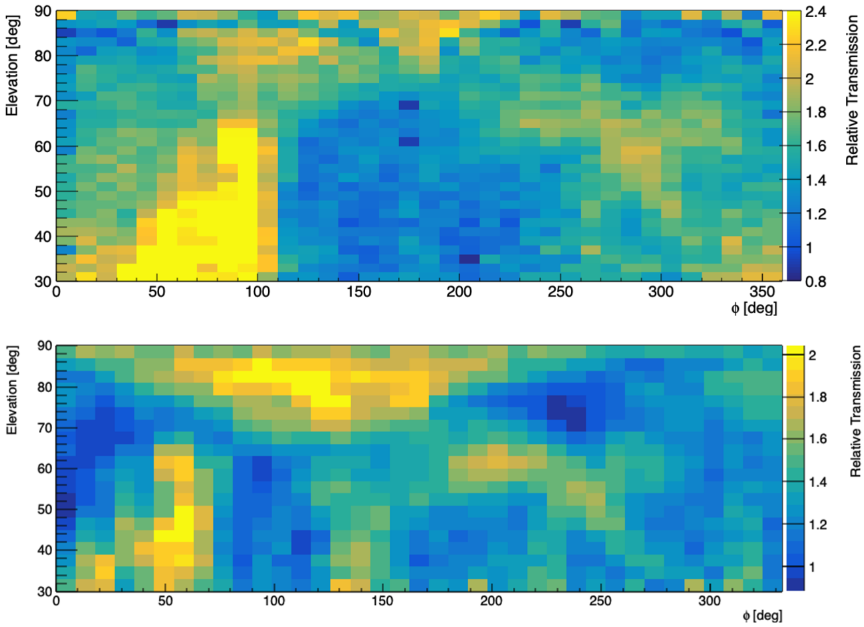

Figure 5.16: Comparison between the cylinder's (top) and Mu-Ray's (bottom) muographies obtained from the same location, the Pool room.

the tank was approximately reproduced in a 3D ROOT object (Figure 5.18) and included in the evaluation of the expected transmission. The expected contribution of the tank room to the relative transmission has been assessed and is represented in Figure 5.19 for the two different points. The results led to understand that the observed significant signals discussed above are related to the tank itself. The relative transmissions were thus re-evaluated including the simulation of the tank in the expected transmission. The corrected muographies are represented in Figure 5.20.

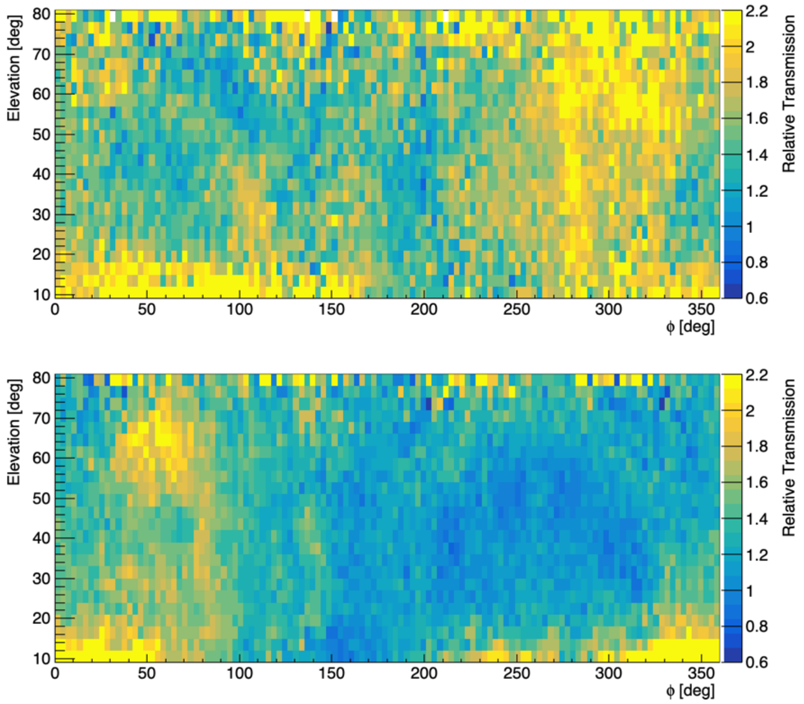

Figure 5.17: Relative Transmission obtained from the two locations in the tank room. The expected transmission does not account the known cavities. Top: Point 2: a significant region with R > 2 is visible at a mean ϕ of 300 degrees and a mean elevation of 60 degrees. Bottom: Point 5: a significant region with R > 2 is visible at a mean ϕ of 70 degrees and a mean elevation of 60 degrees.

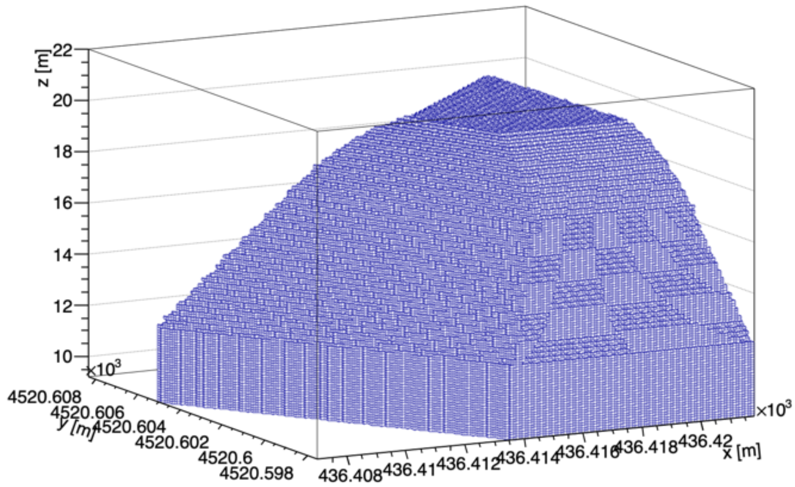

Figure 5.18: Reconstruction of the tank chamber in ROOT. This approximated reconstruction has been used to account for the tank void space in the simulations.

3D reconstruction target chamber: preliminary observations

The installation of the cylindrical detector in different positions inside Mt. Echia is aimed at applying the 3D reconstruction algorithm, already used in the past experience of the Mu-Ray project. To this purpose, a known chamber has been chosen and is highlighted in Figure 5.21 together with the 5 observation points. This chamber has been chosen since it is observable from several points of view accessible in the Gallery.

As preliminary step toward this goal, the test chamber has been simulated and the expected angular regions where the chamber

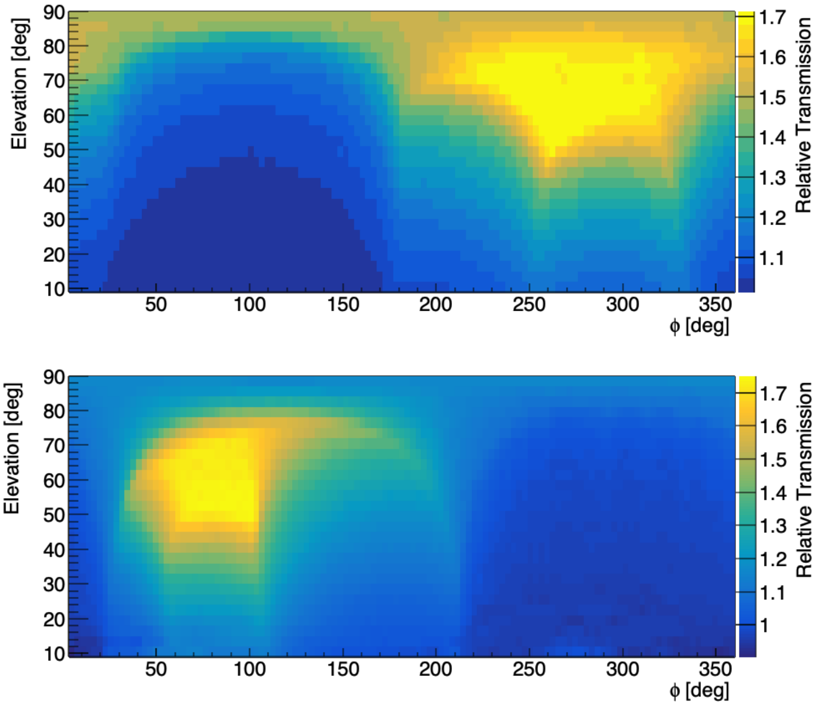

Figure 5.19: Expected contributions of the tank room to the relative transmission observed from the Point 2 (top) and the point 5 (bottom).The relative transmissions have been obtained as the ratio between the expected transmission considering the presence of the empty tank room, and the expected transmission when no voids are considered, *i.e.* the entire space above and around the detector is considered to be filled with yellow tuff.

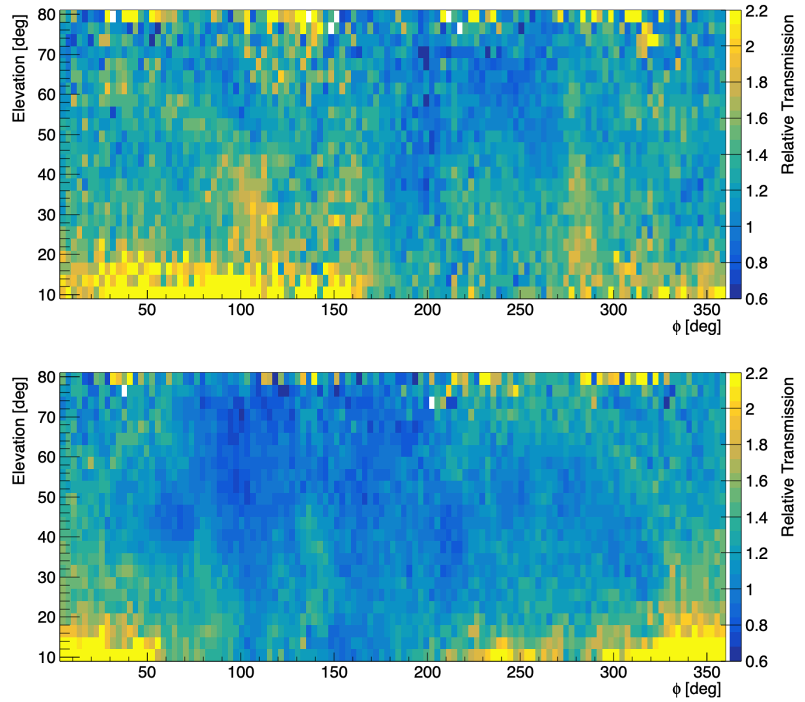

Figure 5.20: Relative transmission distributions from Point 2 (top) and Point 3 (bottom) obtaned by including the effect of the tank room in the expected transmission. The most significative signals, observed in Figure 5.17 almost disappered.

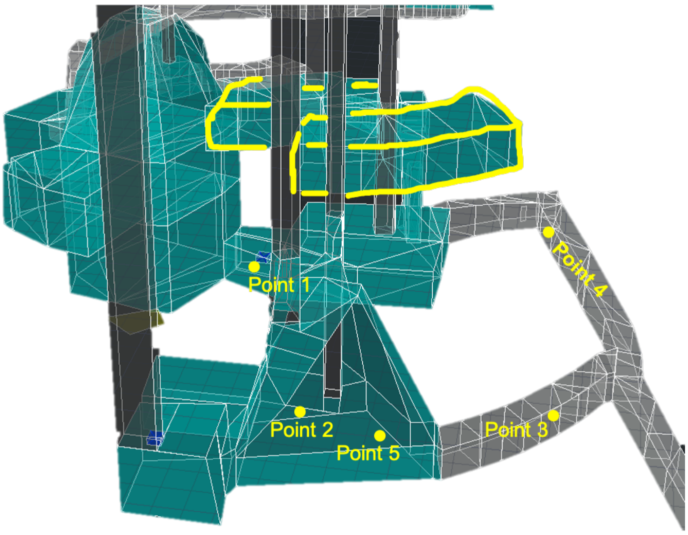

Figure 5.21: Chamber taken as test structure to apply the 3D reconstruction algorithm exploiting the cylinder muographies.

should manifest in each muography have been evaluated. The observed muon radiographies are reported in Figure 5.22 together with the contours of the expected signal from the test chamber. As can be observed in Figure 5.22 each of the 5 muographies presents in the region within the expected contours values of the relative transmission, R, significantly above the unity. Currently, the data are still being analyzed to determine the significance of the observed signals, and all the possible known cavity are beeing simulatated to be included in the expected transmission. The prospectives for the early future are: from one side, to determine the significant signals in the obtained muographies and to understand, where possible, the sources; from the other side to apply the 3D reconstruction algorithm on the test chamber and to use the resulting three-dimensional image to improve the capability of the algorithm to reconstruct the exact geometry of a cavity by comparing the reconstructed and the real chamber shapes.

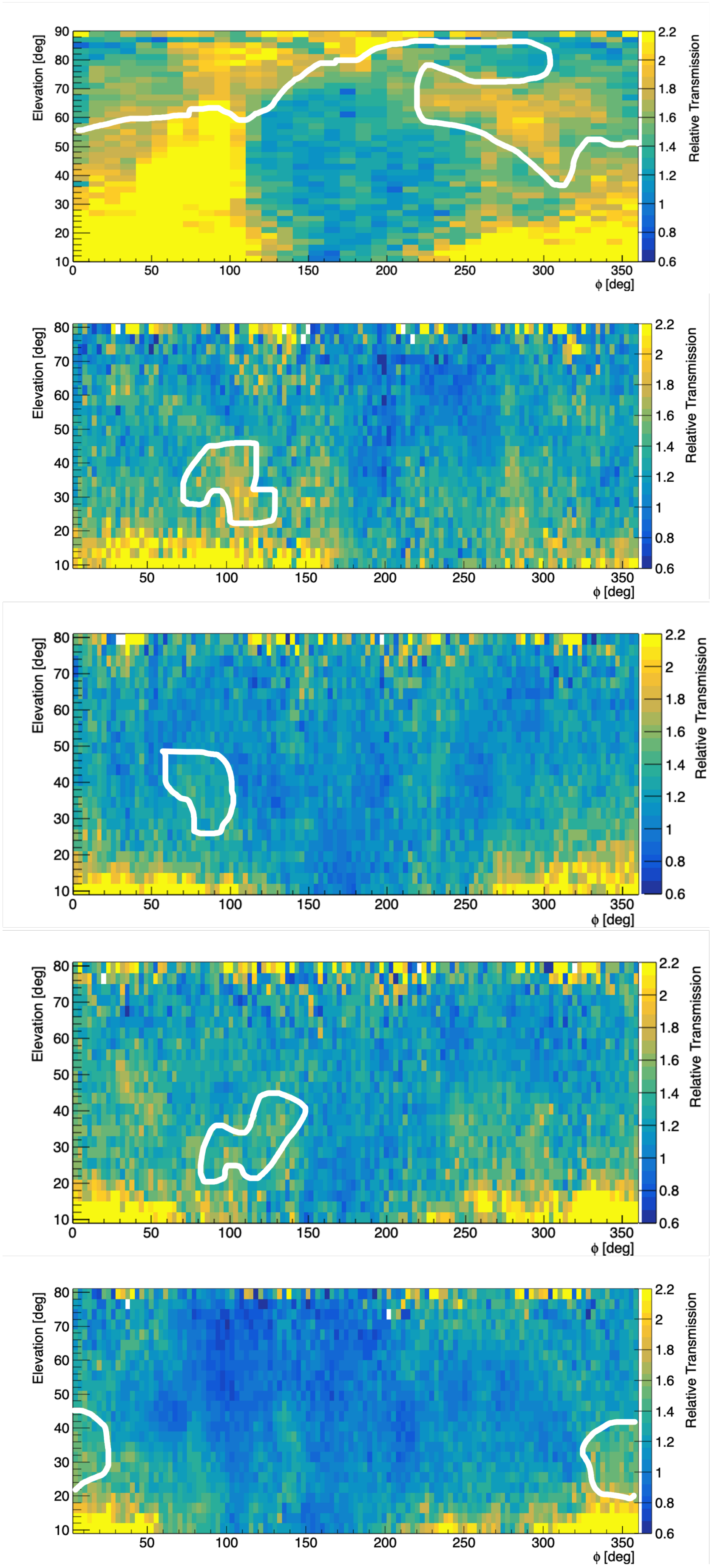

Figure 5.22: Muon radiohraphies obtained from the 5 different locations, from Point 1 to Point 5, starting from the top. Each muography presents the contours of the expected signal generated by the test chamber and each one present correspondingly a R mean value significantly above 1.

Conclusions

Different applications of muon radiography have been presented in this work, after a brief introduction to the technique in general and an overview of the main results from different groups all over the world.
This thesis is part of the research work of the author in synergy with the muography group of the University of Naples Federico II & INFN and collaborators. Three main research topics have been discussed in here: The MURAVES experiment, The Mu-Ray project and the development of a new muon telescope.

The MURAVES experiment aims to investigate the interior of the summit of Mt. Vesuvius. In particular, the possible existence of a layered structure of different density materials, suggested by volcanologists, could be highlighted by muography. Currently the experiment is at its initial stages; the acquired and analyzed statistic is still low respect to the final goal of the experiment. However, a complete data analysis engine, from the raw data to a density evaluation, have been developed and deeply described in this work. Preliminary results have been translated in relative densities between two sides of the volcano, on three different depths. The observed density ratios show discrepancies respect to 1 of +1.5, -0.67 and -2 sigmas respectively from the highest to the deepest layer. These values are a hint of possible density asymmetries between the two sides of the volcano, but the significance level is still not sufficient to interpret this observation as an evidence.
The MURAVES telescope is meant to collect data for at least one or two more years to reach an higher significance of the results. At present, more data are being acquired and analyzed. Many improvements are being developed and many more are prospected on both simulation and analysis chains. One of the main goals for the future is to better assess background contaminations and possible systematics.

The Mu-Ray telescope, born as first MURAVES prototype, has been developed in underground investigations, particularly intended to the discovery of voids or density anomalies in the overlying rock. This kind of application is of particular interest in the field of civil engineering, archaeology and geophysical prospections.
In this context, muographies taken from three different points in the underground of Mt Echia have been combined resulting in a three-dimensional model of an hidden void 4 m wide, with a height of 3-4 m and a length of 7 m. The results and the 3D reconstruction algorithm are described in this work. The algorithm also allowed to locate the cavity in space; a survey conducted in the corresponding position on the surface resulted in an indication of the real existence of the void chamber. In fact, a borehole was found and, according to speleologists and archaeologists, it is probably a connection to the deeper chamber, observed with only mugraphic investigations.

The third topic described in this work concerns the development of a new muon telescope for muon radiography applications. The telescope is a borehole cylindrical detector, designed to fit into boreholes of 25 cm diameter. The shape and compactness of this new detector is particularly advantageous for underground investigations. This detector has been recently realized and is currently at the initial stages of development. The test phase and preliminary applications are described in this thesis. A free-sky data acquisition has been performed and compared with a simulation obtaining a good agreement. A first measurement campaign has been conducted, and is still on going, in the Mt. Echia underground, already known from the past experience within the Mu-Ray project. The goal of this campaign is to both test the performances of the cylindrical detector in a typical environment for which it is designed, and to improve the three-dimensional mugraphic imaging developed within the Mu-Ray project. Currently, preliminary results proved the proper functioning of the detector and the capability to distinguish existing cavities with few days of data acquisition. Five different muographies have been realized and simulations are being provided to reproduce all the expected signals from known chambers. The main plans for the early future are to highlight the possible unexpected signals and to test and improve the 3D reconstruction algorithm, applying it to an existing test-void, using an higher number of points of view respect to its past applications.

Appendix

A MURAVES Time of Flight

The Time of Flight system has been implemented in Mu-Ray and MURAVES telescopes to prevent data to be polluted by the albedo tracks, which could imply some bias in the density measurements. In principle, the discriminating quantity is the sign of the time difference between the last and the first planes: if $t_\mu^4 > t_\mu^1$ the muon is down-going, while in the opposite case the muon can be considered upward going and thus neglected. The ToF measurement is possible thanks to a system integrated on each FEE board consisting in a capacitor and a TDC, explained in sec. 1.2.2. When a muon hit a plane, the corresponding FEE board generates a fastOR signal and the capacitor starts charging. When the last plane hit by the muon sends its fastOR to the Master board, it sends back a STOP signal to all the slaves and the capacitors stop their charge processes and start to discharge. The discharging time of the *i-th* plane (the involved board) is proportional to the time difference $t_i^{start} - t^{stop}$. The TDC measures the time:

$$t_i^{meas} = (t^{stop} - t_i^{start}) \cdot E_i \tag{A.1}$$

where E_i is the *expansion factor* of the involved board. If the instant t_i^μ is the time of the muon passage through the i-th plane, the t_i^{start} depends on the position of the impact point within the corresponding scintillator bar. Indeed, the light needs a certain time, Δt_i^γ, to reach the photosensor. So the t_i^{start} time can be written as:

$$t_i^{start} = t_i^\mu + \Delta t_i^\gamma \tag{A.2}$$

The t^{stop} is common to all the involved FEE; the difference between the time measured by the first and the last planes is:

$$t_1^{meas} - t_4^{meas} = (t^{stop} - t_1^{start}) \cdot E_1 - (t^{stop} - t_4^{start}) \cdot E_4 \tag{A.3}$$

In eq. A.3 we can substitute eq. A.2:

$$t_1^{meas} - t_4^{meas} = (t^{stop} - t_1^\mu - \Delta t_1^\gamma) \cdot E_1 - (t^{stop} - t_4^\mu - \Delta t_4^\gamma) \cdot E_4 \tag{A.4}$$

the expansion factors are usually different board by board and have been evaluated during the calibration of the electronics; if

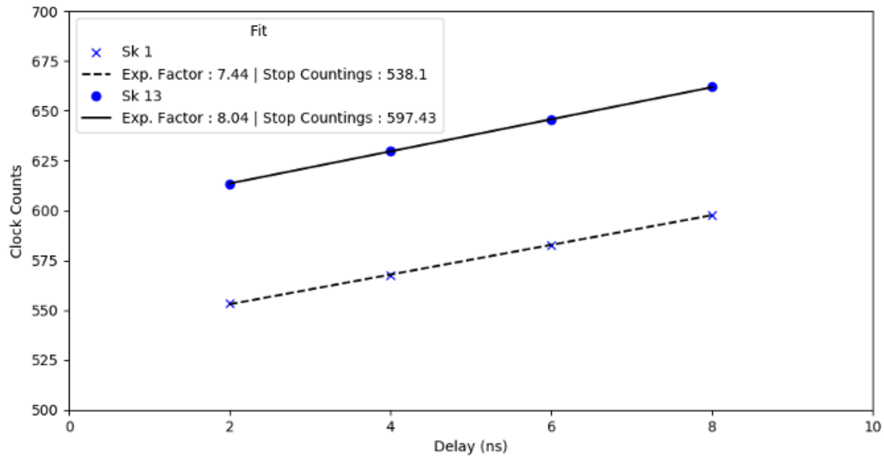

Figure A.1: Calibration of the TDC of the boards number 1 and 13. The plots represents the measured times obtained by varying the delay between start and stop signals.

each measured time is divide by the corresponding expansion factor one obtains:

$$\frac{t_1^{meas}}{E_1} - \frac{t_4^{meas}}{E_4} = t_4^{\mu} - t_1^{\mu} + \Delta t_4^{\gamma} - \Delta t_1^{\gamma} \qquad \text{(A.5)}$$

where $t_4^{\mu} - t_1^{\mu} = \pm\Delta t_{\mu}$ is the time taken by the muon to cross the detector. If the particle crosses the detector down-going, from the 1st to the 4th plane, the sign is positive while, if the direction of the particle is upward, it intercepts the 4th plane first, so the sign is negative, and its measurement allows to recognize the background particles.

The TDC measurement depends on two parameters, the expansion factor E_i and a baseline time value T_i^0; these parameters can be obtained in a dedicated calibration of the TOF system, by forcing a start and stop, electrically varying the time distance between them. Taking few points and fitting the distribution of time measured vs the imposed delay between start and stop, the two parameters can be evaluated (Figure A.1). To obtain the time defined in eq. A.1, one needs to subtract the T^0 value from the TDC counts, $t_i^{meas} = T_i - T_i^0$, where T is the TDC output.

To test and study the ToF system performances a dataset taken by the detector named BLU during a test phase in laboratory has been used, in absence of the lead wall. In Figure A.2 the histogram of the measured ToF = $\frac{t_1^{meas}}{E_1} - \frac{t_4^{meas}}{E_4}$ are shown. Events where the fired boards in planes 1st and 4th are the number 1 and 13 respectively were selected. These boards readout two modules of the

planes which measure the z-coordinate. A first manipulation of this quantity is the subtraction of the contribution of the light propagation time along the fibers. This correction is possible considering the path of the light along the fiber before reaching

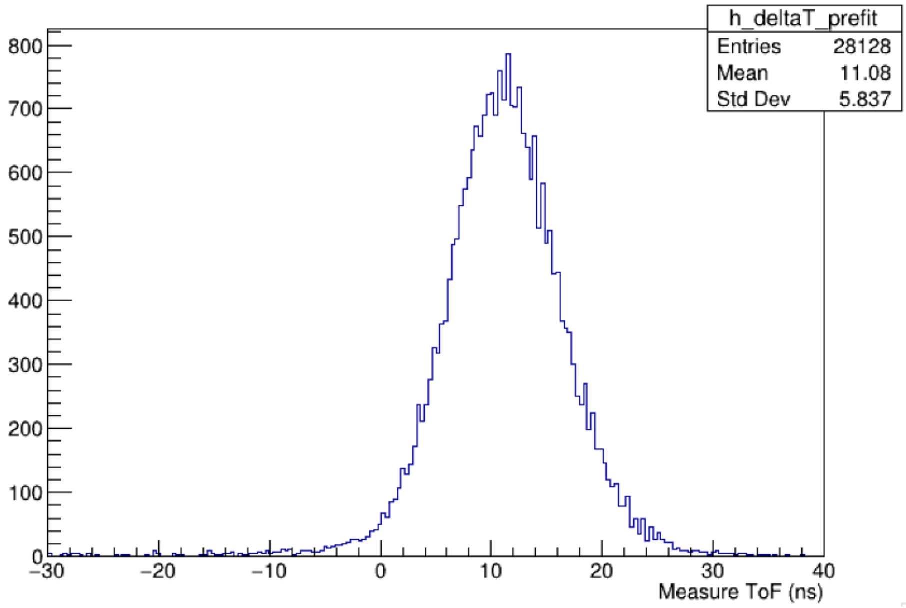

Figure A.2: Measured ToF before subtracting the corrections for the light propagation along the fibers.

the photosensor, that can be evaluated from the y-coordinate. The light propagation time is evaluated as $\frac{\Delta\ell}{v_{fiber}}$, where $v_{fiber} = 0.59c$ is the speed of light through the fiber. After this correction the histogram in Figure A.2 becomes the histogram in Figure A.3. The mean value remains approximately the same, while the standard deviation is reduced by the 8%.
Assuming that no or a negligible contamination by upward-going muons affects the data sample, which consists in only forward events, i.e. events with a track that geometrically appears as downward from the 1st to the 4th plane, the expected muon time Δt_{μ}^{exp} is considered to be positive and is evaluated using the muon path, L, which depends on the track direction as $L = \frac{\Delta\ell_{1,4}}{\cos\theta\cos\phi}$. The difference between the measured muon time, Δt^{meas}, in Figure A.3 and the evaluated time $\Delta t_{\mu}^{exp}(\theta,\phi) = \frac{L}{c}$ is expected to distribute around zero, but at first glance the mean distribution of $\Delta t_{ij}^{meas} - \Delta t_{\mu}^{exp}$ is about 5.2 ns. The reason could be related to some systematics in the TDC calibration; in particular to some possible correlation between boards. To try fixing this issue, learning from data, a free parameter has been added in the definition of $\Delta T_{ij} = \Delta t_{ij}^{meas} - \Delta t_{\mu}^{exp} \Delta t_{ij}^{meas} - \Delta t_{\mu}^{exp}$ where the indices i,j are related to the considered board numbers.

$$\Delta T_{ij} = \frac{t_1^{meas}}{E_1} - \frac{t_4^{meas}}{E_4} + p + \Delta t_4^{\gamma} - \Delta t_1^{\gamma} - \Delta t_{\mu}^{exp} \tag{A.6}$$

Given the expression (A.6), a least square fit has been applied to the quantity $\sum_{events} \Delta T_{1,13}^2$ to get the best value of the parameter p. The distributions of the *train dataset*, the fraction of data used

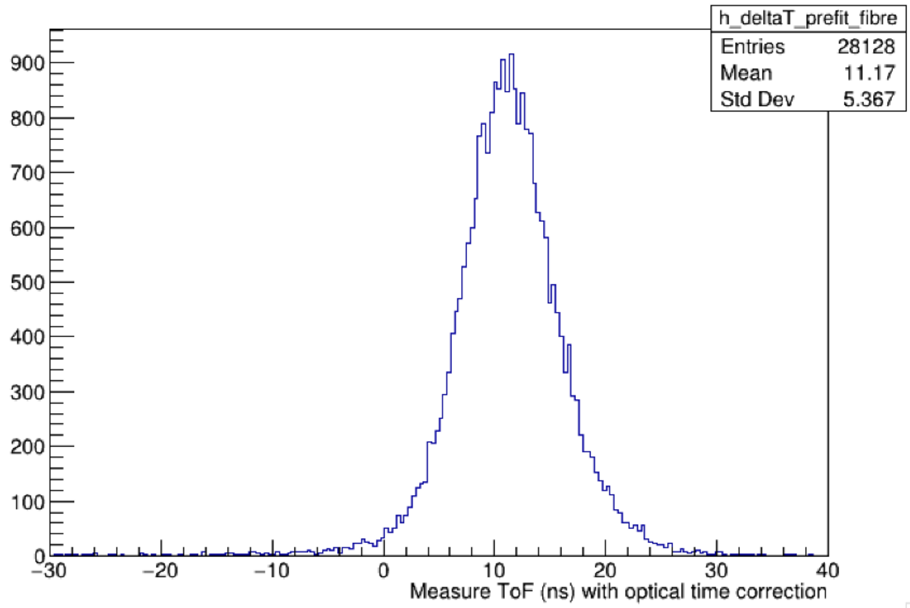

Figure A.3: Measured ToF after subtracting the correction for the light propagation along the fibers, $\Delta t_4^\gamma - \Delta t_1^\gamma$.

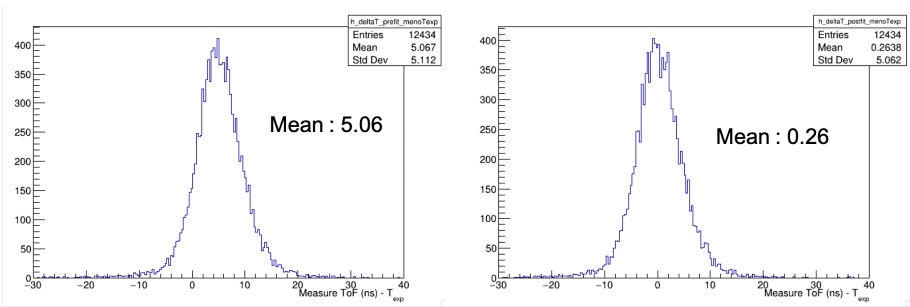

Figure A.4: The distribution of the quantity in eq. (A.6) of the train dataset events, when p=0 (left) and when p = -3.59 ns (right), resulting from the least squares fit.

to perform the fit, before and after the fit are shown in Figure A.4. The estimated parameter $p = -3.59$ has been used to plot the $\Delta T_{1,13}$ for a *test dataset*, *i.e.* a set of events not used to perform the minimization (Figure A.5). The improvement is good for both the train and test datasets. The idea is to use the estimated parameter p to correct data taken on the Mt. Vesuvius and to reject events with ΔT_{ij} lower than - 3σ. The same procedure has been applied to all the possible combinations of the board of 1st and 4th planes.
The above analysis has been intended to better understand and to calibrate the ToF measurement system. It represents a test, applied on one of the hodoscopes, when it was still not moved on the Vesuvius laboratory. Due to the lack of informations about the ToF system calibration parameters, in these same conditions, for the two other hodoscopes, the ToF measurements are not being adopted, at the moment, to make background rejections.

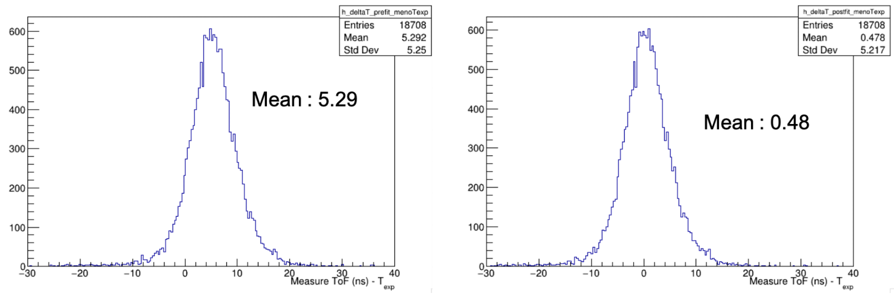

Figure A.5: The distribution of the quantity in eq. (A.6) of a test dataset events, when p=0 (left) and when p = -3.59 ns (right), resulting from the least squares fit.

Bibliography

Here are the references in citation order.

[1] Peter K.F. Grieder. *Cosmic rays at Earth*. Amsterdam: Elsevier, 2016 (cited on pages 3–5).

[2] Thomas K. Gaisser, Ralph Engel, and Elisa Resconi. *Cosmic rays and Particle Physics*. Cambridge: Cambriige University Press, 2001 (cited on pages 3, 4, 6, 7).

[3] Georg Pfotzer. In: *Zeitschr. f. Physik* 102 (1936), p. 23 (cited on page 5).

[4] Georg Pfotzer. In: *Zeitschr. f. Physik* 102 (1936), p. 41 (cited on page 5).

[5] URL: https://arxiv.org/abs/1509.06176v1 (cited on page 7).

[6] Nikolai V. Mokhov Donald E. Groom and Sergei I. Striganov. 'Muon Stopping Power and Range Table 10 MeV -100 TeV'. In: *Atomic Data and Nuclear Data Tables* 78 (2001), pp. 183–356. DOI: 10.1006/adnd.2001.0861 (cited on pages 8, 9, 69).

[7] A. Lechmann *et al*. 'The effect of rock composition on muon tomography measurements'. In: *Solid Earth* 9 (2018), pp. 1517–1533. DOI: 10.5194/se-9-1517-2018 (cited on page 9).

[8] R. Nishiyama *et al*. '3D Density Modeling with Gravity and Muon-Radiographic Observations in Showa-Shinzan Lava Dome, Usu, Japan'. In: *Journal of Geophysical Research Solid Earth* 119 (2014), pp. 699–710 (cited on page 14).

[9] R. Nishiyama *et al*. 'Integrated processing of muon radiography and gravity anomaly data toward the realization of high-resolution 3D density structural analysis of volcanoes: Case study of Showa-Shinzan Lava Dome, Usu, Japan.' In: *Pure Appl. Geophys.* 174 (2017), pp. 1061–1070. DOI: 10.1007/s00024-016-1430-9 (cited on pages 14, 38).

[10] A. Tarantola. *Inverse Problem Theory and Methods for Model Parameter Estimation*. Siam, 2005 (cited on page 14).

[11] G. Bonomi *et al*. 'Applications of cosmic-ray muons'. In: *Progress in Particle and Nuclear Physics* 112 (2020), p. 103768. DOI: 10.1016/j.ppnp.2020.103768 (cited on pages 14, 39, 40).

[12] P. Checchia. 'Review of possible applications of cosmic muon tomography'. In: *JINST* 12 (2016), p. C12072. DOI: 10.1088/1748-0221/11/12/C12072 (cited on page 15).

[13] I. Bodini *et al*. 'Cosmic ray detection based measurement systems: a preliminary study'. In: *Meas. Sci. Technol.* 18 (2007), p. 3537 (cited on pages 15, 40).

[14] G. Bonomi *et al*. 'Cosmic ray tracking to monitor the stability of historical buildings: a feasibility study'. In: *Meas. Sci. Technol.* 30 (2019), p. 045901. DOI: 10.1088/1361-6501/ab00d7 (cited on pages 15, 16, 40).

[15] F. Ambrosino *et al*. 'The MU-RAY project: detector technology and first data from Mt. Vesuvius'. In: *JINST* 9 (2014), p. C02029. DOI: 10.1088/1748-0221/9/02/C02029 (cited on pages 18, 34).

[16] P. Noli et al. 'Muography of the Puy de Dôme'. In: *Annals of Geophysics* 60 (2017), S0105. DOI: 10.4401/ag-7380 (cited on pages 18, 32).

[17] P. Baringer *et al*. 'Cosmic-ray tests of the D0 preshower detector'. In: *Nuclear Instruments and Methods in Physics Research Section A* 469 (2001), p. 295. DOI: 10.1016/S0168-9002(01)00781-1 (cited on page 18).

[18] URL: http://minerva.fnal.gov/ (cited on page 19).

[19] S. Callier *et al*. 'EASIROC, an Easy and Versatile ReadOut Device for SiPM'. In: *Physics Procedia* 37 (2012) (cited on pages 20, 27).

[20] URL: http://www.advansid.com/ (cited on page 22).

[21] L.Cimmino *et al*. 'A new cylindrical borehole detector for radiographic imaging with muons'. In: *Scientific Reports* (2021). DOI: 10.1038/s41598-021-96247-1 (cited on page 24).

[22] L. Cimmino *et al*. 'The MURAVES telescope front-end electronics and data acquisition'. In: *Annals of Geophysics* 60 (2017), p. 1. DOI: 10.4401/ag-7379. (cited on page 27).

[23] G. Saracino *et al*. 'The MURAVES muon telescope: technology and expected performances'. In: 60 (2017), S103. DOI: 10.4401/ag-7378 (cited on page 28).

[24] E. P. George. 'Cosmic Rays Measure Overburden of Tunnel'. In: *Commonwealth Engineer* (1955) (cited on page 30).

[25] L. Alvarez *et al*. 'Search for Hidden Chambers in the Pyramids'. In: *Science* 167 (1970), pp. 832–839 (cited on pages 30, 35).

[26] H. K.M. Tanaka *et al*. 'High resolution imaging in the inhomogeneous crust with cosmic-ray muon radiography: The density structure below the volcanic crater floor of Mt. Asama, Japan'. In: *Earth and Planetary Science Letters* 263 (2007), pp. 103–114. DOI: 10.1016/j.epsl.2007.09.001 (cited on page 31).

[27] H. K.M. Tanaka *et al*. 'Radiographic visualization of magma dynamics in an erupting volcano'. In: *Nature Commun.* 5 (2014), p. 3381. DOI: 10.1038/ncomms4381 (cited on page 31).

[28] M. Rosas-Carbajal *et al*. 'Three-dimensional density structure of La Soufrière de Guadeloupe lava dome from simultaneous muon radiographies and gravity data'. In: *Geophys.Res. Lett.* 44 (2017), pp. 6743–6751. DOI: doi:10.1002/2017GL074285 (cited on page 32).

[29] K. Jourde *et al*. 'Muon dynamic radiography of density changes induced by hydrothermal activity at the La Soufrière of Guadeloupe volcano'. In: *Sci. Rep.* 6 (2016), p. 33406. DOI: https://doi.org/10.1038/srep33406 (cited on page 32).

[30] Y Le Gonidec *et al*. 'Abrupt changes of hydrothermal activity in a lava dome detected by combined seismic and muon monitoring'. In: *Sci. Rep.* 9 (2019), p. 3079. DOI: https://doi.org/10.1038/s41598-019-39606-3 (cited on page 32).

[31] D. Carbone *et al*. 'An experiment of muon radiography at Mt Etna (Italy)'. In: *Geophys. J. Int.* 196 (2014), pp. 633–643. DOI: 10.1093/gji/ggt403 (cited on page 33).

[32] Lo Presti *et al*. 'An experiment of muon radiography at Mt Etna (Italy)'. In: *Nuclear Inst. and Methods in Physics Research, A* 904 (2018), pp. 195–201. DOI: 10.1016/j.nima.2018.07.048 (cited on page 34).

[33] G. Ambrosi *et al*. 'The MU-RAY project: Volcano radiography with cosmic-ray muons'. In: *Nuclear Inst. and Methods in Physics Research, A* 628 (2011), pp. 120–123. DOI: 10.1016/j.nima.2010.06.299 (cited on page 34).

[34] A. Anastasio *et al*. 'The MU-RAY detector for muon radiography of volcanoes'. In: *Nuclear Inst. and Methods in Physics Research, A* 732 (2013), pp. 423–426. DOI: 10.1016/j.nima.2013.05.159 (cited on page 34).

[35] V. Tioukov *et al*. 'First muography of stromboli volcano)'. In: *Sci. Rep.* 9 (2019), p. 6695. DOI: https://doi.org/10.1038/s41598-019-43131 (cited on page 34).

[36] S. Aguilar et al. In: *X Latin American Symposium on Nuclear Physics and Applications (X LASNPA)* (2013).

[37] K. Morishima *et al*. 'Discovery of a big void in Khufu's Pyramid by observation of cosmic-ray muons'. In: *Nature* 552 (2017), pp. 386–390. DOI: https://doi.org/10.1038/nature24647 (cited on page 36).

[38] D. Schouten *et al*. 'Muon Tomography Applied to a Dense Uranium Deposit at the McArthur River Mine'. In: *JGR Solid Earth* 123 (2018), pp. 8637–8652. DOI: https://doi.org/10.1029/2018JB015626 (cited on page 37).

[39] D. Byman *et al*. 'Blind Test of Muon Geotomography for Mineral Exploration'. In: *ASEG-PESA 2015* (2015) (cited on page 37).

[40] *Mublast project, Research found for coal and steel RFSR-CT-2014-00027*. URL: https://ec.europa.eu/research/industrial_technologies/%20pdf/rfcs/summaries-%20rfcs_en.pdf (cited on page 38).

[41] URL: https://decisionsciences.com/our-product/ (cited on page 39).

[42] *Mu Steel project, Research Fund for Coal and Steel RFSR-CT-2010-00033*. URL: https://ec.europa.eu/research/industrial_%20technologies/pdf/rfcs/summaries-%20rfcs_en.pdf (cited on page 39).

[43] G. Imbò. 'L'attività eruttiva vesuviana e relative osservazioni nel corso nell'intervallo 1906-1944 ed in particolare del parossismo del Marzo 1944'. In: *Annali dell'Osservatorio Vesuviano - volume unico celebrativo del I centenario dell'Osservatorio Vesuviano, Stabilimento Tipografico G. Genovese, Napoli* (1949) (cited on page 42).

[44] URL: https://www.victronenergy.it/ (cited on page 44).

[45] N. Lesparre *et al*. 'Geophysical muon imaging: feasibility and limits'. In: *Geophys. J. Int.* 183 (2010), pp. 1248–1361. DOI: 10.1111/j.1365-246X.2010.04790.x (cited on pages 49, 50).

[46] Vilardo et al. 'Digital Terrain Model (DTM) of Vesuvius crater'. In: (2013) (cited on page 65).

[47] URL: https://root.cern/ (cited on page 65).

[48] URL: https://arxiv.org/abs/1904.03435v1 (cited on page 66).

[49] V. Niess *et al*. 'Backward Monte-Carlo applied to muon transport'. In: *Computer Physics Communications* 229 (2018), pp. 54, 57. DOI: 10.1016/j.cpc.2018.04.001 (cited on pages 66, 67).

[50] G. Baccani *et al*. 'The MIMA project. Design, construction and performances of a compact hodoscope for muon radiography applications in the context of archaeology and geophysical prospections'. In: *Journal of Instrumentation* 13 (2018), P11001. DOI: 10.1088/1748-0221/13/11/P11001 (cited on page 81).

[51] L. Bonechi *et al*. 'Development of the ADAMO detector: test with cosmic rays at different zenith angles.' In: *29th Int. Cosmic Ray Conference, Pune* 9 (2005), pp. 283–286 (cited on pages 83, 91).

[52] G. Saracino *et al*. 'Imaging of underground cavities with cosmic-ray muons from observations at Mt. Echia (Naples)'. In: 7 (2017), p. 1038. DOI: 10.1038/s41598-017-01277-3 (cited on page 83).

[53] L. Cimmino et al. '3D Muography for the Search of Hidden Cavities'. In: *Scientific Reports* 9 (2019), p. 2974 (cited on pages 85, 87).

[54] K. Nagamine. *Introductory Muon Science*. Cambridge University Press, 2009 (cited on page 91).